UMCS

MARIA CURIE-SKŁODOWSKA UNIVERSITY
LUBLIN

Faculty of Mathematics, Physics
and Computer Science

Department of Theoretical Physics

Szczepan Głodzik
supervisor: prof. dr hab. Tadeusz Domański

Influence of spin-orbit interactions on bound states in superconductors

Lublin 2020

UNIWERSYTET MARII CURIE-SKŁODOWSKIEJ
W LUBLINIE

Wydział Matematyki, Fizyki i Informatyki

Katedra Fizyki Teoretycznej

Szczepan Głodzik
promotor: prof. dr hab. Tadeusz Domański

Wpływ oddziaływań spinowo-orbitalnych na stany związane w nadprzewodnikach

Lublin 2020

Preface

In this short preface, I would like to express my appreciation to the people who made my doctoral journey possible. First of all – my supervisor, professor Tadeusz Domański, to whom I am forever indebted for believing in my abilities of transitioning to thoretical physics. I am deeply grateful for the countless hours of discussions and answers to my questions, which always came in great abundance. I am also thankful to all of my co-authors and colleagues, among whom Teemu Ojanen deserves a distinction, for both teaching me and learning with me.

To my wife, whose passion and drive are a constant source of inspiration for me – thank you. I am proud of being a part of this dynamic duo. I am also grateful to my parents for the ongoing love and support. And in the unlikely event of any of my siblings ever reading this, I hope I ignited at least a tiny spark of interest in science in you.

Lublin, May 2020

Acknowledgements

During the work on the majority of the papers presented in this thesis, I was supported by the National Science Centre (NCN), under the grant PRELUDIUM 2017/27/N/ST3/01762.

Contents

Chapter 1

Introduction

Arguably every thesis concerning superconductivity starts with a few words about the great discovery by Heike Kamerlingh-Onnes, and this one shall not be different. The measurements of 8th April 1911 left an imprint in the world of physics, remarkable not only for the huge impact that the zero-resistance flow of charge has on the modern world, but also, or maybe even more for the gargantuan struggle of theoretical physicists aiming to erect a microscopic theory describing this baffling phenomenon. The epochal *Kwik nagenoeg nul* [1] reported by Kamerlingh-Onnes raised a puzzle with which giants like Bloch, Bohr, Heisenberg or Born wrestled and failed. Even Feynman, albeit concluding that the correct theoretical description of superconductivity is unachievable using perturbation theory, ascribed his low amount of published work in the 1950's to his endeavor in finding the correct approach [2]. It took 46 years and efforts of John Bardeen, Leon Cooper and Robert Schrieffer to finally arrive at the correct microscopic description of superconducting state, termed since as BCS theory [3]. Another big leap in understanding exotic phases of matter, which happens to be connected to the present thesis, was ignited by the discovery of the quantum Hall effect by Klaus von Klitzing [4]. As a result, the celebrated Landau paradigm of classifying phases of matter by symmetry breaking and order parameters became inadequate. Across the superconducting transition, it is the gauge symmetry that is said to be broken (although it is somewhat of a loose statement [5]), and an order parameter acquires a non-zero value. There is no local order parameter that can describe the quantum Hall state, nor is there a spontaneously broken symmetry when transitioning to such a state. We can rather say that this state is *topologically*

distinct from other phases of matter, in the sense that some of its properties (e.g. number of gapless states dispersing on the edge of the sample) are invulnerable to smooth perturbations of the system like irregularities or disorder, as long as the single particle gap is not closed. It is the twisting and knotting of electron wavefunctions in momentum space [6] that is responsible for the existence of celebrated gapless edge states, when topologically disparate materials are connected – a manifestation of bulk-boundary corespondence. Whether they are end states in the Su-Schrieffer-Heeger model [7], helical edge states of the quantum spin Hall effect [8, 9], or chiral Majorana modes on the edge of a semiconducting film in a two dimensional heterostructure [10], they have received an enormous amount of attention recently, especially since 2016, when John Michael Kosterlitz, David Thouless and Duncan Haldane were awarded the Nobel Prize in Physics *for theoretical discoveries of topological phase transitions and topological phases of matter*. Both superconductivity and topology are important in the present thesis, although it is the presence of impurities and bound states associated with them, that permiate throughout this work. On the one hand, there are scalar impurities, i.e. those which do not break time reversal symmetry and hence do not lift the Kramers degeneracy, which were shown by Anderson [11] to not alter the critical temperature of a superconductor. However that may be changed, when a disordered system is strongly correlated [12]. Additionally, non-magnetic impurities will not host any bound states, although this statement is not true for superconductors with pairing symmetry different than s-wave [13] and in the case of quantum dots. On the other hand, magnetic adsorbates locally break Cooper pairs and induce a pair of bound states in the superconducting energy gap. The focus on the smallest possible additives and their local influence on the host would not make sense without an appropriate experimental technique. The great invention by Gerd Binnig and Heinrich Rorher [14] (who shared the 1986 Nobel Prize in Physics with Ernst Ruska) revolutionized the domain of surface imaging, and provided an exceptional device – Scanning Tunneling Microscope (STM), which to this day provides astonishing images of surfaces and enables the study of various phenomena manifesting in the local density of states. The preceding phenomena appear throughout this work, and are tied together by one more – the spin-orbit interaction. The first contact with it is usually the introductory course on quantum mechanics, where one learns that it is a relativistic effect,

which results in splitting of the atomic energy levels. In condensed matter physics, we are more used to the idea of electronic bands. Nevertheless it is convenient to consider an electron moving in the electric field stemming from the crystalline potential. In its rest frame, the electron feels an effective magnetic field, proportional to its momentum, and it is this effect that leads to energy splitting of the spin sub-bands. The spin-orbit interaction is odd in momentum, and the first to show that it arises in systems without an inversion symmetry was Dresselhaus [15] and Bychkov and Rashba [16]. To visualize the physical implications of the e.g. Rashba effect, one can formulate an analogy to the Magnus effect. A spinning object's trajectory will be deflected due to a force coming from a pressure difference. Analogously, the electrons moving through a solid may also be deflected, depending on their intrinsic angular momentum, resulting in spin Hall effect. Recently, spin-orbit coupling in solids receives much attention, not only because it is responsible for a surge in development of a new field dubbed spin-orbitronics, but also due to the emergence of many novel phases of matter which require the presence of this interaction [17]. This thesis focuses on bound states induced by the presence of magnetic impurities in superconductors and with the influence that various types of spin-orbit interactions might have on them. In the main part the theoretical background concerning most important phenomena will be laid out. Next we present a discussion of methods used to examine the selected physical systems. A summary of the findings from the papers co-authored by the author and closely related to the present thesis will serve as a conclusion.

Chapter 2

Theoretical background

2.1 Fundamentals of superconductivity

As mentioned above and realized by many physicists in the 20th century, the correct description of the superconducting state cannot be approached by perturbative methods. It was Leon Cooper, who explicitly showed that it is the case [18]. Assuming that two electrons forming a singlet state interact above a filled Fermi sphere, Cooper showed that the energy (relative to the sum of energies at the Fermi sphere) of such a pair will become

$$\varepsilon = -2\ \omega_D\ e^{-\frac{2}{V\rho(0)}}. \tag{2.1}$$

We note that this energy is negative, hence this state is a bound state. The Debye frequency ω_D refers to the idea of Fröhlich, that the attractive interaction between electrons might originate from electron-phonon interactions [19]. Building on these facts BCS proposed a variational wavefunction, which is a coherent superposition of Cooper pairs:

$$|\Psi_{BCS}\rangle = \prod_{\boldsymbol{k}} \left(u_{\boldsymbol{k}} + v_{\boldsymbol{k}} c^{\dagger}_{\boldsymbol{k}\uparrow} c^{\dagger}_{-\boldsymbol{k}\downarrow}\right)|0\rangle, \tag{2.2}$$

with zero being the vacuum and $u_{\boldsymbol{k}}$, $v_{\boldsymbol{k}}$ some complex coefficients, on which we will elaborate below. One can see that there are many peculiar properties of this wavefunction, like the fact that it is a superposition of states with different total number of electrons. Knowing that

only electrons with energies below $\hbar\omega_D$ are important in the problem, and that the Cooper instability arises from the scattering of electrons with opposite spin, we can write

$$H = \sum_{\boldsymbol{k}\sigma} \xi_{\boldsymbol{k}} c^\dagger_{\boldsymbol{k}\sigma} c_{\boldsymbol{k}\sigma} + \sum_{k,k'} V_{\boldsymbol{k}\boldsymbol{k}'} c^\dagger_{\boldsymbol{k}\uparrow} c^\dagger_{-\boldsymbol{k}\downarrow} c_{-\boldsymbol{k}'\downarrow} c_{\boldsymbol{k}'\uparrow} \tag{2.3}$$

and treat $V_{\boldsymbol{k}\boldsymbol{k}'}$ as an effective, attractive interaction ($V_{\boldsymbol{k}\boldsymbol{k}'} \equiv V < 0$) between electrons of interest (with $|\xi_{\boldsymbol{k}}| < \hbar\omega_D$). We will also focus on the isotropic (or s-wave) gap and write $\Delta_{\boldsymbol{k}} = \Delta$. Introducing the mean-field approximation, justified by the coherence length ξ in BCS superconductors being of the order of 1000Å, we argue that the difference between an operator and its expectation value is small

$$(A - \langle A\rangle)(B - \langle B\rangle) \sim 0, \tag{2.4}$$

so we can say that

$$AB \simeq \langle A\rangle B + A\langle B\rangle - \langle A\rangle\langle B\rangle. \tag{2.5}$$

We then identify $A = c^\dagger_{\boldsymbol{k}\uparrow} c^\dagger_{-\boldsymbol{k}\downarrow}$ and $B = c_{-\boldsymbol{k}'\downarrow} c_{\boldsymbol{k}'\uparrow}$, to finally express the reduced BCS Hamiltonian (with the constant term $\langle A\rangle\langle B\rangle$ omitted):

$$H = \sum_{\boldsymbol{k}\sigma} \xi_{\boldsymbol{k}} c^\dagger_{\boldsymbol{k}\sigma} c_{\boldsymbol{k}\sigma} + \Delta \sum_k c^\dagger_{\boldsymbol{k}\uparrow} c^\dagger_{-\boldsymbol{k}\downarrow} + \Delta^* \sum_{\boldsymbol{k}} c_{-\boldsymbol{k}\downarrow} c_{\boldsymbol{k}\uparrow}, \tag{2.6}$$

where

$$\begin{aligned} \Delta &= V\langle c_{-\boldsymbol{k}\downarrow} c_{\boldsymbol{k}\uparrow}\rangle \\ \Delta^* &= V\langle c^\dagger_{\boldsymbol{k}\uparrow} c^\dagger_{-\boldsymbol{k}\downarrow}\rangle. \end{aligned} \tag{2.7}$$

The non-zero value of Δ informs us about the superconducting transition, and as we will shortly see, its magnitude reflects the energy gap in the electronic spectrum. To analyze the Hamiltonian (2.6) we will employ the Bogoliubov-Valatin transformation, which can be summarized in the following identity:

$$\begin{pmatrix} c_{\boldsymbol{k}\uparrow} \\ c^\dagger_{-\boldsymbol{k}\downarrow} \end{pmatrix} = \begin{pmatrix} u_{\boldsymbol{k}} & v_{\boldsymbol{k}} \\ -v_{\boldsymbol{k}} & u_{\boldsymbol{k}} \end{pmatrix} \begin{pmatrix} \gamma_{\boldsymbol{k}\uparrow} \\ \gamma^\dagger_{-\boldsymbol{k}\downarrow} \end{pmatrix}, \tag{2.8}$$

in which we introduce new fermionic operators $\gamma_{\boldsymbol{k}}^{(\dagger)}$, which annihilate (create) Bogoliubov quasiparticles – Bogoliubons. To state the matter in a more picturesque fashion – an electron is represented as a superposition of a quasiparticle and a quasihole. We demand that the BCS Hamiltonian Eq. (2.6) is diagonal in the space of those operators. The explicit form of the operator space rotation matrix (2.8) can vary in literature. Common is the fact that when plugged into the BCS Hamiltonian it will yield a familiar formula:

$$u_{\boldsymbol{k}} v_{\boldsymbol{k}} = \frac{\Delta}{\sqrt{\xi_{\boldsymbol{k}}^2 + \Delta^2}}, \tag{2.9}$$

which when combined with the result of enforcing fermionic anitcommutation relations of operators $\gamma_{\boldsymbol{k}}$

$$\{\gamma_{\boldsymbol{k}}^\dagger, \gamma_{\boldsymbol{k}}\} = 1, \tag{2.10}$$

gives the following relations:

$$\begin{aligned} u_{\boldsymbol{k}}^2 &= \frac{1}{2}\left(1 + \frac{\xi_{\boldsymbol{k}}}{\sqrt{\xi_{\boldsymbol{k}}^2 + \Delta^2}}\right), \\ v_{\boldsymbol{k}}^2 &= \frac{1}{2}\left(1 - \frac{\xi_{\boldsymbol{k}}}{\sqrt{\xi_{\boldsymbol{k}}^2 + \Delta^2}}\right). \end{aligned} \tag{2.11}$$

Having those identities, we can insert them into the Hamiltonian expressed with the Bogoliubov quasiparticle operators, to see that it acquires a simple form:

$$H = \sum_{\boldsymbol{k}\sigma} E_{\boldsymbol{k}} \gamma_{\boldsymbol{k}\sigma}^\dagger \gamma_{\boldsymbol{k}\sigma}, \tag{2.12}$$

where the energy in the diagonal basis $E_{\boldsymbol{k}} = \sqrt{\xi_{\boldsymbol{k}}^2 + \Delta^2}$. We can see from (2.11) that in the normal state ($\Delta \to 0$), the Bogoliubons represent holes for energies less than the Fermi level, and particles for $\xi_{\boldsymbol{k}} > E_F$. The onset of superconductivity, embodied by the non-zero value of Δ, leads to a gap in the spectrum – the energy of an excited quasiparticle has to be at least Δ. We will now examine the gap equation

$$\Delta = V \sum_k \frac{\Delta}{2E_{\boldsymbol{k}}} \tanh\left(\frac{E_{\boldsymbol{k}}}{2k_B T}\right), \tag{2.13}$$

which can be obtained via insertion of the Bogoliubov-Valatin tranformation into Eq. (2.7), and study its limiting behavior. First, if we let $T \to 0$ we are left with the following equation

$$1 = V\rho(0) \int_0^{\omega_D} \frac{d\varepsilon}{\sqrt{\varepsilon^2 + \Delta^2}}. \tag{2.14}$$

After careful evaluation, the above leads to a familiar result

$$\Delta = 2\omega_D \; e^{\frac{-1}{V\rho(0)}} \tag{2.15}$$

in agreement with the Schrödinger equation approach used by Cooper (cf. Eq (2.1)). On the opposite side, when we send the gap to zero $\Delta \to 0$, we can find the critical temperature T_C. Again carefully evaluating the gap equation we arrive at

$$T_C = \frac{e^\gamma}{\pi} \; \frac{2\omega_D}{k_B} \; e^{\frac{-1}{V\rho(0)}}, \tag{2.16}$$

where γ is the Euler constant. Evaluation of $\dfrac{\Delta(T \to 0)}{k_B T_C}$ leads to the most celebrated result of the BCS theory, stating that

$$\frac{\Delta(T \to 0)}{k_B T_C} \approx 1.76 \tag{2.17}$$

is universal for conventional superconductors.

Yu-Shiba-Rusinov states

As every material is fundamentally impure, the study of impurities in both metals and superconductors is natural. When considering magnetic impurities in metals, one can dwell on whether the Kondo effect [20], or the Anderson impurity model [21] is the apex of theoretical efforts. The first studies examining a spherical impurity in superconducting hosts were reported by Fetter [22]. It was quickly realized that a non-magnetic impurity does not give rise to bound states with subgap energy, or rather, they do exist only in a window of about $10^{-3}\Delta$ from the gap edge, thus they are irrelevant [23]. The above statement is modified in the context of 'artificial atoms' – quantum dots (QD), which can support in-gap bound states when proximitized to a superconducting lead. When the charging energy of

the dot is smaller than Δ, there is a bound state composed out of a superposition of empty and doubly occupied state [24]. In the opposite regime (more common), i.e. $U >> |\Delta|$, if the dot hosts an odd number of electrons, a single quasiparticle bound to the spin on the QD emerges. This state is usually called Yu-Shiba-Rusinov state, in analogy to the case of a classical magnetic impurity in a superconductor [25]. One can see that in the context of QDs, there is not much difference between the two regimes in terms of spectroscopy. This difference is however rather large when considering impurities, as we will now find out. The late 1960s were the time when the topic of bound states in s-wave superconductors induced by magnetic impurities was first considered by Luh Yu [26], Hiroyuki Shiba [27] and Anatol Rusinov [28]. The main caveat is that the impurities were assumed to be classical spins. It is probably put in the most elegant way in Shiba's paper, where he claims that having a Hamiltonian for the interaction of conduction electrons with a localized spin:

$$H = \frac{J}{2N} \sum_{\boldsymbol{k},\boldsymbol{k'}} c^{\dagger}_{\boldsymbol{k}} \boldsymbol{\sigma} c_{\boldsymbol{k'}} \cdot \boldsymbol{S}, \tag{2.18}$$

one can assume that the strength of the interaction $J \to 0$ and the impurity spin $S \to \infty$, keeping the product JS finite. In this way we omit any quantum mechanical dynamics of spin. Despite the three aforementioned authors employing different approaches, the conclusion is the same: if there is a time reversal breaking, localized potential in contact with a superconductor, there will be a pair of single particle bound states inside the superconducting gap. First experimental results confirming this statement were reported in 1997 when the IBM Almaden group examined various magnetic and non-magnetic adsorbates on the surface of Niobium [29]. The STM spectra collected around the magnetic impurities revealed two bound states at energies below the BCS gap, which were asymmetric in spectral weight – a consequence of particle-hole symmetry breaking Coulomb potential and imbalances in the normal state conductance [30]. We will now embark on finding the energy of such bound states, starting with the familiar BCS Hamiltonian, or rather, the Hamiltonian density

$$H = \xi_{\boldsymbol{k}} \tau_z \sigma_0 + \Delta \tau_x \sigma_0 - JS\delta(\boldsymbol{r}) \tau_0 \sigma_z, \tag{2.19}$$

in the Nambu basis $\Psi = (\psi_{\boldsymbol{k}\uparrow}, \psi_{\boldsymbol{k}\downarrow}, \psi^\dagger_{-\boldsymbol{k}\downarrow}, -\psi^\dagger_{-\boldsymbol{k}\uparrow})^T$. In (2.19) the tensor product between matrices τ and σ is implied. These are the Pauli matrices which operate in particle-hole and spin space respectively. To make things simpler we can now split the Hamiltonian into two separate ones for spin-up and spin-down (while dropping the identity matrix τ_0)

$$H_\pm = \xi_{\boldsymbol{k}}\tau_z + \Delta\tau_x \mp JS\delta(\boldsymbol{r}). \tag{2.20}$$

We now write the Schrödinger equation with the impurity term isolated on the right hand side:

$$[E - \xi_{\boldsymbol{k}}\tau_z - \Delta\tau_x]\psi(\boldsymbol{r}) = \mp JS\delta(\boldsymbol{r})\psi(0), \tag{2.21}$$

and proceed by employing a nifty trick. We first make use of the Fourier transform $\psi_{\boldsymbol{k}} = \int \frac{d\boldsymbol{r}}{(2\pi)^3} e^{-i\boldsymbol{k}\boldsymbol{r}}\psi(\boldsymbol{r})$ to get rid of the Dirac delta, which gives:

$$[E - \xi_{\boldsymbol{k}}\tau_z - \Delta\tau_x]\psi_{\boldsymbol{k}} = \mp JS\psi(0). \tag{2.22}$$

Now we multiply from the left by $[E - \xi_{\boldsymbol{k}}\tau_z - \Delta\tau_x]^{-1}$ and use the inverse Fourier transform to obtain an equation for the spinor at the position of the impurity, which is the origin:

$$\psi(0) = \int_{-\infty}^{\infty} \frac{d\boldsymbol{k}}{(2\pi)^3} \frac{\mp JS}{E^2 - \xi^2_{\boldsymbol{k}} - \Delta^2}[E + \xi_{\boldsymbol{k}}\tau_z + \Delta\tau_x]\psi(0), \tag{2.23}$$

where we have explicitly written the inverse matrix, an easy task considering we are working with 2x2 matrices. Looking at (2.23) we observe that we have two integrals to solve:

$$\mathcal{I}_1 = \int_{-\infty}^{\infty} \frac{d\boldsymbol{k}}{(2\pi)^3} \frac{1}{E^2 - \xi^2_{\boldsymbol{k}} - \Delta^2}, \tag{2.24}$$

$$\mathcal{I}_2 = \int_{-\infty}^{\infty} \frac{d\boldsymbol{k}}{(2\pi)^3} \frac{\xi_{\boldsymbol{k}}}{E^2 - \xi^2_{\boldsymbol{k}} - \Delta^2}. \tag{2.25}$$

We first make use of a usual substitution $\int \frac{d\boldsymbol{k}}{(2\pi)^3} = \nu_0 \int d\xi_{\boldsymbol{k}}$, where ν_0 is the density of states at the Fermi energy. Now the integrand in Eq. (2.25) is odd in $\xi_{\boldsymbol{k}}$ so the integral vanishes.

The integral (2.24) can be solved using contour integration, seeing that we are interested in subgap energies $E < \Delta$, and we obtain $\mathcal{I}_1 = -\dfrac{\pi\nu_0}{\sqrt{\Delta^2 - E^2}}$. Using this result we can now express equation (2.23) as:

$$\left[\mathbb{1} \mp \frac{\alpha[E + \Delta\tau_x]}{\sqrt{\Delta^2 - E^2}}\right] \psi(0) = 0. \tag{2.26}$$

Solving for energy we obtain the formula for the energy of Yu-Shiba-Rusinov states

$$E_{YSR} = \pm\Delta \frac{1 - \alpha^2}{1 + \alpha^2}, \tag{2.27}$$

where in both of the above equations we have introduced the coupling constant as $\alpha = JS\pi\nu_0$. By examining Eq. (2.27) we can see that the energy of a Shiba state will always be smaller than the the superconducting gap. Additionally, a special value of the strength of impurity-substrate coupling can lead to the energy of YSR states being zero. This is the critical coupling, at which the ground state of the system changes – a manifestation of the quantum phase transition, which we will now study in more detail.

Quantum phase transition

Since in general we focus on classical impurities with $S \gg 1$, complete screening of this moment is not possible, hence the implications of the Kondo model, albeit admittedly fascinating [31, 32], can be discarded. We will therefore follow the reasoning of Balatsky et al. [13] and references therein. In the weak coupling regime, i.e. when the coupling constant J is smaller than the critical value $J_C = 1/\pi\nu_0 S$, the ground state is the true BCS state in the presence of the impurity potential (cf. Eq. (2.2)). If we examine the net spin of conduction electrons in the ground state we will naturally see that it is null $\langle\Psi_0|\boldsymbol{S}_{el}|\Psi_0\rangle$=0. The first excited state in this regime is the quasiparticle with energy E_{YSR} and we label it as $|\Psi_{ex}\rangle = \gamma^\dagger|\Psi_0\rangle$, where $\gamma^\dagger$ is the quasiparticle creation operator that we have encountered in section 2.1. It is a fermionic quasiparticle, thus it is now not surprising that the net spin is $\langle\Psi_{ex}|\boldsymbol{S}^z_{el}|\Psi_{ex}\rangle = -1/2$. When the impurity coupling reaches the critical value, E_{YSR} becomes a zero energy state and the ground state becomes unstable. Above J_C it is more energetically favorable to induce the unpaired spin rather than to form a pair. Thence in the strong coupling situation $J > J_C$, $|\Psi_0\rangle$ and $|\Psi_{ex}\rangle$ exchange roles, and now the ground state of

the system (with net spin $-1/2$) is a non-BCS state, because of the presence of an unpaired single-particle state. The additional spin-down quasiparticle (assuming antiferromagnetic alignment and spin-up impurity) locally supresses the pair potential Δ, even resulting in its sign change in the strong coupling regime. This is reminiscent of the $0-\pi$ shift in Josephson junctions, manifested by the reversal of the supercurrent [33], and indeed the sign reversal of the order parameter in the vicinity of the impurity is sometimes dubbed 'π phase shift'. While the case of Josephson current reversal is well established and understood, origins of the sign change of $\Delta(r = r_0)$ remain mysterious, although numerical simulations suggest it is rather general. An analytic estimate was put forward in a recent work [34], which predicts the change in the gap function at the impurity site for $J = J_C$ to be

$$\delta\Delta(r = r_{imp}) \sim \frac{\Delta}{ln(\omega_D/\Delta)}. \tag{2.28}$$

It is also worth noting that when treated self-consistently, the supression of Δ around the impurity contributes to the free energy, and the critical value of the impurity coupling is shifted downwards. Naturally a question arises whether the presented reasoning reflects itself in any form in empirical results. Looking at the expression for E_{YSR} Eq. (2.27), only the coupling J is a parameter that can be experimentally manipulated. The most common way is to depend on the discrete changes in J determined by the adsorption sites [31, 35]. A new approach is to use the forces between the STM tip and the impurity (approximated by the Lennard-Jones potential) and continuously control the coupling, as presented for the first time in reference [34].

2.2 Topological matter

Topology as a branch of mathematics, which studies how shapes can be smoothly deformed into each other, was adapted in condensed matter to describe topologically equivalent Hamiltonians. It turns out that just as geometric objects, which are topologically equivalent have the same topological invariant, translationally invariant Hamiltonians, connected by adiabatic changes preserving the energy gap, can be called topologically equivalent. This naturally leads to

the fact that if the excitation gap closes upon such deformation, the topologically distinct systems are separated by a phase transition. If we are concerned with Hamiltonians labeled by the crystal momentum, the information about invariants must be contained in their wavefunctions. It was sir Michael Berry, who found that aside from the familiar dynamical phase, eigenstates of a Hamiltonian depending on slowly varying parameters pick up an additional, geometrical phase, now widely recognized as the Berry phase [36]. Exploiting the ambiguity in the solutions of $H_{\boldsymbol{k}}|u_n(\boldsymbol{k})\rangle = E_n(\boldsymbol{k})|u_n(\boldsymbol{k})\rangle$, we can write

$$|u_n(\boldsymbol{k})\rangle \longrightarrow e^{i\phi_n(\boldsymbol{k})}|u_n(\boldsymbol{k})\rangle. \tag{2.29}$$

The rate of change of the wave function in k space is defined as

$$\boldsymbol{\mathcal{A}}_n(\boldsymbol{k}) = i\langle u_n(\boldsymbol{k})|\nabla_{\boldsymbol{k}}|u_n(\boldsymbol{k})\rangle, \tag{2.30}$$

and bears the name Berry connection. It is an analogue of the electromagnetic vector potential and by virtue of the transformation Eq. (2.29), it also changes in a familiar way

$$\boldsymbol{\mathcal{A}}_n(\boldsymbol{k}) \longrightarrow \boldsymbol{\mathcal{A}}_n(\boldsymbol{k}) - \nabla_{\boldsymbol{k}}\phi_n(\boldsymbol{k}). \tag{2.31}$$

A gauge invariant quantity that we can construct is the Berry curvature, again in analogy to electromagnetism $\boldsymbol{\mathcal{F}}_n(\boldsymbol{k}) = \nabla_{\boldsymbol{k}} \times \boldsymbol{\mathcal{A}}_n(\boldsymbol{k})$. It turns out that the integral of the Berry curvature over the two dimensional Brillouin zone is the Chern number

$$C_n^1 = \frac{1}{2\pi}\int_{BZ} dk_x\ dk_y\ \boldsymbol{\mathcal{F}}_n(\boldsymbol{k}), \tag{2.32}$$

which is one the most fundamental integer invariants. In the above equation the superscript 1 reflects the fact that it is the first Chern number, closely related to the quantum Hall effect, where the conductance is given by $\sigma_{xy} = n\dfrac{e^2}{h}$, with integer n being the total Chern number of the occupied bands

$$n \equiv C = \sum_{E_n<E_F} C_n^1. \tag{2.33}$$

It was shown by Simon [37], that the language of Berry phase and the Chern number is equivalent to the famous TKNN invariant, formulated by Thouless, Kohmoto, Nightingale and den Nijs in the seminal 1982 paper [38]. There are different invariants for different classes of symmetries. Depending on the presence or absence of time reversal, particle-hole (charge conjugation) and chiral symmetries, topological states fall into one of the 10 symmetry classes, summarized in a 'periodic table' [39]. One additional remark is due as we segue to the description of the quantum spin Hall effect in the next paragraph. The total Berry curvature is odd under time reversal

$$\sum_{E_n<E_F} \boldsymbol{\mathcal{F}}_n(\boldsymbol{k}) \longrightarrow - \sum_{E_n<E_F} \boldsymbol{\mathcal{F}}_n(-\boldsymbol{k}), \tag{2.34}$$

therefore the total Chern number of a system, which preserves time reversal symmetry is $C = 0$. It is no surprise, as the quantum Hall effect requires an externally applied magnetic field. However, the quantum spin Hall phase is an example of a topologically non trivial phase utilizing spin-orbit interactions, which do not break the time reversal symmetry. We will now shortly describe it.

Quantum spin Hall effect

Before introducing the ideas from the seminal paper by Kane and Mele [9], it is useful to mention the general approach taken by Haldane to describe a two dimensional topological insulator in a graphene lattice [40]. The continuum description of graphene, with the Hamiltonian linearized around the K or K' point is

$$\mathcal{H} = -i\hbar v_F(\sigma_x\tau_z\partial_x + \sigma_y\partial_y), \tag{2.35}$$

with $v_F = \dfrac{3at}{2}$, where a is the lattice constant and t nearest-neighbor hopping. Pauli matrices σ and τ operate in the sublattice and valley (K and K' point) spaces respectively. We have also already expressed the momentum measured relative to the Dirac points as $q \to -i\hbar\nabla$. The celebrated linear spectrum follows from Eq (2.35) $E(\boldsymbol{q}) = \pm\hbar v_F|\boldsymbol{q}|$. At the Dirac points ($\boldsymbol{q} = 0$) the inversion $\mathcal{P}$ and time reversal $\mathcal{T}$ symmetries protect the degeneracy. The gap

can be opened by breaking those symmetries, e.g. by introducing a mass term proportional to σ_z, which would describe a situation with two different atoms in the unit cell, but this would give us a trivial insulating state. Haldane imagined introducing a second-neighbor hopping term, with different signs depending on the direction of hopping from the first to second neighbor. This would stem from some staggered magnetic flux, which breaks time reversal symmetry, but is equal to zero through the unit cell. The continuum version of the Haldane term acquires the form

$$\mathcal{H}_H = m_H \sigma_z \tau_z, \tag{2.36}$$

with opposite sign of the mass term at K and K'. This gapped system is a topological insulator, with the Hall conductance $\pm e^2/h$, depending on the sign of the Chern number, which can be ± 1. Solved in a semi infinite ribbon geometry, Haldane model will show a gapless state dispersing through the gap. This is the chiral edge state, which may cross the Fermi level multiple times with different group velocities. What remains robust is the difference between the right and left moving modes, which will be always equal to $C = \pm 1$. The idea of Kane and Mele was to construct two copies of the Haldane model – one for each spin direction $s_z = \pm 1$. With addition of spin, a time reversal invariant term emerges, which couples spin and orbital degrees of freedom

$$\mathcal{H}_{KM} = \lambda_{SO} \sigma_z \tau_z s_z. \tag{2.37}$$

In the lattice version of the Kane-Mele model there appears again a second neighbor hopping term, but it additionaly distinguishes between two spin species, for which this term has opposite signs. Because it is a doubled Haldane model, there are also two modes dispersing through the gap, however this time these are counterpropagating helical states with the spin locked to the momentum direction. Additionally, those states are immune to localization and will travel through a disordered medium without backscattering. One can show that the off-diagonal elements of the scattering matrix will vanish, as long as the time reversal symmetry is preserved. The problem remains, that the Chern number will be equal to zero in systems with time reversal invariance. If however the spin projection is a good quantum number, the difference between spin-up and spin-down Chern numbers will be $C_\uparrow - C_\downarrow = \pm 2$,

and can serve as an invariant. In reality the spins will be mixed and this recipe is no longer valid. Kane and Mele introduced a different topological index – the Z_2 invariant – in another seminal paper from 2005 [41]. The introduction of this Z_2 number is deeply involved, and we will retain to a comment about the invariant in centrosymmetric systems. If there is an inversion symmetry, a Kramers pair of eigenstates at time reversal invariant momenta Γ_i share an eigenvalue ξ_i of the parity operator P

$$\begin{aligned} P|u_n^I(\Gamma_i)\rangle &= \xi_i|u_n^I(\Gamma_i)\rangle, \\ P|u_n^{II}(\Gamma_i)\rangle &= \xi_i|u_n^{II}(\Gamma_i)\rangle \end{aligned} \tag{2.38}$$

with $\xi_i = \pm 1$ and the roman numerals label the Kramers partners. We can then evaluate the Z_2 index by computing

$$(-1)^\nu = \prod_i \xi_i, \tag{2.39}$$

which probes if the edge states dispersing through the gap connect pairwise at the time reversal invariant momenta. If not, the invariant is $(-1)^\nu = -1$ and the system is in the quantum spin Hall phase.

Topological superconductivity

Topological arguments are naturally extended from insulators to superconductors. After all, there is a gap in the spectrum of a superconductor, and states below the Fermi level are occupied. One can therefore define topological numbers for the occupied bands. Topological superconductivity is defined as a state with a fully opened gap, a non-zero topological invariant and the absence of gapless bulk excitations. Just as in the case of topological insulators, there will be gapless states only on the boundary between such a system, and a topologically trivial one. Depending on the bulk topology, the dispersion of those gapless states may be different; in the following paragraphs we wil focus on a nodal state with flat dispersion, and a chiral one, with a single state dispersing through the gap, similar to the quantum Hall state. The quasiparticle excitations in superconductors are a mixture or electrons and holes, so an eigenstate of the Bogoliubov de-Gennes Hamiltonian with energy E, has a partner with energy

$-E$. We see that a quasiparticle is essentialy the same as the antiparticle. A zero-energy fermionic excitation which comes to mind in this context is the Majorana fermion. Predicted in 1937 by Ettore Majorana, as a real solution of the Dirac equation, with a particle being its own antiparticle – a self-conjugate Dirac fermion [42]. In condensed matter, there are no real Majorana fermions known from high energy physics, rather there are emergent collective excitations of electrons [43]. In topological superconductors, the edge excitations are gapless, and their low energy description satisfies the massless Dirac equation, therefore the zero energy edge states are Majorana quasiparticles. The tremendous activity in researching the possible routes of obtaining a solid level of control of Majorana zero modes, comes from the prediction that they would serve as nonlocal qubits, because of their non-abelian statistics. The number of review papers elaborating on various means of inducing those exotic states in condensed matter systems is a testament to their relevance [44–48]. In the following we will shortly describe two types of systems, relevant to the contributions presented in Chapter 4.

Chiral superconductivity

The first demonstration of a chiral p-wave superconductor was put forward by Read and Green, with the gap structure explicitly breaking time reversal symmetry $\Delta_0(k_x \pm ik_y)$ [49]. This state supports Majorana zero modes on the edges and in the vortex cores. A simpler realization was desired, and it turned out that Dirac fermions with s-wave pairing will also produce the desired outcome [50]. It was challenging at the time to find a condensed matter system realizing this proposal, but when it turned out that a surface state of a topological insulator is a Dirac fermion, Fu and Kane proposed, in the groundbreaking paper, to put such a surface state in proximity to s-wave superconductor [51]. The Hamiltonian of this system becomes

$$\mathcal{H} = \begin{pmatrix} -i\sigma_i\partial_i - \mu & \Delta^* \\ \Delta & i\sigma_i\partial_i + \mu \end{pmatrix} \tag{2.40}$$

and hosts Majorana zero modes in vortices and on the edges. Another breakthrough demonstrates the important role of the Rashba spin-orbit interaction [10, 52]. In the basis of $\psi_{\boldsymbol{k}} = (c_{\boldsymbol{k}\uparrow}\ c_{\boldsymbol{k}\downarrow}\ c^\dagger_{-\boldsymbol{k}\uparrow}\ c^\dagger_{-\boldsymbol{k}\downarrow})^T$ the Hamiltonian of a system with s-wave pairing, Zeeman field

and Rashba spin-orbit interaction is the following

$$\mathcal{H}_{\boldsymbol{k}} = \begin{pmatrix} \varepsilon_{\boldsymbol{k}} + \boldsymbol{g}_{\boldsymbol{k}} \cdot \boldsymbol{\sigma} - \mu_B H_z \sigma_z & i\Delta\sigma_y \\ -i\Delta\sigma_y & -\varepsilon_{\boldsymbol{k}} + \boldsymbol{g}_{\boldsymbol{k}} \cdot \boldsymbol{\sigma}^* + \mu_B H_z \sigma_z \end{pmatrix} \tag{2.41}$$

with $\boldsymbol{g}_{\boldsymbol{k}} = 2\lambda(k_y, -k_x)$, present when the $z \to -z$ symmetry is broken. How this state is similar to a chiral p-wave superonductor can be seen by performing a unitary transformation $\mathcal{H}^{\mathcal{D}}_{\boldsymbol{k}} = \mathcal{D}\mathcal{H}_{\boldsymbol{k}}\mathcal{D}^\dagger$, with

$$\mathcal{D} = \frac{1}{\sqrt{2}} \begin{pmatrix} 1 & i\sigma_y \\ i\sigma_y & 1 \end{pmatrix}. \tag{2.42}$$

The dual Hamiltonian is now

$$\mathcal{H}^{\mathcal{D}}_{\boldsymbol{k}} = \begin{pmatrix} \Delta - \mu_B H_Z \sigma_z & -i\varepsilon_{\boldsymbol{k}}\sigma_y - i\boldsymbol{g}_{\boldsymbol{k}} \cdot \boldsymbol{\sigma}\sigma_y \\ i\varepsilon_{\boldsymbol{k}}\sigma_y + i\boldsymbol{g}_{\boldsymbol{k}} \cdot \boldsymbol{\sigma}\sigma_y & -\Delta + \mu_B H_Z \sigma_z \end{pmatrix}, \tag{2.43}$$

and we see that the spin-orbit coupling now serves as a triplet pairing component, similar to the Read & Green's proposal [49]. After a critical value of magnetic field is applied

$$\mu_B H_z > \sqrt{\varepsilon(0)^2 + \Delta^2}, \tag{2.44}$$

a topological gap opens and an edge state with linear dispersion $E \sim ck$ traverses the gap. Applying a strong field can of course destroy s-wave superconductivity, but the difficulty can be circumvented in various ways, and one of them is construction of heterostructures, e.g. a semiconductor 'sandwiched' between a magnetic insulator and a superconductor. The similarity between the system Eq. (2.41) and the chiral p-wave superconductor is additionally supported by the presence of Majorana zero modes in vortices, when the condition (2.44) is satisfied.

Nodal topological superconductivity

The superconducting order parameter in many unconventional superconductors vanishes in special points (or sometimes lines) called 'nodes'. As gapless systems, they are not classified by the ten symmetry classes mentioned in Sec. 2.2, however, they still host gapless, topologically

protected boundary modes. Additionally, the topological invariants that characterize nodal topological superconductors are momentum dependent. There are many systems predicted to realize this exotic phase, e.g. noncentrosymmetric superconductors [53] and Weyl superconductors [54], however as is usual with intrinsic unconventional phases, it is difficult to unambigously prove that they exist in nature. It is therefore desired to construct a nodal topological phase from simpler ingredients, just like in the case of chiral superconductivity designed by the mixture of singlet pairing, magnetic field and Rashba interaction. One such example is a nodal topological state of Ising superconductors. A class of materials called transition metal dichalcogenides (TMD) exhibits the unconventional Ising pairing. Viewed from the out-of-plane direction, TMDs show a honeycomb lattice with broken sublattice symmetry. This $y \to -y$ mirror symmetry breaking results in the so called Ising spin-orbit coupling. In contrast to Rashba coupling, it pins the electron spins to out-of-plane directions, and because of that Ising superconductors are remarkably tolerant of in-plane magnetic fields, with critical fields exceeding the Pauli limit by up to 6 times [55]. One can therefore expect that the combination of s-wave superconductivity (present in TMDs), Zeeman field and spin-orbit interactions will lead to the emergence of a topologically non-trivial phase. Indeed this is the case, as shown by He et al. [56]. The Ising coupling vanishes along the high symmetry lines $\Gamma - M$ in the hexagonal Brillouin zone. It is at the intersection of the normal Fermi surface and this line, that the superconducting gap vanishes upon application of the external, in-plane Zeeman field, leading to six pairs of point nodes with opposite chirality. Even though the time reversal symmetry is broken by the external field, an effective symmetry – a combination of time reversal and mirror symmetries is present, which together with the particle-hole symmetry ensure that there is also chiral symmetry. The system then falls into the BDI class (one of the ten symmetry classes mentioned before [39]) for any fixed k_y, and can be characterized by the winding number

$$\mathcal{W}(k_y) = \frac{1}{2\pi i} \int dk_x \; Tr \left[\mathcal{C} H_{\boldsymbol{k}}^{-1} \partial_{k_x} H_{\boldsymbol{k}} \right], \tag{2.45}$$

with $\mathcal{C}$ the chiral symmetry operator. Whenever the system is in the state with $\mathcal{W}(k_y) \neq 0$, flat Majorana bands connect the point nodes. Since they are flat, they do not have any

velocity and are localized on the edges on the system, which are not parallel to the zigzag termination. When projected onto this direction, the nodal points cancel each other. The proposal for detection of such localized Majorana states is therefore scanning tunneling spectroscopy. Below the critical magnetic field we expect a usual s-wave gap when probing the edge, whereas above the critical field (in the topologically non trivial state), there would be a V-shaped gap (characteristic for nodal states) with a pronounced zero-bias maximum.

Chapter 3

Methods

3.1 Bogoliubov-de Gennes equations

The initial applications of the Bogoliubov-de Gennes approach (BdG) consisted of analysis of quasiparticle exctitations around vortices. Significant increase in computing power allows for a treatment of more complicated structures and situations. The main appeal of the BdG method is the relative simplicity and attainability. Despite generically being a set of generalized Schrödinger equations, BdG approach is widely used to tackle a rich variety of phenomena, such as the exotic Majorana quasiparticles in a chain of magnetic adatoms [57], disorder in d-wave superconductors [58], or unconventional superconductivity induced by proximity of d_{xy} superconductor to a topological insulator [59], to name just a few. As mentioned above, the advances in local probing techniques, like the STM, revived the desire to theoretically access single-particle density of states in atomic scale, and for that the BdG approach is definitely apt. Below we will succinctly derive the Bogoliubov-de Gennes equations in their tight-binding version. This approach is generic, although we will essentially follow the program of Ref. [60], aside from slight differences in notation. We start with a Hamiltonian:

$$H = \sum_{\langle ij\rangle_n,\sigma} h_{ij\sigma} c^\dagger_{i\sigma} c_{i\sigma} + \sum_{\langle ij\rangle,\sigma,\sigma'} \lambda^{\sigma\sigma'}_{ij} c^\dagger_{i\sigma} c_{j\sigma'} + V \sum_i \left(\Delta_i c^\dagger_{i\uparrow} c^\dagger_{i\downarrow} + \Delta^*_i c_{i\downarrow} c_{i\uparrow} \right) \tag{3.1}$$

which is general enough to take into account various possibilities. The single particle term $h_{ij\sigma}$ contains spin-conserving hopping up to n-th nearest neighbors, but can also be equipped with different on-site terms, like the chemical potential (whose local change would serve as a non-magnetic impurity), sublattice potentials in appropriate systems and magnetic fields. Present is also a possible spin-orbit interaction, expressed as a hopping with a change in spin direction proportional to $\lambda_{ij}^{\sigma\sigma'}$. The last term expresses the on-site pairing with the pairing potential $V < 0$ and order parameter $\Delta_i = \langle c_{i\downarrow} c_{i\uparrow} \rangle$. The structure of the Hamiltonian obliges us to mind both spin and particle-hole spaces, thus computing four commutators:

$$\begin{aligned}
\big[c_{i\uparrow}, H\big] &= \sum_j h_{ij\uparrow} c_{j\uparrow} + \sum_j \lambda_{ij}^{\uparrow\downarrow} c_{j\downarrow} + V\Delta_i c_{j\downarrow}^\dagger \\
\big[c_{i\uparrow}^\dagger, H\big] &= -\sum_j h_{ji\uparrow} c_{j\uparrow}^\dagger - \sum_j \lambda_{ji}^{\uparrow\downarrow} c_{j\downarrow} - V\Delta_i^* c_{j\downarrow} \\
\big[c_{i\downarrow}, H\big] &= \sum_j h_{ij\downarrow} c_{j\downarrow} + \sum_j \lambda_{ij}^{\downarrow\uparrow} c_{j\downarrow} - V\Delta_i c_{j\uparrow}^\dagger \\
\big[c_{i\downarrow}^\dagger, H\big] &= -\sum_j h_{ji\downarrow} c_{j\downarrow}^\dagger - \sum_j \lambda_{ji}^{\downarrow\uparrow} c_{j\uparrow}^\dagger + V\Delta_i^* c_{j\uparrow},
\end{aligned} \tag{3.2}$$

instructs us that the Bogoliubov-Valatin transformation is a legitimate approach. We therefore express the electronic operators as linear combinations of electron-like and hole-like quasiparticles

$$c_{i\sigma} = {\sum_n}' (u_{i\sigma}^n \gamma_n - \sigma v_{i\sigma}^{n*} \gamma_n^\dagger), \quad c_{i\sigma}^\dagger = {\sum_n}' (u_{i\sigma}^{n*} \gamma_n^\dagger - \sigma v_{i\sigma}^n \gamma_n), \tag{3.3}$$

where the prime denotes summation over positive energy states labeled by n, and $\sigma = \pm 1$. We impose the effective Hamiltonian to be diagonal $H_\gamma = \sum_n E_n \gamma_n^\dagger \gamma_n + E_{const}$, and it is easy to check that

$$\big[\gamma_n^{(\dagger)}, H_\gamma\big] = (-) E_n \gamma_n^{(\dagger)}. \tag{3.4}$$

We now substitute Eq. (3.3) into the commutators Eq. (3.2) and by comparing the coefficients of terms with γ_n and $\gamma_n^\dagger$ from Eq. (3.4), we obtain the BdG equations, written concisely in a

matrix form:

$$\sum_j \hat{H}_{ij}\hat{\phi}_j = E_n\hat{\phi}_i, \tag{3.5}$$

where

$$\hat{H}_{ij} = \begin{pmatrix} h_{ij\uparrow} & \lambda_{ij}^{\uparrow\downarrow} & 0 & \Delta_i \\ \lambda_{ij}^{\downarrow\uparrow} & h_{ij\downarrow} & \Delta_i & 0 \\ 0 & \Delta_i^* & -h_{ij\uparrow}^* & \lambda_{ij}^{*\uparrow\downarrow} \\ \Delta_i^* & 0 & \lambda_{ij}^{*\downarrow\uparrow} & -h_{ij\downarrow}^* \end{pmatrix}, \tag{3.6}$$

and

$$\hat{\phi}_i = \begin{pmatrix} u_{i\uparrow} \\ u_{i\downarrow} \\ v_{i\uparrow} \\ v_{i\downarrow} \end{pmatrix}. \tag{3.7}$$

In order to access the effects which various elements of the Hamiltonian have on the spatial structure of the order parameter, we need to solve the set of BdG equations with a self-consistency condition and diagonalize the Hamiltonian matrix Eq. (3.6), first with a random or guessed distribution of Δ_i, and compute it in each iteration using

$$\Delta_i = \frac{V}{2}\sum_n{}' \left(u_{i\uparrow}^n v_{i\downarrow}^{n*} + u_{i\downarrow}^n v_{i\uparrow}^{n*}\right)\tanh\left(\frac{E_n}{2k_BT}\right), \tag{3.8}$$

until a desired accuracy is achieved. In most cases we are interested in the local density of states, which is proportional to the imaginary part of the retarded Green's function of the system $G_{i\sigma}^r(E)$ via the formula $\rho_{i\sigma}(E) = -\frac{1}{\pi}Im\{G_{i\sigma}^r(E)\}$. Using the Bogoliubov-Valatin transformation Eq. (3.3) in a familiar expression $G_{i\sigma} = \langle\langle c_{i\sigma}|c_{i\sigma}^\dagger\rangle\rangle$ we readily arrive at

$$\rho_{i\sigma}(E) = |u_{in\sigma}|^2\delta(E - E_n) + |v_{in\sigma}|^2\delta(E + E_n). \tag{3.9}$$

The Dirac delta is usually artificially broadened using Lorentzian or Gaussian distributions. We can see from the above reasoning, that after establishing the physical implications of a model we wish to study and thus constructing a Hamiltonian on a discretized lattice, our aim is to diagonalize the appropriate matrix and calculate the observables of interest using

the eigenvectors and eigenenergies. This task can be computationally demanding, as the size of matrix Eq. (3.6) is $4N$x$4N$ with N the number of lattice sites. Simulating large lattices is therefore problematic and one usually resorts to using exaggerated values of Δ, since for smaller systems, the average level spacing can be of the order of the superconducting gap.

3.2 Bond currents

Acquisition of the eigenvectors and eigenvalues of Eq. (3.6) can be additionally used for calculation of the bond current, i.e. the average flow of charge between sites of the lattice. Their relation with Shiba states was first established in Ref. [61], where the authors have shown that through the magnetoelectric effect, the supercurrents around the impurity are carried by the YSR states. To obtain the expression for the current we start from the continuity equation

$$\frac{\partial \rho_i}{\partial t} - \sum_j J_{ij} = 0, \tag{3.10}$$

where $\rho_i = \sum_\sigma c^\dagger_{i\sigma} c_{i\sigma}$ is the density operator. We now use the Heisenberg equation

$$i\hbar \frac{\partial \rho_i}{\partial t} = [\rho_i, H], \tag{3.11}$$

where H is the appropriate Hamiltonian of the studied system. As we are interested in obtaining a vector field which visualizes the flow of charge between sites, we drop any term that induces on-site charge fluctuations. This process leaves only the hopping terms of the Hamiltonian contributing to the final expression. After the evaluation of commutators and insertion of the Bogoliubov-Valatin transformation Eq. (3.3), we obtain for the current from site i

$$\langle J_i \rangle = -i \sum_{j,\sigma,\sigma'} {\sum_n}' \left[h_{ij}^{\sigma\sigma'} \left(u_{i\sigma}^{n*} u_{j\sigma'}^{n} f(E_n) + \sigma\sigma' v_{i\sigma}^{n} v_{j\sigma'}^{n*} f(-E_n) \right) - c.c \right]. \tag{3.12}$$

Here we work in the natural units $e \equiv \hbar \equiv 1$. In the above expression $h_{ij}^{\sigma\sigma'}$ will depend on the type of the hopping. It can be a usual, spin conserving hopping between the neighbors of arbitrary rank, and/or various strains of spin-orbit interactions. The magnetoelectric effect in the context of magnetic structures on a superconducting surface is neatly visualized in

the following argument. The effective Hamiltonian of the surface of a three dimensional material will contain a Rashba term, stemming from the lack of inversion symmetry, i.e. $H_{\boldsymbol{k}} = \boldsymbol{k}^2/2m\ + \lambda(\boldsymbol{\sigma} \times \boldsymbol{k}) \cdot \hat{\boldsymbol{z}}$. Therefore, an additional, spin-dependent contribution to the current will emerge, as can be seen by evaluating $\partial_{\boldsymbol{k}} H_{\boldsymbol{k}} = \boldsymbol{k}/m\ + \lambda \hat{\boldsymbol{z}} \times \boldsymbol{\sigma}$. Therefore the question of such effect being present because of a single impurity is perfectly valid. One additional remark is due in the context of bound states around magnetic impurities. As mentioned before, the Shiba states carry the supercurrents, as in the language of the T matrix approach, only the poles associated with them give rise to non-zero current. Furthermore the direction of the flow is reversed after the quantum phase transtition described in the previous Chapter. This statement is modified, and the situation more complicated when the structure of $h_{ij}^{\sigma\sigma'}$ contains non-trivial terms (cf. description of paper **III** in Chapter 4).

3.3 Majorana polarization

Since the first report of the elusive Majorana quasiparticles being detected in a mesoscopic transport experiment [62], there has been a good amount of debate, whether the zero-bias conductance peaks are really Majoranas. Both the Shiba states and Andreev bound states can without a doubt exist at zero energy in special cases, while the Kondo resonance is guaranteed to be centered around the Fermi level. Theoretical studies are naturally helpful in such a situation and provide different interpretations and ways to test the validity of experimental reports. An example is the proposal of measuring the profile of the supercurrent in a junction consisting of two superconductors connected by a nanowire [63]. As one can never obtain a true zero energy Majorana bound sate when using numerical methods, and a state which is arbitrarily close to zero is not an indisputable proof of a topologically non-trivial state, it is useful to possess various computational tools at one's disposal. When exploring systems harboring the exotic Majorana quasiparticles, one can resort to a quantity called Majorana polarization, It was introduced in Ref. [64] as a complex version of local density of states, suitable for the description of Majorana quasiparticles, but was valid only for a subset of systems. A generalization of this approach was provided in Ref. [65]. One can obtain it from the particle-hole operator, of which the Majorana bound states are eigenstates

with eigenvalue $|1|$. In the Nambu basis $\Psi_i = (c_{i\uparrow}, c_{i\downarrow}, c^\dagger_{i\downarrow}, -c^\dagger_{i\uparrow})^T$ the particle-hole operator takes on the form $\hat{\mathcal{C}} = e^{i\phi}\sigma_y\tau_y\hat{K}$, with $\hat{K}$ as the complex conjugation operator. If we are interested in the local Majorana polarization vector, we evaluate, using a wavefunction $\psi_i = (u_{i\uparrow}, u_{i\downarrow}, v_{i\downarrow}, v_{i\uparrow})^T$, the following:

$$\langle\psi|\hat{\mathcal{C}}_i|\psi\rangle = -2\sum_\sigma \sigma u^*_{i\sigma}v^*_{i\sigma}, \tag{3.13}$$

with $\hat{\mathcal{C}}_i = \hat{\mathcal{C}}\hat{r}_i$, where $\hat{r}_i$ is the projection onto site i. It is useful to inspect the real space map of Eq. (3.13), presented as a vector quantity, with the real and imaginary parts as x and y components. This way one can inspect if the state is a 'true' Majorana, for to be considered as such, in a region $\mathcal{R}$ where we expect a Majorana state to be localized, the vectors must be 'ferromagnetically' aligned. One can also verify this condition by evaluating whether

$$\frac{\left|\sum_{i\in\mathcal{R}}\langle\psi|\hat{\mathcal{C}}_i|\psi\rangle\right|}{\sum_{i\in\mathcal{R}}\langle\psi|\hat{r}_i|\psi\rangle} = 1, \tag{3.14}$$

when the region $\mathcal{R}$ is appropriately chosen. This method was succesfully employed to examine many different types of systems, as one dimensional wires, two dimensional strips or junctions between a normal metal and a superconductor [65, 66]. It can as well be used to study the topological phase diagram of recently fabricated, highly controllable topological Josephson junctions (cf. the description of paper **VI** in Chapter 4).

Chapter 4

Original contributions

We will now present a summary of results obtained in the papers constituting the thesis and state the author's input to them. The first paper emerged from a wish to check if there exist mechanisms, which may influence the spatial character of the YSR wave function. Recent experimental results at the time revealed that the dimensionality certainly plays a crucial role in this context [67]. Seeing that in the lattice version, the spin-orbit interaction is a hopping term, we have hypothesized that it may influence the spatial extent of bound states. In the second publication we have summarized the efforts of our group and coworkers in the general context of bound states, whether coming from impurities, their collections or highly controllable systems – quantum dots. The Yu-Shiba-Rusinov states were presented in a tight-binding version for a generic situation of a magnetic impurity in a square lattice. Having learned that spin-orbit interactions affect the Shiba states in an unusual manner, we have turned our attention to different flavors of the coupling between orbital and spin degrees of freedom. It turned out that the interactions capable of inducing the exciting topologically non-trivial phases were an interesting example. We have therefore studied the effect of the intrinsic spin-orbit coupling of honeycomb lattices, introduced as a necessary ingredient for the presence of the quantum spin Hall efffect in graphene [9] on the bound states induced by single magnetic impurity. The next paper was the result of reflecting on recent experimental breakthroughs – discovery of two dimensional ferromagnetism [68] and Ising superconductivity in transition metal dichalcogenides [55, 69]. We have envisioned a system, already known to harbor a rich topological phase diagram – a Shiba lattice [70, 71], but with important

differences. This time, it was the combination of Ising spin-orbit coupling (bearing similarities to the Kane-Mele term, albeit of different origin) and in-plane ferromagnetism, that yielded a topologically non-trivial, nodal superconducting phase. Being familiar with the Ising spin-orbit interaction proved useful in the project with the experimental group led by Peter Liljeroth from Aalto University. They have manufactured state of the art heterostructures using molecular beam epitaxy. Islands of ferromagnetic $CrBr_3$ on superconducting TMD – $NbSe_2$ revealed zero bias peaks on their edges when probed with scanning tunneling spectroscopy. We have established a theoretical model showing that this designer structure realizes topological superconductivity with 1D chiral Majorana modes on the edges of the islands. The most recent work, connected to a highly controllable topological Josephson junction focuses on the Majorana polarization introduced in Chapter 3. We have shown that its absolute value can be probed by polarized scanning spectroscopy and examined the influence of an electrostatic impurity on the spatial structure of Majorana bound states induced in the junction. Below we discuss the selected papers in more detail.

I. *Yu-Shiba-Rusinov states of impurities in a triangular lattice of $NbSe_2$ with spin-orbit coupling*, Phys. Rev. B **96**, 184425 (2017)
A. Ptok, S. Głodzik, T. Domański

Inspired by experimental results [67] showing that when the superconducting substrate is (*quasi*) two dimensional, the Shiba state wave function will spread significantly further in the lattice, we have examined a magnetic impurity embedded in a triangular lattice superconductor. Through numerical calculations we have shown that a spin-orbit interaction with its effective field acting in the plane of the substrate, the spatial length of YSR states can be additionally increased. We have also determined that this peculiar type of spin-orbit coupling will slightly affect the value of the critical coupling between the impurity and the superconducting host, at which the quantum phase transition

occurs. We have examined the spatial patterns of the YSR states (proportional to STM results), and by computing the displaced moving average of the YSR LDOS resolved the particle-hole oscillations measured in the aforementioned experiment. Lastly, we have presented the intereference between the YSR signals coming from magnetic dimers, and the influence of their relative position on such patterns.

Author's contribution: Analytical & numerical calculations. Preparation of the manuscript.

II. *Interplay between pairing and correlations in spin-polarized bound states*, Beilstein J. Nanotechnol. **2018**, 9, 1370–1380

S. Głodzik, A. Kobiałka, A. Gorczyca-Goraj, A. Ptok, G. Górski, M. M. Maśka, T. Domański

This paper reviews phenomena associated with the presence of magnetic adsorbates in contact with superconductors. From single impurities, through a chain of magnetic atoms, to an interpaly between the Kondo effect and Majorana modes in a setup with a quantum dot. The first part focuses on Yu-Shiba-Rusinov (YSR) states induced by a single magnetic impurity in a square lattice superconductor and shows the increase of their spatial extent due to an in-plane spin-orbit field. This is especially visible in the particle-hole oscillations, which show an increase of the spectral weight of the Shiba states away from the impurity sites, by almost an order of magnitude. Other characteristic features of YSR states are also present, albeit their topography is naturally different than in the case of triangular lattice.

Author's contribution: Analytical & numerical calculations presented in the paragraph „Single magnetic impurity".

III. *In-gap states of magnetic impurity in quantum spin Hall insulator proximitized to a superconductor*, J. Phys.: Condens. Matter **32** (2020) 235501
S. Głodzik, T. Domański

In this paper we have studied a single magnetic impurity embedded in a honeycomb lattice with proximity induced superconducting order. Because of the symmetries in such a lattice, a spin conserving, next-nearest-neighbor hopping term, called intrinsic spin-orbit coupling, or the Kane-Mele term is allowed [9]. The presence of this coupling drives the system into the topologically non-trivial state – the quantum spin Hall phase, with a Z_2 topological invariant [41]. We have established that the presence of the Kane-Mele term shifts the critical magnetic interaction J_C to higher values, and significantly reduces the spatial extent of Shiba-like states. Those are not strictly Yu-Shiba-Rusinov states, because the density of states in a honeycomb lattice vanishes at the Fermi energy, and the formula Eq. (2.27) would not yield a subgap state. Nevertheless there are bound states coming from the magnetic impurity, and we have observed that when the quantum spin Hall phase is not destroyed (e.g. by the chemical potential shift), there are two species of impurity bound states in the gap. One pair (Shiba-like) undergoes the quantum phase transition, while the other does not. There are usual manifestations of the change in the ground state: sign reversal of the order parameter at the impurity site, change in the bulk polarization and the reversal of the bond current. When inspected carefully, it turns out that only the current carried by the YSR-like states is reversed. Because of the competition of two flow directions, total current is drastically reduced after the phase transition.

Author's contribution: Analytical & numerical calculations. Preparation of the manuscript.

IV. *Engineering nodal topological phases in Ising superconductors by magnetic superstructures*, New J. Phys. **22** (2020) 013022
S. Głodzik, T. Ojanen

Motivated by the discovery of Ising superconductivity in TMDs [55,69] and the prediction of flat Majorana bands realized in this type of materials under in-plane magnetic fields [56], we have envisioned an island of classical spins pointing parallel to the plane on the surface of a superconducting TMD. Such a system is expected to enter a nodal (gapless) topological phase in which the flat Majorana bands would manifest as localized zero energy states. Those states are only present on the island edges parallel to the armchair termination of the lattice. This stems from the the structure of the point nodes (gap closings) in the momentum space. Their configuration additionally controls the degeneracy of the flat band, reflected in the value of the topological invariant – the integer winding number.

Author's contribution: Analytical & numerical calculations. Preparation of the manuscript.

V. *Topological superconductivity in a designer ferromagnet-superconductor van der Waals heterostructure*, arXiv:2002.02141
S.Kezilebieke, M. Nurul Huda, V. Vaňo, M. Aapro, S. C. Ganguli, O. J. Silveira, S. Głodzik, A. S. Foster, T. Ojanen, P.Liljeroth

Two dimensional topological superconductivity induced by magnetic impurities has been proposed theoretically [70, 71] and observed experimentally [72, 73], altough there is some debate concerning the robustness and scalability of the experimental results. By designing a structure comprising two types of van der Waals materials – $NbSe_2$ and $CrBr_3$, which exhibit two competing electronic orders (superconductivity and ferromagnetism respectively), we show that the system is in the topological supercon-

ducting state with pronounced zero-bias peaks on the edges of the islands. Those edge states, revealed by the STM data and theoretical calculations, are the celebrated chiral Majorana states, proposed as building blocks for topological quantum computation. The theoretical model correctly predicts that in the phase with the Chern number $C = 3$ the edge states are the most prominent excitation even at energies close to the topological gap. Their exponential localization at the island edges is also consistent, as well as the apparent (but not real) discontinuity of the edge state, stemming from interference effects due to irregularities of the boundary.

Author's contribution: Establishing the theoretical model and performing the momentum & real space numerical calculations.

VI. *How to measure a Majorana: The Majorana polarization of a topological planar Josephson junction* , arXiv:2004.01420

S. Głodzik, N. Sedlmayr, T. Domański

It has been first predicted theoretically [74, 75] and then shown experimentally [76, 77] that a topological Josephson junction can be driven into a topologically non-trivial state using the phase difference between the superconducting electrodes. The quasi-one-dimensional barrier between the two leads hosts Majorana bound states which are remarkably robust. We test this robustness by calculating the Majorana polarization for different widths of the barrier and show that this value can be probed using polarized Andreev spectroscopy. Additionally we examine the influence of a strong point-like electrostatic impurity and show that when placed close to the end of the normal region, it can localize one of the Majorana bound states, leaving the other one virtually unaffected. We also confirm the phase diagram using the polarization criterion.

Author's contribution: Numerical calculations. Preparation of the manuscript.

Yu-Shiba-Rusinov states of impurities in a triangular lattice of $NbSe_2$ with spin-orbit coupling

Andrzej Ptok,[1,2,*] Szczepan Głodzik,[2,†] and Tadeusz Domański[2,‡]

[1]*Institute of Nuclear Physics, Polish Academy of Sciences, ul. E. Radzikowskiego 152, 31-342 Kraków, Poland*

[2]*Institute of Physics, Marie Curie-Skłodowska University, pl. Marii Skłodowskiej-Curie 1, PL-20031 Lublin, Poland*

(Received 5 July 2017; revised manuscript received 31 October 2017; published 22 November 2017)

We study the topography of the spin-polarized bound states of magnetic impurities embedded in a triangular lattice of a superconducting host. Such states have been observed experimentally in 2H-$NbSe_2$ crystal [G. C. Ménard *et al.*, Nat. Phys. **11**, 1013 (2015)], and they revealed oscillating particle-hole asymmetry extending to tens of nanometers. Using the Bogoliubov–de Gennes approach, we explore the Yu-Shiba-Rusinov states in the presence of spin-orbit interaction. We also study the bound states of double impurities for several relative positions in a triangular lattice.

DOI: 10.1103/PhysRevB.96.184425

I. INTRODUCTION

Magnetic impurities are detrimental for Cooper pairs because they induce spin-polarized subgap states [1–3] and (when impurities are dense enough) partly suppress or completely fill in the energy gap of the superconducting sample. Such in-gap quasiparticles, dubbed Yu-Shiba-Rusinov (YSR) states [4–6], have been observed experimentally in various systems [7–14]. They always exist in pairs, appearing symmetrically with respect to the chemical potential (treated here as the "zero-energy" reference level). Their energies can be controlled either electrostatically or magnetically [14]. Another feature is their spin-polarization evidenced by the asymmetric conductance at opposite voltages [15,16].

The bound states formed at magnetic impurities in three-dimensional isotropic superconductors are usually characterized by a relatively short spatial extent [17]. Contrary to that, in two-dimensional (2D) lattices, Ménard *et al.* [11] have reported different behavior, displaying a much longer extent of the YSR states with alternating (oscillating) particle-hole spectral weights. Furthermore, the bound states of impurities in superconducting 2H-$NbSe_2$ [18] with *quasi*-2D triangular lattice structure and strong spin-orbit coupling [19] have revealed the long-range coherent structures of a star-shape, whereas molecular dimers developed more complex spatial features [20].

Bulk crystals of 2H-$NbSe_2$ are characterized by centrosymmetric ($P6_3/mmc$) structure, formed by the stacking of noncentrosymmetric layers [21,22] [Fig. 1(a)]. Every layer is arranged in a honeycomb structure, comprising Nb and Se sublattices. Local inversion symmetry breaking [23–25] gives rise to the out-of-plane spin polarization [21] in every layer. At $T_{CDW} \approx 33$ K, there appears charge-density order [22,26,27], and below $T_c \approx 7$ K [21] the superconducting state sets in.

The normal state Fermi surface, studied by angle-resolved photoemission spectroscopy (ARPES) [21,27–30], has revealed two pairs of Nb-derived pockets, which are trigonally warped around a central Γ point and at the corner of the (hexagonal) first Brillouin zone. *Ab initio* (DFT) calculations indicated that the Fermi surface sheets originate predominantly from Nb 4*d* orbitals [21,31–33]. As a consequence, a triangular lattice formed by Nb atoms plays an important role for the superconducting state of this compound [34] and implies further a unique starlike shape of the bound states.

Contrary to bulk systems, the Fermi surface of the single monolayer 2H-$NbSe_2$ consists of only the pockets around the corner points of the Brillouin zone [21], whose size depends on the spin polarization [Fig. 1(b)]. The latter effect originates from the in-plane spin-orbit field [19,30]. Coupling of the spin to the *valley* distinguishes between nonequivalent parts of the Brillouin zone. Similar behavior has also been observed in other materials with hexagonal lattice structures [36–39].

Motivated by the recent experimental results of Ménard *et al.* [11], we study the YSR states of magnetic impurities embedded in a triangular lattice of the 2D superconducting host. The single monolayer of the 2H-$NbSe_2$ can be treated as a two-dimensional triangular lattice [34] with an in-plane spin-orbit field (in the supplemental material, we take into account also the out-of-plane spin-orbit component, which might be realized in other compounds [40,41]).

In Sec. II we present the microscopic model and discuss some methodological details. Next, in Sec. III A, we analyze the YSR bound states of a single magnetic impurity in a

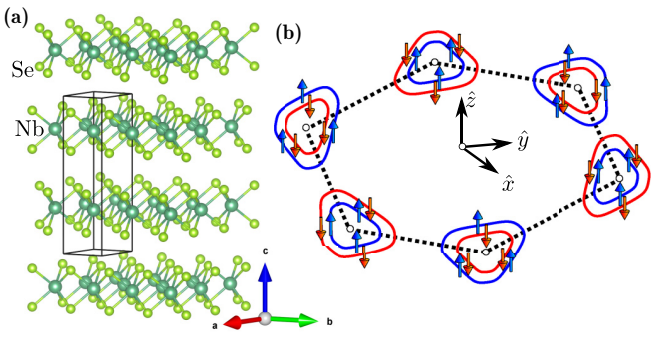

FIG. 1. (a) Crystallographic structure of the centrosymmetric $NbSe_2$ compound and its primitive unit cell (black prism). The image was obtained using VESTA software [35]. (b) Schematic view of the Fermi surface in the $NbSe_2$ monolayer, adopted from Ref. [21]. Blue (red) corresponds to different spin [negative (positive)] polarizations for each Fermi sheet in the zone corners.

*aptok@mmj.pl
†szglodzik@kft.umcs.lublin.pl
‡doman@kft.umcs.lublin.pl

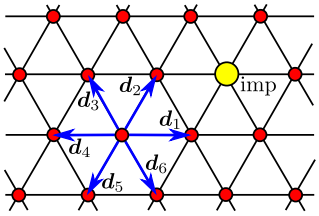

FIG. 2. Schematic illustration of a single magnetic impurity (yellow) in a two-dimensional triangular lattice. Each lattice site is surrounded by six nearest neighbors at positions $\boldsymbol{d}_\alpha$.

triangular lattice (Fig. 2), focusing on the role of spin-orbit coupling. In Sec. III B we study the bound states of double magnetic impurities (arranged in three different configurations) that might be relevant to the experimental data [20] revealing strong interference effects. Finally, in Sec. IV we summarize the main results.

II. MODEL AND METHOD

Magnetic impurities embedded in a 2D superconducting host with spin-orbit coupling can be described by the following Hamiltonian:

$$\hat{\mathcal{H}} = \hat{\mathcal{H}}_0 + \hat{\mathcal{H}}_{\rm imp} + \hat{\mathcal{H}}_{\rm int} + \hat{\mathcal{H}}_{\rm SOC}. \tag{1}$$

The single-particle term

$$\hat{\mathcal{H}}_0 = -t \sum_{\langle i,j\rangle\sigma} \hat{c}^\dagger_{i\sigma}\hat{c}_{j\sigma} - \mu \sum_{i\sigma} \hat{c}^\dagger_{i\sigma}\hat{c}_{i\sigma} \tag{2}$$

describes the kinetic energy of electrons, where $\hat{c}^\dagger_{i\sigma}$ ($\hat{c}_{i\sigma}$) denotes the creation (annihilation) of an electron with spin σ at the ith lattice site, t is a hopping integral between the nearest neighbors, and μ is the chemical potential. Large spin S of the impurities can be treated classically [1,2], and in such a case the interaction potential can comprise the magnetic J and nonmagnetic K parts,

$$\hat{\mathcal{H}}_{\rm imp} = -J(\hat{c}^\dagger_{0\uparrow}\hat{c}_{0\uparrow} - \hat{c}^\dagger_{0\downarrow}\hat{c}_{0\downarrow}) + K(\hat{c}^\dagger_{0\uparrow}\hat{c}_{0\uparrow} + \hat{c}^\dagger_{0\downarrow}\hat{c}_{0\downarrow}). \tag{3}$$

We describe the superconducting state, imposing the on-site interaction

$$\hat{\mathcal{H}}_{\rm int} = U \sum_i \hat{c}^\dagger_{i\uparrow}\hat{c}_{i\uparrow}\hat{c}^\dagger_{i\downarrow}\hat{c}_{i\downarrow} \tag{4}$$

with attractive potential $U < 0$. Such effective pairing is assumed to be weak, therefore we can treat it within the standard mean-field decoupling

$$\begin{aligned}\hat{c}^\dagger_{i\uparrow}\hat{c}_{i\uparrow}\hat{c}^\dagger_{i\downarrow}\hat{c}_{i\downarrow} = {}& \chi_i \hat{c}^\dagger_{i\uparrow}\hat{c}^\dagger_{i\downarrow} + \chi_i^* \hat{c}_{i\downarrow}\hat{c}_{i\uparrow} - |\chi_i|^2 \\ & + n_{i\uparrow}\hat{c}^\dagger_{i\downarrow}\hat{c}_{i\downarrow} + n_{i\downarrow}\hat{c}^\dagger_{i\uparrow}\hat{c}_{i\uparrow} - n_{i\uparrow}n_{i\downarrow},\end{aligned} \tag{5}$$

where $\chi_i = \langle \hat{c}_{i\downarrow}\hat{c}_{i\uparrow}\rangle$ is the superconducting order parameter and $n_{i\sigma} = \langle \hat{c}^\dagger_{i\sigma}\hat{c}_{i\sigma}\rangle$ is the average number of spin σ particles at the ith site. The Hartree term can be incorporated into the *effective* local spin-dependent chemical potential $\mu \to \tilde{\mu}_{i\sigma} \equiv \mu - U n_{i\bar{\sigma}}$. As we shall see, impurities suppress the local order parameter χ_i whose magnitude and sign depend on the coupling strength J [42,43].

The spin-orbit coupling (SOC) can be expressed by [44]

$$\hat{\mathcal{H}}_{\rm SOC} = -i\lambda \sum_{ij\sigma\sigma'} \hat{c}^\dagger_{i+\boldsymbol{d}_j\sigma}(\boldsymbol{d}_j \times \hat{\boldsymbol{\sigma}}^{\sigma\sigma'})\cdot\hat{w}\,\hat{c}_{i\sigma'}, \tag{6}$$

where the vector $\boldsymbol{d}_j = (d_j^x, d_j^y, 0)$ corresponds to the nearest neighbors of the ith site (Fig. 2), and $\hat{\boldsymbol{\sigma}} = (\sigma_x, \sigma_y, \sigma_z)$ consists of the Pauli matrices. The unit vector $\hat{w}$ shows a direction of the spin-orbit field, which in general can be arbitrary, but we restrict our considerations to the in-plane $\hat{w} \equiv \hat{x} = (1,0,0)$ and out-of-plane $\hat{z} = (0,0,1)$ polarizations, so formally we have

$$(\boldsymbol{d}_j \times \hat{\boldsymbol{\sigma}})\cdot\hat{w} = \begin{cases} d_j^y\sigma_z & \text{for in-plane field,} \\ d_j^x\sigma_y - d_j^y\sigma_x & \text{for out-of-plane field.}\end{cases} \tag{7}$$

Let us notice that the out-of-plane component mixes $\uparrow$ and $\downarrow$ particles, whereas the in-plane field corresponds to additional spin-conserving hopping with the spin- and direction-dependent amplitude.

Bogoliubov–de Gennes technique

Magnetic impurities break the translational invariance of the system, therefore the local pairing amplitude χ_i and occupancy $n_{i\sigma}$ have to be determined for each lattice site individually [45]. One can diagonalize the Hamiltonian (1) via the following unitary transformation:

$$\hat{c}_{i\sigma} = \sum_n (u_{in\sigma}\hat{\gamma}_n - \sigma v^*_{in\sigma}\hat{\gamma}^\dagger_n), \tag{8}$$

where $\hat{\gamma}_n$ and $\hat{\gamma}^\dagger_n$ are *quasi*particle fermionic operators, with the eigenvectors $u_{in\sigma}$ and $v_{in\sigma}$. This leads to the Bogoliubov–de Gennes (BdG) equations [46]

$$\mathcal{E}_n \begin{pmatrix} u_{in\uparrow} \\ v_{in\downarrow} \\ u_{in\downarrow} \\ v_{in\uparrow}\end{pmatrix} = \sum_j \begin{pmatrix} H_{ij\uparrow} & D_{ij} & S^{\uparrow\downarrow}_{ij} & 0 \\ D^*_{ij} & -H^*_{ij\downarrow} & 0 & S^{\downarrow\uparrow}_{ij} \\ S^{\downarrow\uparrow}_{ij} & 0 & H_{ij\downarrow} & D_{ij} \\ 0 & S^{\uparrow\downarrow}_{ij} & D^*_{ij} & -H^*_{ij\uparrow}\end{pmatrix} \begin{pmatrix} u_{jn\uparrow} \\ v_{jn\downarrow} \\ u_{jn\downarrow} \\ v_{jn\uparrow}\end{pmatrix} \tag{9}$$

containing the single-particle term $H_{ij\sigma} = -t\delta_{\langle i,j\rangle} - [\tilde{\mu}_{i\sigma} + (K - \sigma J)\delta_{i0}]\delta_{ij} + S^{\sigma\sigma}_{ij}$ and the spin-orbit coupling term $S^{\sigma\sigma'}_{ij} = -i\lambda\sum_l (\boldsymbol{d}_l \times \hat{\boldsymbol{\sigma}}^{\sigma\sigma'})\cdot\hat{w}\,\delta_{j,i+\boldsymbol{d}_l}$. Here, $S^{\sigma\sigma}_{ij}$ and $S^{\sigma\bar{\sigma}}_{ij}$ correspond to the in-plane and out-of-plane spin-orbit field, respectively, which satisfy $S^{\sigma\sigma'}_{ij} = (S^{\sigma'\sigma}_{ji})^*$, and $D_{ij} = U\chi_i\delta_{ij}$ describes the on-site pairing. The superconducting order parameter χ_i and occupancy $n_{i\sigma}$ can be computed self-consistently from the BdG equations (9),

$$\chi_i = \sum_n [u_{in\downarrow}v^*_{in\uparrow} f(\mathcal{E}_n) - u_{in\uparrow}v^*_{in\downarrow} f(-\mathcal{E}_n)], \tag{10}$$

$$n_{i\sigma} = \sum_n [|u_{in\sigma}|^2 f(\mathcal{E}_n) + |v_{in\bar{\sigma}}|^2 f(-\mathcal{E}_n)], \tag{11}$$

where $f(\omega) = 1/[1 + \exp(\omega/k_BT)]$ is the Fermi-Dirac distribution. In particular, the spin-resolved local density of states

(LDOS) is given by [47]

$$\rho_{i\sigma}(\omega) = \sum_n [|u_{in\sigma}|^2 \delta(\omega - \mathcal{E}_n) + |v_{in\sigma}|^2 \delta(\omega + \mathcal{E}_n)]. \quad (12)$$

For its numerical determination, we have replaced the Dirac δ function by the Lorentzian $\delta(\omega) = \zeta/[\pi(\omega^2 + \zeta^2)]$ with a small broadening $\zeta = 0.025t$.

III. NUMERICAL RESULTS AND DISCUSSION

We now present the BdG results obtained for the single impurity embedded in a triangular lattice (Sec. III A) and for several configurations of two magnetic impurities (Sec. III B). Numerical computations have been done at zero temperature for the finite cluster $N_a \times N_b = 41 \times 41$, assuming $U/t = -3$, $\mu/t = 0$, $K/t = 0$, and determining the bound states for varying J. In this work, we focus on the effect of an in-plane spin-orbit field, and additional results for the out-of-plane SOC are shown in the Supplemental Material (SM) [48].

A. Single magnetic impurity

Let us start by discussing the results obtained in the absence of spin-orbit coupling. A typical quasiparticle spectrum is displayed in Fig. 3, where we can recognize the gapped region $|\omega| \leqslant \Delta$ of the superconducting host (for our set of model parameters $\Delta \simeq 0.65t$) and one pair of the bound states, appearing symmetrically around the chemical potential. The energies $\pm E_\alpha$ of these states and spectral weights depend on the coupling J. In particular, at some critical J_c (indicated by black arrows) they eventually cross each other. This crossing is a hallmark of the quantum phase transition (QPT) [49] in which the ground state undergoes a qualitative evolution [15]. When magnetic coupling overcomes the pairing energy (for $|J| \geqslant J_c$), the particle and hole states become degenerate, and the ground state changes from a BCS singlet to a spinful configuration [15,50–52].

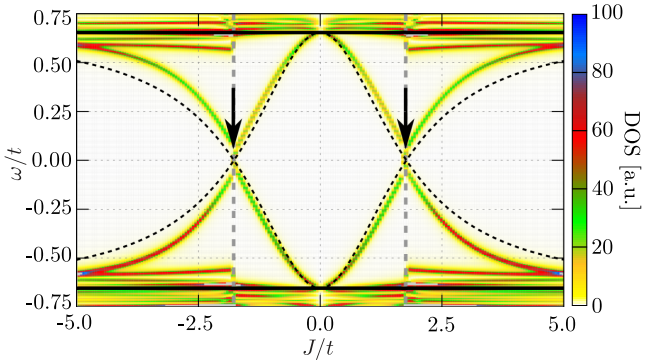

FIG. 3. Evolution of the low-energy spectrum with respect to the magnetic coupling J. The solid black line shows the magnitude of the pairing gap in regions far away from the impurity, black arrows point to the quantum phase transition (i.e., crossing of the subgap YSR states), and thin-dashed lines display the YSR bound states calculated from Eq. (13). Results were obtained without the SOC.

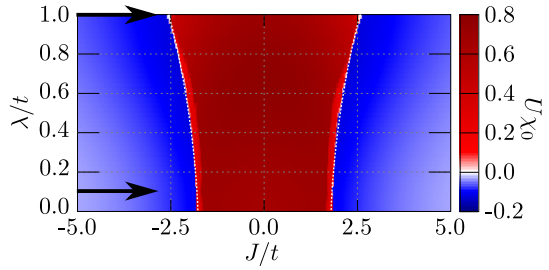

FIG. 4. Influence of the in-plane SOC on the critical value J_c. Blue and red correspond to the discontinuous change of $U\chi_0$ at the impurity site, and a white line marks the QPT. Black arrows indicate two values of λ, for which the profiles are shown in Fig. 5.

Our BdG data can be confronted with the analytical results of the thermodynamic limit $N_a \times N_b \to \infty$ [50]:

$$E_{\mathrm{YSR}} = \pm\Delta \frac{1-\alpha^2}{1+\alpha^2}, \quad (13)$$

where $\alpha = \pi\rho_0 J$ is the dimensionless impurity coupling parameter, ρ_0 is the normal state DOS at the Fermi level, and Δ is the superconducting gap. These quasiparticle energies (13) are displayed in Fig. 3 by a thin-dashed line. In the weak-coupling limit $|J| \leqslant J_c$, the formula (13) matches well with our numerical BdG results. Some differences appear above the QPT (for $|J| \geqslant J_c$), where the local pairing parameter at magnetic impurity is substantially reduced, affecting also the pairing gap of its neighboring sites. With an increasing coupling λ, the QPT is shifted to higher values (Fig. 4). The critical J_c corresponds to a value of J at which the YSR states cross each other. Variation of the critical J_c is caused by the influence of the SOC merely on the normal state DOS (ρ_0).

Such a quantum phase transition is manifested by a sign change of the order parameter χ_0 at the impurity site [Fig. 5(a)],

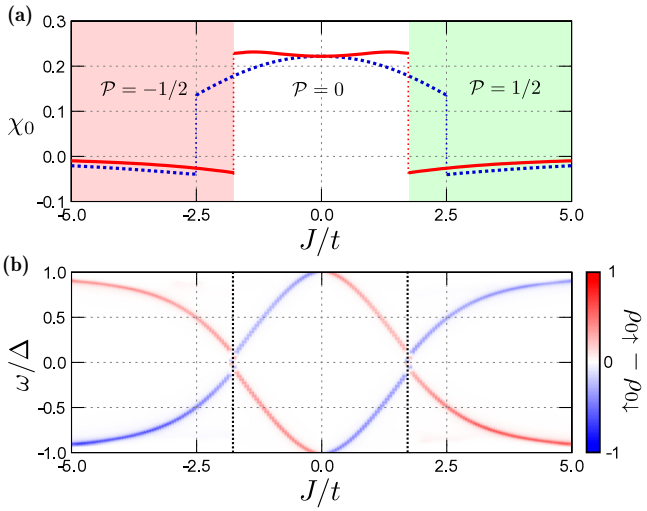

FIG. 5. The order parameter $\chi_0 = \langle \hat{c}_{0\downarrow}\hat{c}_{0\uparrow}\rangle$ obtained at the impurity site $i = 0$ (a) for the weak (red line) and strong (blue dotted line) spin-orbit couplings, with $\lambda/t = 0.1$ and 1.0, respectively. Magnetic polarization of the YSR states $\rho_{0\uparrow}(\omega) - \rho_{0\downarrow}(\omega)$ (b), obtained for $\lambda/t = 0.1$.

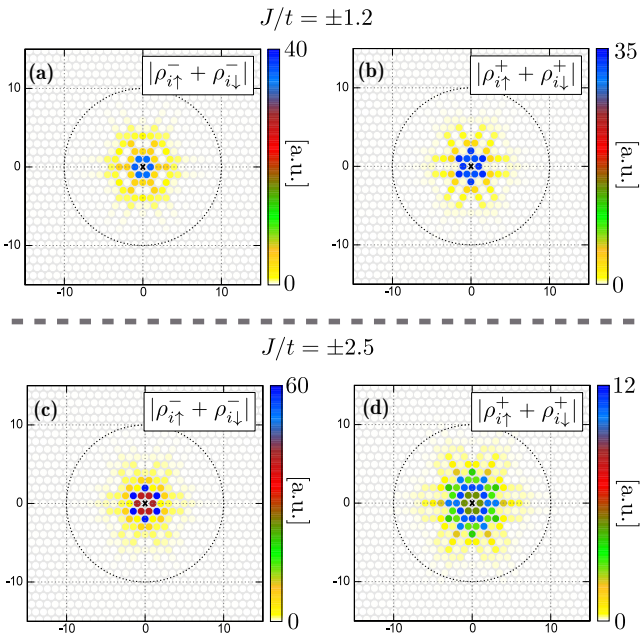

FIG. 6. Spatial patterns of the "negative" and "positive" YSR states $|\bar{\rho}^{\pm}_{i\uparrow} + \bar{\rho}^{\pm}_{i\downarrow}|$. Results are obtained for $J/t = \pm 1.2$ (top panel) and $J/t = \pm 2.5$ (bottom panel), assuming the in-plane spin-orbit coupling $\lambda/t = 0.1$.

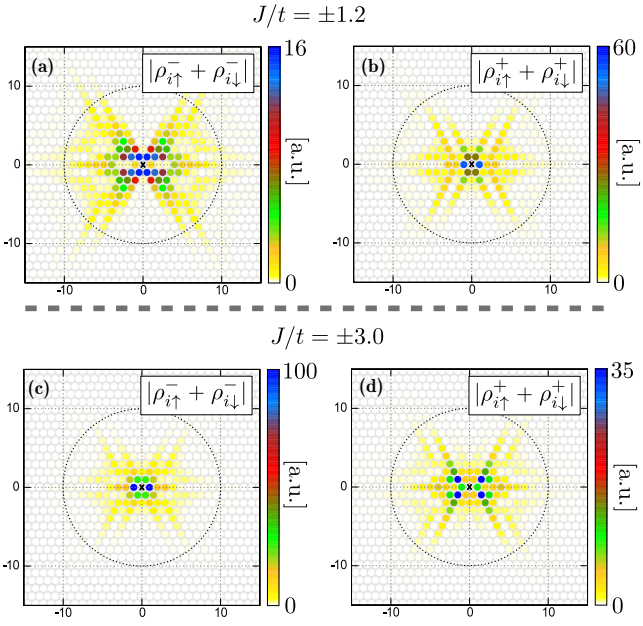

FIG. 7. The same as in Fig. 6, but for the stronger spin-orbit interaction $\lambda/t = 1$.

and discontinuity of its absolute value is a signature of the first-order phase transition [53–55]. Let us emphasize that the QPT is associated also with a reversal of the YSR polarization [Fig. 5(b)] and furthermore the total polarization of the system $\mathcal{P} = \frac{1}{2}\sum_i (n_{i\uparrow} - n_{i\downarrow})$ abruptly changes at $J = \pm J_c$ from zero to $\pm 1/2$ [56]. Similar behavior can be observed for multiple impurities [57].

In the weak-coupling limit (i.e., for $\lambda \ll t$), we can hardly notice any meaningful influence of SOC on the bulk superconductivity and the YSR states (see Fig. 1 in the SM [48]). A similar conclusion has been previously reported from the T-matrix treatment of magnetic impurities for 1D and 2D square lattices by Kaladzhyan *et al.* [52]. Our calculations have been done for $\lambda/t = 0.1$ which could be realistic for the $NbSe_2$ compound. Obviously for much stronger values of the spin-orbit coupling, both the superconducting state and the bound YSR states depend on the magnitude of λ and the direction of the magnetic moment [58].

Let us now explore the spatial extent of the YSR states. This can be achieved within the BdG approach by integrating the spectral weights

$$\rho^{\pm}_{i\sigma} = \int_{\omega_1}^{\omega_2} \rho_{i\sigma}(\omega) d\omega \tag{14}$$

in the interval $\omega \in (\omega_1, \omega_2)$ capturing every in-gap quasiparticle below or above the Fermi level [59]. Our numerical calculations have been done for the single impurity in the weak $J = -1.2t > -J_c$ and strong magnetic coupling limits $J = -2.5t < -J_c$, respectively. The results shown in Fig. 6 (notice different scales for each of these panels) reveal the characteristic six-leg star shape, whose extent spreads on several sites around the magnetic impurity. Spectral weights at the positive and negative energies are quite different, leading to a finite spin polarization of the YSR states (displayed in the bottom panel in Fig. 5).

Upon varying J, we observe that the star-shape (characterizing the C_6 symmetry of a triangular lattice) is rather robust. Such YSR state patterns could be probed by scanning tunneling microscopy, which nowadays has an atomic-scale resolution [8,12,60–62]. Let us emphasize that this six-leg star shape originates from a triangular lattice geometry and from the particular topology of the Fermi surface [63], in agreement with the experimental observations [11]. We have checked that the YSR states are only quantitatively (by a few percent) affected by the weak ($\lambda/t = 0.1$) in-plane spin-orbit coupling. For stronger SOC, the results are presented in Fig. 7. Comparison with Fig. 6 shows that for higher λ the YSR states gradually increase their extent, and the starlike shape seems to be weakly deformed with some elongation parallel to the x axis. Figure 7(a) presents an especially large range of bound states, extending well beyond ten lattice constants from the impurity site. As stated in the previous section, the in-plane spin-orbit field leads to the presence of the $S^{\sigma\sigma}_{ij}$ term in the single-particle part of the BdG equations, which directly affects the hopping amplitude. To observe the influence of this term on the spectral function, λ has to be of the order of t. We suspect that the large spatial extent of the YSR states reported in [11] was a consequence of the reduced dimensionality and/or the structure of the atomic lattice, and was not affected much by the in-plane spin-orbit field of $NbSe_2$. In general, however, materials with the stronger SOC couplings could reveal some increase in the spatial extent of subgap bound states.

For some quantitative analysis of the spatial profiles of YSR states, we define the *displaced moving average* (DMA) $\bar{\rho}^{\pm}(r)$ interpreted as an averaged spectral weight contained in a ring of radius r and its half-width δr. It depends only on

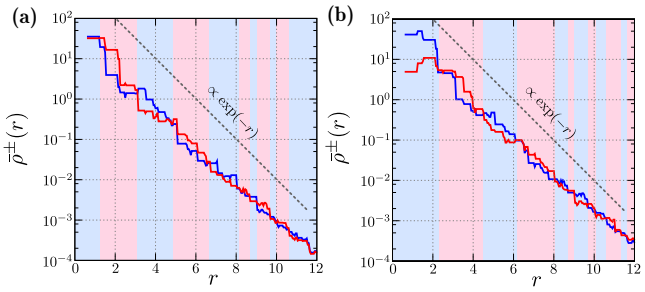

FIG. 8. Profiles of the hole- (blue line) and electron-like (red line) displaced moving average (DMA) for the YSR bound states $\bar{\rho}^{\pm}(r)$ as a function of distance r from the impurity (with $\delta r = 0.5$). The left and right panels correspond to $|J| < J_c$ and $|J| > J_c$, respectively. Results are obtained for the in-plane spin-orbit field $\lambda/t = 0.1$. The dashed gray line corresponds to $\exp(-r)$, which is a guide to eye. The blue (red) background indicates the dominant hole (particle) type of the YSR state at a given r.

a radial distance r from the magnetic impurity $\boldsymbol{r}_0$, averaging the angle-dependent fluctuations. Our results are presented in Fig. 8. They clearly show that functions $\bar{\rho}^{\pm}(r)$ of the YSR states are characterized by particle and hole oscillations that are opposite in phase (see the blue and red lines). Such particle-hole oscillations decay exponentially with distance (notice a logarithmic scale in Fig. 8), in agreement with previous studies [11,56,64]. In the 2D continuum version of this model, the wave functions of the YSR states have been expressed analytically [11]:

$$\psi^{\pm}(r) \propto \frac{1}{\sqrt{k_F r}} \sin\left(k_F r - \frac{\pi}{4} + \delta^{\pm}\right) \times \exp\left[-\sin(\delta^{+} - \delta^{-})\frac{r}{\zeta}\right], \quad (15)$$

where k_F is the Fermi wave vector, r is the distance from the impurity, whereas ζ is the superconducting coherence length. Both functions oscillate with $k_F r$, but with different scattering phase shifts $\delta^{\pm} = K\rho_0 \pm J/\rho_0$. At short distances, the YSR wave functions are governed by $\sin(k_F r)/\sqrt{k_F r}$, whereas for larger r the exponential envelope function suppresses particle-hole oscillations (see the dotted line in Fig. 8). Dominant (particle or hole) contributions to the YSR bound states are displayed by an alternating color of the background in Fig. 8. The period of such oscillations is approximately equal to nearly two lattice constants. The out-of-plane spin-orbit field leads to a similar behavior (Fig. 5 in [48]).

The quantum phase transition (at J_c) has consequences on a reversal of the magnetization induced near the impurity (see Fig. 9). For $|J| < J_c$, the impurity is weakly screened, whereas for stronger couplings, $|J| > J_c$, the impurity polarizes its neighborhood in the direction of its own magnetic moment. In both cases, this short-range magnetization does not coincide with the six-leg star shape of the bound states. Differences between the YSR wave functions and various components of magnetization have been previously discussed for a 2D square lattice by Kaladzhyan *et al.* [52].

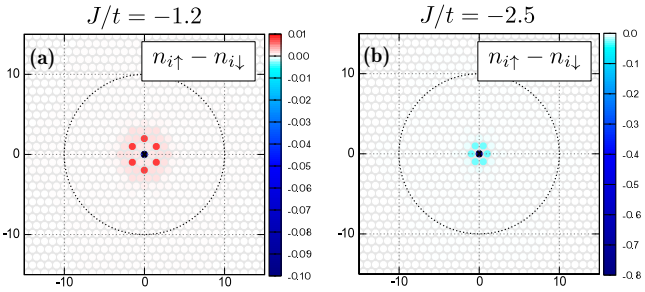

FIG. 9. Magnetization along the z axis induced near the magnetic impurity for $|J| < J_c$ (a) and $|J| > J_c$ (b).

B. YSR of double impurities

The BdG technique has the advantage that it can be easily applied to study the bound states of more numerous impurities, distributed at arbitrary positions in a crystallographic lattice. In this section, we consider the case of double magnetic impurities arranged in three different configurations displayed in Fig. 10(a). Our study of the YSR states is inspired by the results of Ref. [20] for ferromagnetic dimers. Such BdG calculations can be applied to more complex molecules [51,65–67] and/or multi-impurity structures [68–70]. It is well known [1] that multiple impurities can develop several quantum phase transitions with some characteristic features. They have been previously studied for 2D lattices, treating the spins classically [57,71,72] and taking into account the strong correlation effects within the Anderson-type scenario [73]. Here we explore the YSR states of two classical magnetic impurities embedded in a triangular lattice, assuming the weak in-plane spin orbit interaction $\lambda/t = 0.1$.

Figure 10 presents the subgap spectrum obtained for different configurations of the double impurities. We notice that coupling between the impurities induces the double-peak structure of YSR states, both at negative and positive energies [panel (b)]. Figure 11 displays spatial distributions of the YSR states for each configuration of the double magnetic impurities for the weak (left column) and strong (right column) couplings J. Although the C_6 rotational symmetry is broken, one can clearly see the mirror symmetry with respect to the axis

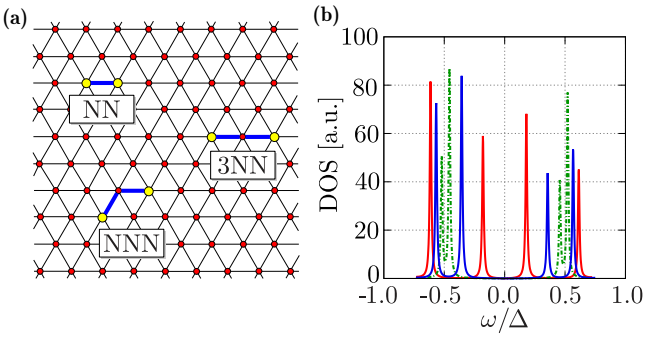

FIG. 10. Schematic illustration of two magnetic impurities arranged in three different configurations (a) and the subgap spectrum (b) for the nearest neighbors (NN), next nearest neighbors (NNN), and third nearest neighbors (3NN), as shown by red, blue, and green lines, respectively. We assumed the in-plane spin-orbit coupling $\lambda/t = 0.1$.

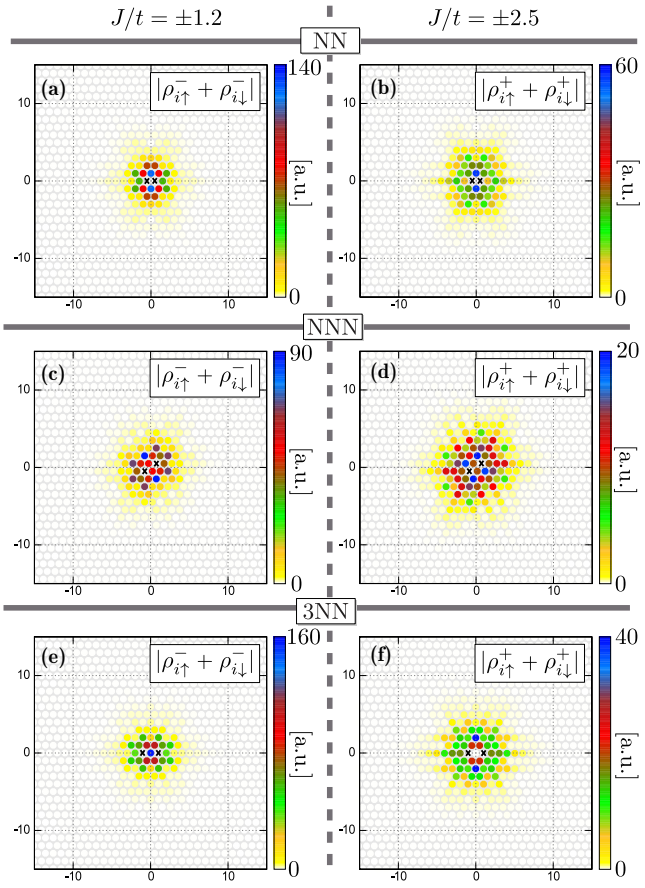

FIG. 11. Spatial pattern of the YSR states for the double magnetic impurities in different (NN, NNN, 3NN) configurations, as indicated. The left column panels refer to the weak coupling $J/t = -1.2$ and the right column panels to the strong coupling $J/t = -2.5$ limits, respectively. We imposed the in-plane spin-orbit coupling $\lambda/t = 0.1$ that could be relevant to $NbSe_2$.

connecting these double impurities and the axis perpendicular to it. Novel spatial patterns of the YSR states are due to the constructive/destructive quantum interference between the overlapping subgap states. Obviously, the most significant quantum interference occurs for the quantum impurities either at the nearest-neighbor (NN) or next-nearest-neighbor (NNN) configurations, with a clear bonding-antibonding splitting of the YSR quasiparticle energies. For more distant arrangements of the double impurities (for instance, 3NN), their spatial patterns gradually evolve back to the starlike shape. A more in-depth comparison of the results obtained with and without SOC is presented in [48] Figs. 6 and 7 of the SM. We hope that our theoretical predictions can be empirically verified, using the combined AFM (capable of manipulating the impurities) and STM (suitable for probing the subgap spectrum) techniques.

IV. CONCLUSIONS

In summary, we have investigated the energies and spatial extent of the Yu-Shiba-Rusinov (YSR) states induced by the classical magnetic impurities embedded in a two-dimensional triangular lattice of the 2H-$NbSe_2$ superconducting host. To study this particular crystallographic geometry in the presence of local inhomogeneities (in a form of the single or double impurities) and the spin-orbit coupling (SOC), we have adopted the Bogoliubov–de Gennes formalism.

In agreement with experimental observations [11], we have found that the YSR states acquire sixfold rotational symmetry (starlike patterns) whose spectroscopic signatures extend onto about a dozen of the intersite distances. Furthermore, their intertwining (π-shifted in phase) particle-hole oscillations are clearly visible. The weak spin-orbit coupling (which should be relevant to the 2H-$NbSe_2$ compound) has a rather negligible influence on the energies of YSR states, but for relatively stronger SOC their spatial extent eventually increases (beyond 10 lattice constants in some cases). Analysis of the SOC for the single impurity indicates that the extended range of YSR states reported in [11] stems from the dimensionality and/or the structure of an atomic lattice, rather than from the in-plane spin-orbit field of such materials.

We have also studied the subgap quasiparticle spectrum of double magnetic impurities in three different configurations, revealing either the constructive or destructive quantum interference that breaks C_6 symmetry of the YSR wave functions. Deviation from the starlike shape (typical for single impurities) depends on the relative distance between such magnetic impurities. When they are close to each other, the YSR states develop a double-peak structure (characteristic for the bonding and antibonding states) whose spatial patterns no longer resemble the star shape. With an increasing distance between the impurities, such bonding-antibonding splitting gradually disappears, and the spatial starlike shape of YSR states is gradually restored.

ACKNOWLEDGMENTS

We thank K. J. Kapcia for valuable comments and discussions. This work was supported by the National Science Centre (NCN, Poland) under Grants No. UMO-2016/20/S/ST3/00274 (A.P.) and No. DEC-2014/13/B/ST3/04451 (S.G. and T.D.)

[1] A. V. Balatsky, I. Vekhter, and J.-X. Zhu, Impurity-induced states in conventional and unconventional superconductors, Rev. Mod. Phys. **78**, 373 (2006).

[2] V. Koerting, B. M. Andersen, K. Flensberg, and J. Paaske, Nonequilibrium transport via spin-induced subgap states in superconductor/quantum dot/normal metal cotunnel junctions, Phys. Rev. B **82**, 245108 (2010).

[3] B. W. Heinrich, J. I. Pascual, and K. J. Franke, Single magnetic adsorbates on s-wave superconductors, arXiv:1705.03672.

[4] L. Yu, Bound state in superconductors with paramagnetic impurities, Acta Phys. Sin. **21**, 75 (1965).

[5] H. Shiba, Classical spins in superconductors, Prog. Theor. Exp. Phys. **40**, 435 (1968).

[6] A. I. Rusinov, Superconductivity near a paramagnetic impurity, Zh. Eksp. Teor. Fiz. Pisma Red. **9**, 146 (1968) [JETP Lett. **9**, 85 (1969)].

[7] A. Yazdani, B. A. Jones, C. P. Lutz, M. F. Crommie, and D. M. Eigler, Probing the local effects of magnetic impurities on superconductivity, Science **275**, 1767 (1997).

[8] S.-H. Ji, T. Zhang, Y.-S. Fu, X. Chen, X.-C. Ma, J. Li, W.-H. Duan, J-F. Jia, and Q.-K. Xue, High-Resolution Scanning Tunneling Spectroscopy of Magnetic Impurity Induced Bound States in the Superconducting Gap of Pb Thin Films, Phys. Rev. Lett. **100**, 226801 (2008).

[9] M. Ruby, F. Pientka, Y. Peng, F. von Oppen, B. W. Heinrich, and K. J. Franke, Tunneling Processes into Localized Subgap States in Superconductors, Phys. Rev. Lett. **115**, 087001 (2015).

[10] N. Hatter, B. W. Heinrich, M. Ruby, J. I. Pascual, and K. J. Franke, Magnetic anisotropy in Shiba bound states across a quantum phase transition, Nat. Commun. **6**, 8988 (2015).

[11] G. C. Ménard, S. Guissart, C. Brun, S. Pons, V. S. Stolyarov, F. Debontridder, M. V. Leclerc, E. Janod, L. Cario, D. Roditchev, P. Simon, and T. Cren, Coherent long-range magnetic bound states in a superconductor, Nat. Phys. **11**, 1013 (2015).

[12] D.-J. Choi, C. Rubio-Verdú, J. de Bruijckere, M. M. Ugeda, N. Lorente, and J. I. Pascual, Mapping the orbital structure of impurity bound states in a superconductor, Nat. Commun. **8**, 15175 (2017).

[13] A. Assouline, Ch. Feuillet-Palma, A. Zimmers, H. Aubin, M. Aprili, and J.-Ch. Harmand, Shiba Bound States Across the Mobility Edge in Doped InAs Nanowires, Phys. Rev. Lett. **119**, 097701 (2017).

[14] A. Jellinggaard, K. Grove-Rasmussen, M. H. Madsen, and J. Nygård, Tuning Yu-Shiba-Rusinov states in a quantum dot, Phys. Rev. B **94**, 064520 (2016).

[15] M. I. Salkola, A. V. Balatsky, and J. R. Schrieffer, Spectral properties of quasiparticle excitations induced by magnetic moments in superconductors, Phys. Rev. B **55**, 12648 (1997).

[16] M. E. Flatté and J. M. Byers, Local Electronic Structure of a Single Magnetic Impurity in a Superconductor, Phys. Rev. Lett. **78**, 3761 (1997).

[17] A. L. Fetter, Spherical impurity in an infinite superconductor, Phys. Rev. **140**, A1921 (1965).

[18] M. M. Ugeda, A. J. Bradley, Y. Zhang, S. Onishi, Y. Chen, W. Ruan, C. Ojeda-Aristizabal, H. Ryu, M. T. Edmonds, H.-Z. Tsai, A. Riss, S.-K. Mo, D. Lee, A. Zettl, Z. Hussain, Z.-X. Shen, and M. F. Crommie, Characterization of collective ground states in single-layer $NbSe_2$, Nat. Phys. **12**, 92 (2016).

[19] X. Xi, Z. Wang, W. Zhao, J.-H. Park, K. T. Law, H. Berger, L. Forro, J. Shan, and K. F. Mak, Ising pairing in superconducting $NbSe_2$ atomic layers, Nat. Phys. **12**, 139 (2016).

[20] S. Kezilebieke, M. Dvorak, T. Ojanen, and P. Liljeroth, Coupled Yu-Shiba-Rusinov states in molecular dimers on $NbSe_2$, arXiv:1701.03288.

[21] L. Bawden, S. P. Cooil, F. Mazzola, J. M. Riley, L. J. Collins-McIntyre, V. Sunko, K. W. B. Hunvik, M. Leandersson, C. M. Polley, T. Balasubramanian, T. K. Kim, M. Hoesch, J. W. Wells, G. Balakrishnan, M. S. Bahramy, and P. D. C. King, Spin-valley locking in the normal state of a transition-metal dichalcogenide superconductor, Nat. Commun. **7**, 11711 (2016).

[22] A. Meerschaut and C. Deudon, Crystal structure studies of the 3R-$Nb_{1.09}S_2$ and the 2H-$NbSe_2$ compounds: Correlation between nonstoichiometry and stacking type (= polytypism), Mater. Res. Bull. **36**, 1721 (2001).

[23] J. M. Riley, F. Mazzola, M. Dendzik, M. Michiardi, T. Takayama, L. Bawden, C. Granerød, M. Leandersson, T. Balasubramanian, M. Hoesch, T. K. Kim, H. Takagi, W. Meevasana, Ph. Hofmann, M. S. Bahramy, J. W. Wells, and P. D. C. King, Direct observation of spin-polarised bulk bands in an inversion-symmetric semiconductor, Nat. Phys. **10**, 835 (2014).

[24] X. Zhang, Q. Liu, J.-W. Luo, A. J. Freeman, and A. Zunger, Hidden spin polarization in inversion-symmetric bulk crystals, Nat. Phys. **10**, 387 (2014).

[25] J. M. Riley, W. Meevasana, L. Bawden, M. Asakawa, T. Takayama, T. Eknapakul, T. K. Kim, M. Hoesch, S. K. Mo, H. Takagi, T. Sasagawa, M. S. Bahramy, and P. D. C. King, Negative electronic compressibility and tunable spin splitting in WSe_2, Nat. Nanotechnol. **10**, 1043 (2015).

[26] J. A. Wilson, F. J. Di Salvo, and S. Mahajan, Charge-Density Waves in Metallic, Layered, Transition-Metal Dichalcogenides, Phys. Rev. Lett. **32**, 882 (1974).

[27] X. Zhu, Y. Cao, J. Zhang, E. W. Plummer, and J. Guo, Classification of charge density waves based on their nature, Proc. Natl. Acad. Sci. (U.S.A.) **112**, 2367 (2015).

[28] T. Yokoya, T. Kiss, A. Chainani, S. Shin, M. Nohara, and H. Takagi, Fermi surface sheet-dependent superconductivity in $2H$-$NbSe_2$, Science **294**, 2518 (2001).

[29] S. V. Borisenko, A. A. Kordyuk, V. B. Zabolotnyy, D. S. Inosov, D. Evtushinsky, B. Büchner, A. N. Yaresko, A. Varykhalov, R. Follath, W. Eberhardt, L. Patthey, and H. Berger, Two Energy Gaps and Fermi-Surface "Arcs" in $NbSe_2$, Phys. Rev. Lett. **102**, 166402 (2009).

[30] D. J. Rahn, S. Hellmann, M. Kalläne, C. Sohrt, T. K. Kim, L. Kipp, and K. Rossnagel, Gaps and kinks in the electronic structure of the superconductor $2H$-$NbSe_2$ from angle-resolved photoemission at 1 K, Phys. Rev. B **85**, 224532 (2012).

[31] K. Rossnagel, O. Seifarth, L. Kipp, M. Skibowski, D. Voß, P. Krüger, A. Mazur, and J. Pollmann, Fermi surface of $2H$-$NbSe_2$ and its implications on the charge-density-wave mechanism, Phys. Rev. B **64**, 235119 (2001).

[32] M. D. Johannes, I. I. Mazin, and C. A. Howells, Fermi-surface nesting and the origin of the charge-density wave in $NbSe_2$, Phys. Rev. B **73**, 205102 (2006).

[33] F. Flicker and J. van Wezel, Charge order from orbital-dependent coupling evidenced by $NbSe_2$, Nat. Commun. **6**, 7034 (2015).

[34] J. Á. Silva-Guillén, P. Ordejón, F. Guinea, and E. Canadell, Electronic structure of $2H$-$NbSe_2$ single-layers in the CDW state, 2D Mater. **3**, 035028 (2016).

[35] K. Momma and F. Izumi, *VESTA3* for three-dimensional visualization of crystal, volumetric and morphology data, J. Appl. Crystallogr. **44**, 1272 (2011).

[36] H. Zeng, J. Dai, W. Yao, D. Xiao, and X. Cui, Valley polarization in MoS_2 monolayers by optical pumping, Nat. Nanotech. **7**, 490 (2012).

[37] K. F. Mak, K. He, J. Shan, and T. F. Heinz, Control of valley polarization in monolayer MoS_2 by optical helicity, Nat. Nanotech. **7**, 494 (2012).

[38] R. Suzuki, M. Sakano, Y. J. Zhang, R. Akashi, D. Morikawa, A. Harasawa, K. Yaji, K. Kuroda, K. Miyamoto, T. Okuda, K. Ishizaka, R. Arita, and Y. Iwasa, Valley-dependent spin polarization in bulk MoS_2 with broken inversion symmetry, Nat. Nanotech. **9**, 611 (2014).

[39] B. Zhu, H. Zeng, J. Dai, Z. Gong, and X. Cui, Anomalously robust valley polarization and valley coherence in bilayer WS_2, Proc. Natl. Acad. Sci. (U.S.A.) **111**, 11606 (2014).

[40] S. Glass, G. Li, F. Adler, J. Aulbach, A. Fleszar, R. Thomale, W. Hanke, R. Claessen, and J. Schäfer, Triangular Spin-Orbit-Coupled Lattice with Strong Coulomb Correlations: Sn Atoms on a SiC(0001) Substrate, Phys. Rev. Lett. **114**, 247602 (2015).

[41] G. Sharma and S. Tewari, Yu-Shiba-Rusinov states and topological superconductivity in Ising paired superconductors, Phys. Rev. B **94**, 094515 (2016).

[42] E. D. B. Smith, K. Tanaka, and Y. Nagai, Manifestation of chirality in the vortex lattice in a two-dimensional topological superconductor, Phys. Rev. B **94**, 064515 (2016).

[43] S. L. Goertzen, K. Tanaka, and Y. Nagai, Self-consistent study of Abelian and non-Abelian order in a two-dimensional topological superconductor, Phys. Rev. B **95**, 064509 (2017).

[44] Y. Xu, Ch. Qu, M. Gong, and Ch. Zhang, Competing superfluid orders in spin-orbit-coupled fermionic cold-atom optical lattices, Phys. Rev. A **89**, 013607 (2014).

[45] A. Ptok and K. J. Kapcia, Probe-type of superconductivity by impurity in materials with short coherence length: The s-wave and η-wave phases study, Supercond. Sci. Technol. **28**, 045022 (2015).

[46] P. G. De Gennes, *Superconductivity of Metals and Alloys*, Advanced Books Classics Series (Westview, 1999).

[47] H. Matsui, T. Sato, T. Takahashi, S.-C. Wang, H.-B. Yang, H. Ding, T. Fujii, T. Watanabe, and A. Matsuda, BCS-Like Bogoliubov Quasiparticles in High-T_c Superconductors Observed by Angle-Resolved Photoemission Spectroscopy, Phys. Rev. Lett. **90**, 217002 (2003).

[48] See Supplemental Material at http://link.aps.org/supplemental/10.1103/PhysRevB.96.184425 for a comparison with results for out-of-plane spin-orbit coupling.

[49] A. Sakurai, Comments on superconductors with magnetic impurities, Prog. Theor. Phys. **44**, 1472 (1970).

[50] W. V. van Gerven Oei, D. Tanasković, and R. Žitko, Magnetic impurities in spin-split superconductors, Phys. Rev. B **95**, 085115 (2017).

[51] K. J. Franke, G. Schulze, and J. I. Pascual, Competition of superconducting phenomena and Kondo screening at the nanoscale, Science **332**, 940 (2011).

[52] V. Kaladzhyan, C. Bena, and P. Simon, Characterizing p-wave superconductivity using the spin structure of Shiba states, Phys. Rev. B **93**, 214514 (2016).

[53] M. Mashkoori, K. Björnson, and A. M. Black-Schaffer, Impurity bound states in fully gapped d-wave superconductors with subdominant order parameters, Sci. Rep. **7**, 44107 (2017).

[54] S. S. Pershoguba, K. Björnson, A. M. Black-Schaffer, and A. V. Balatsky, Currents Induced by Magnetic Impurities in Superconductors with Spin-Orbit Coupling, Phys. Rev. Lett. **115**, 116602 (2015).

[55] Sz. Głodzik and A. Ptok, Quantum phase transition induced by magnetic impurity, J. Supercond. Nov. Magn. (2017).

[56] D. K. Morr and N. A. Stavropoulos, Quantum interference between impurities: Creating novel many-body states in s-wave superconductors, Phys. Rev. B **67**, 020502 (2003).

[57] D. K. Morr and J. Yoon, Impurities, quantum interference, and quantum phase transitions in s-wave superconductors, Phys. Rev. B **73**, 224511 (2006).

[58] Y. Kim, J. Zhang, E. Rossi, and R. M. Lutchyn, Impurity-Induced Bound States in Superconductors with Spin-Orbit Coupling, Phys. Rev. Lett. **114**, 236804 (2015).

[59] J. Röntynen and T. Ojanen, Topological Superconductivity and High Chern Numbers in 2D Ferromagnetic Shiba Lattices, Phys. Rev. Lett. **114**, 236803 (2015).

[60] M. T. Randeria, B. E. Feldman, I. K. Drozdov, and A. Yazdani, Scanning Josephson spectroscopy on the atomic scale, Phys. Rev. B **93**, 161115 (2016).

[61] H. Kim, Y. Yoshida, Ch.-Ch. Lee, T.-R. Chang, H.-T. Jeng, H. Lin, Y. Haga, Z. Fisk, and Y. Hasegawa, Atomic-scale visualization of surface-assisted orbital order, arXiv:1706.09753.

[62] G. Reecht, B. Heinrich, H. Bulou, F. Scheurer, L. Limot, and G. Schull, Imaging isodensity contours of molecular states with STM, arXiv:1703.05622.

[63] A. Weismann, M. Wenderoth, P. Lounis, S. Zahn, N. Quaas, R. G. Ulbrich, P. H. Dederichs, and S. Blügel, Seeing the Fermi surface in real space by nanoscale electron focusing, Science **323**, 1190 (2009).

[64] T. Kawakami and X. Hu, Evolution of Density of States and a Spin-Resolved Checkerboard-Type Pattern Associated with the Majorana Bound State, Phys. Rev. Lett. **115**, 177001 (2015).

[65] D. Jacob, M. Soriano, and J. J. Palacios, Kondo effect and spin quenching in high-spin molecules on metal substrates, Phys. Rev. B **88**, 134417 (2013).

[66] J. Kügel, M. Karolak, A. Krönlein, J. Senkpiel, P.-J. Hsu, G. Sangiovanni, and M. Bode, State identification and tunable Kondo effect of MnPc on Ag(001), Phys. Rev. B **91**, 235130 (2015).

[67] J. O. Island, R. Gaudenzi, J. de Bruijckere, E. Burzurí, C. Franco, M. Mas-Torrent, C. Rovira, J. Veciana, T. M. Klapwijk, R. Aguado, and H. S. J. van der Zant, Proximity-Induced Shiba States in a Molecular Junction, Phys. Rev. Lett. **118**, 117001 (2017).

[68] S. Nakosai, Y. Tanaka, and N. Nagaosa, Two-dimensional p-wave superconducting states with magnetic moments on a conventional s-wave superconductor, Phys. Rev. B **88**, 180503 (2013).

[69] G. C. Ménard, S. Guissart, Ch. Brun, M. Trif, F. Debontridder, R. T. Leriche, D. Demaille, D. Roditchev, P. Simon, and T. Cren, Two-dimensional topological superconductivity in Pb/Co/Si(111), arXiv:1607.06353.

[70] J. L. Lado and J. Fernández-Rossier, Unconventional Yu-Shiba-Rusinov states in hydrogenated graphene, 2D Mater. **3**, 025001 (2016).

[71] S. Hoffman, J. Klinovaja, T. Meng, and D. Loss, Impurity-induced quantum phase transitions and magnetic order in conventional superconductors: Competition between bound and quasiparticle states, Phys. Rev. B **92**, 125422 (2015).

[72] T. Meng, J. Klinovaja, S. Hoffman, P. Simon, and D. Loss, Superconducting gap renormalization around two magnetic impurities: From Shiba to Andreev bound states, Phys. Rev. B **92**, 064503 (2015).

[73] R. Žitko, Numerical subgap spectroscopy of double quantum dots coupled to superconductors, Phys. Rev. B **91**, 165116 (2015).

BEILSTEIN JOURNAL OF NANOTECHNOLOGY

Interplay between pairing and correlations in spin-polarized bound states

Szczepan Głodzik[1], Aksel Kobiałka[1], Anna Gorczyca-Goraj[2], Andrzej Ptok[3], Grzegorz Górski[4], Maciej M. Maśka[2] and Tadeusz Domański[*1]

Full Research Paper

Open Access

Address:
[1]Institute of Physics, M. Curie-Skłodowska University, 20-031 Lublin, Poland, [2]Institute of Physics, University of Silesia, 41-500 Chorzów, Poland, [3]Institute of Nuclear Physics, Polish Academy of Sciences, 31-342 Kraków, Poland and [4]Faculty of Mathematics and Natural Sciences, University of Rzeszów, 35-310 Rzeszów, Poland

Email:
Tadeusz Domański[*] - doman@kft.umcs.lublin.pl

* Corresponding author

Keywords:
bound states in superconductors; Majorana quasiparticles; subgap Kondo effect

Beilstein J. Nanotechnol. **2018,** *9,* 1370–1380.
doi:10.3762/bjnano.9.129

Received: 15 December 2017
Accepted: 09 April 2018
Published: 07 May 2018

This article is part of the Thematic Series "Topological materials".

Guest Editor: J. J. Palacios

Abstract

We investigate single and multiple defects embedded in a superconducting host, studying the interplay between the proximity-induced pairing and interactions. We explore the influence of the spin–orbit coupling on energies, polarization and spatial patterns of the bound (Yu–Shiba–Rusinov) states of magnetic impurities in a two-dimensional square lattice. We also address the peculiar bound states in the proximitized Rashba chain, resembling the Majorana quasiparticles, focusing on their magnetic polarization that has been recently reported by S. Jeon et al. (*Science* **2017,** *358,* 772). Finally, we study leakage of these polarized Majorana quasiparticles into side-attached nanoscopic regions and confront them with the subgap Kondo effect near to the singlet–doublet phase transition.

Introduction

Magnetism is usually detrimental to superconductivity because it breaks the Cooper pairs (at the critical field strength H_{c2}). There are, however, a few exceptions in which these phenomena coexist, e.g., in iron pnictides [1], $CeCoIn_5$ [2]. Also, sometimes magnetic fields induce superconductivity [3]. Plenty of other interesting examples can be found in nanoscopic systems, where magnetic impurities (dots) exhibit a more subtle relationship with the electron pairing driven by the proximity effect [4,5]. Cooper pairs easily penetrate the nanoscopic impurities, inducing the bound (Yu–Shiba–Rusinov) states that manifest the local pairing in coexistence with magnetic polarization. Such bound states have been observed in various systems [6-14]. In-gap states (appearing in pairs symmetrically around the Fermi level) can be nowadays controlled electrostatically or magnetically [12] whereas their topography, spatial extent and polarization can be precisely inspected by the state-of-art tunneling measurements [15,16].

It has been reported that adatoms deposited on a two-dimensional (2D) superconducting surface develop

Yu–Shiba–Rusinov (YSR) states, extending to a dozen of intersite distances and they reveal particle–hole oscillations [11]. Bound states of these magnetic impurities in superconducting $NbSe_2$ are characterized by the star shape [17] typical for the rotational symmetry of its triangular lattice. More complex objects, such as dimers, reveal other spatial features, showing the bonding and antibonding states [18]. In a somewhat different context it has been pointed out [19] that exchange coupling between numerous quantum defects involving their intrinsic spins can couple them ferromagnetically. This can be used (e.g., in metallic carbon nanotubes) for a robust transmission of magnetic information over large distances.

In all cases the bound YSR states are also sensitive to interactions. One of them is the spin–orbit coupling (usually meaningful at boundaries, e.g., surfaces) [20-22]. Such interaction in one-dimensional magnetic nanowires can induce the topologically nontrivial superconducting phase, in which the YSR states undergo mutation to Majorana (zero-energy) quasiparticles. Coulomb repulsion between the opposite spin electrons can bring additional important effects. In the proximitized quantum dots it can lead to a parity change (quantum phase transition) with further influence on the subgap Kondo effect (driven by effective spin-exchange coupling with mobile electrons). Furthermore, such spin exchange can be amplified by the induced electron pairing, and can have constructive influence on the Kondo effect [23,24].

We study here the polarized bound states, taking into account the spin–orbit and/or Coulomb interactions. In particular, we consider: (i) a single magnetic impurity in a 2D square lattice of a superconducting host, (ii) a nanoscopic chain of magnetic impurities on the classical superconductor (i.e., proximitized Rashba nanowire) in its topologically trivial/nontrivial superconducting phase, and (iii) a strongly correlated quantum dot side-attached to the Rashba chain, where the Kondo and the leaking Majorana quasiparticle can be confronted with each other. These magnetically polarized YSR and Majorana quasiparticles as well as the subgap Kondo effect can be experimentally verified using tunneling heterostructures with ferromagnetic lead (STM tip).

Results and Discussion

Single magnetic impurity

Let us start by considering a single magnetic impurity on the surface of an *s*-wave superconductor in presence of spin–orbit interactions. This situation can be modeled by the Anderson-type Hamiltonian

$$\widehat{\mathcal{H}} = \widehat{\mathcal{H}}_{\rm sc} + \widehat{\mathcal{H}}_{\rm imp} + \widehat{\mathcal{H}}_{\rm SOC}. \qquad (1)$$

We describe the superconducting substrate by

$$\widehat{\mathcal{H}}_{\rm sc} = -t\sum_{\langle i,j\rangle\sigma}\hat{c}^{\dagger}_{i\sigma}\hat{c}_{j\sigma} + U\sum_i \hat{n}_{i\uparrow}\hat{n}_{i\downarrow} - \mu\sum_{i\sigma}\hat{n}_{i\sigma}, \qquad (2)$$

where $\hat{c}^{\dagger}_{i\sigma}$ ($\hat{c}_{i\sigma}$) denotes creation (annihilation) of an electron with spin σ at the *i*-th site, *t* is a hopping integral between the nearest neighbors, μ is the chemical potential, and $\hat{n}_{i\sigma} = \hat{c}^{\dagger}_{i\sigma}\hat{c}_{i\sigma}$ is the number operator. For simplicity, we assume a weak attractive potential $U < 0$ between itinerant electrons and treat it within the mean-field decoupling

$$\hat{c}^{\dagger}_{i\uparrow}\hat{c}_{i\uparrow}\hat{c}^{\dagger}_{i\downarrow}\hat{c}_{i\downarrow} \approx \chi_i\hat{c}^{\dagger}_{i\uparrow}\hat{c}^{\dagger}_{i\downarrow} + \chi^{*}_i\hat{c}_{i\downarrow}\hat{c}_{i\uparrow} - |\chi_i|^2 + n_{i\uparrow}\hat{c}^{\dagger}_{i\downarrow}\hat{c}_{i\downarrow} + n_{i\downarrow}\hat{c}^{\dagger}_{i\uparrow}\hat{c}_{i\uparrow} - n_{i\uparrow}n_{i\downarrow},$$

where $\chi_i = \langle\hat{c}_{i\downarrow}\hat{c}_{i\uparrow}\rangle$ is the local superconducting order parameter and $n_{i\sigma} = \langle\hat{n}_{i\sigma}\rangle$. The Hartree term can be incorporated into the local (spin-dependent) chemical potential $\mu \to \tilde{\mu}_{i\sigma} \equiv \mu - Un_{i\bar{\sigma}}$. The second term in Equation 1 refers to the local impurity

$$\widehat{\mathcal{H}}_{\rm imp} = -J\left(\hat{c}^{\dagger}_{0\uparrow}\hat{c}_{0\uparrow} - \hat{c}^{\dagger}_{0\downarrow}\hat{c}_{0\downarrow}\right) + K\left(\hat{c}^{\dagger}_{0\uparrow}\hat{c}_{0\uparrow} + \hat{c}^{\dagger}_{0\downarrow}\hat{c}_{0\downarrow}\right), \qquad (3)$$

which affects the order parameter χ_i near the impurity site $i = 0$, inducing the YSR states [25,26]. In this work we focus on the magnetic term *J* [4,27], disregarding the potential scattering *K*.

The spin–orbit coupling (SOC) can be expressed by

$$\widehat{\mathcal{H}}_{\rm SOC} = -{\rm i}\lambda\sum_{ij\sigma\sigma'}\hat{c}^{\dagger}_{i+\mathbf{d}_j\sigma}\left(\mathbf{d}_j\times\hat{\boldsymbol{\sigma}}^{\sigma\sigma'}\right)\cdot\widehat{\mathbf{w}}\,\hat{c}_{i\sigma'}, \qquad (4)$$

where the vector $\mathbf{d}_j = (d^x_j, d^y_j, 0)$ refers to positions of the nearest neighbors of the *i*-th site, and $\hat{\boldsymbol{\sigma}} = (\sigma_x, \sigma_y, \sigma_z)$ stands for the Pauli matrices. The unit vector $\widehat{\mathbf{w}}$ shows the direction of the spin–orbit field, which can be arbitrary. Here we restrict our considerations to the in-plane $\widehat{\mathbf{w}} \equiv \hat{x} = (1, 0, 0)$ polarization, which will be important for nontrivial superconductivity in nanowires discussed in the subsection 'Magnetically polarized Majorana quasiparticles'. The other (out-of-plane) component could eventually mix ↑ and ↓ spins [22].

Impurities break the translational invariance, therefore the pairing amplitude χ_i and occupancy $n_{i\sigma}$ have to be determined for each lattice site individually. We can diagonalize the Hamiltonian (Equation 1) by the unitary transformation

$$\hat{c}_{i\sigma} = \sum_n \left(u_{in\sigma}\hat{\gamma}_n - \sigma v^*_{in\sigma}\hat{\gamma}^\dagger_n \right), \quad (5)$$

where $\hat{\gamma}^{(\dagger)}_n$ are quasiparticle fermionic operators with eigenvectors $u_{in\sigma}$ and $v_{in\sigma}$. This leads to the Bogoliubov–de Gennes (BdG) equations

$$\mathcal{E}_n \begin{pmatrix} u_{in\uparrow} \\ v_{in\downarrow} \\ u_{in\downarrow} \\ v_{in\uparrow} \end{pmatrix} = \sum_j \begin{pmatrix} H_{ij\uparrow} & D_{ij} & S^{\uparrow\downarrow}_{ij} & 0 \\ D^*_{ij} & -H^*_{ij\downarrow} & 0 & S^{\downarrow\uparrow}_{ij} \\ S^{\downarrow\uparrow}_{ij} & 0 & H_{ij\downarrow} & D_{ij} \\ 0 & S^{\uparrow\downarrow}_{ij} & D^*_{ij} & -H^*_{ij\uparrow} \end{pmatrix} \begin{pmatrix} u_{jn\uparrow} \\ v_{jn\downarrow} \\ u_{jn\downarrow} \\ v_{jn\uparrow} \end{pmatrix}, \quad (6)$$

where $D_{ij} = \delta_{ij} U \chi_i$, and the single-particle term is given by

$$H_{ij\sigma} = -t\delta_{\langle i,j\rangle} - \left(\tilde{\mu}_{i\sigma} - \sigma J \delta_{i0} \right) \delta_{ij} + S^{\sigma\sigma}_{ij}$$

with the spin–orbit coupling term

$$S^{\sigma\sigma'}_{ij} = -\mathrm{i}\lambda \sum_l \left(\mathbf{d}_l \times \hat{\boldsymbol{\sigma}}^{\sigma\sigma'} \right) \cdot \hat{\mathbf{w}}\, \delta_{j,i+\mathbf{d}_l}.$$

Here, $S^{\sigma\sigma}_{ij}$ and $S^{\sigma\bar{\sigma}}_{ij}$ (where $\bar{\sigma}$ is opposite to σ) correspond to in-plane and out-of-plane spin–orbit field, respectively, and satisfy $S^{\sigma\sigma'}_{ij} = (S^{\sigma'\sigma}_{ji})*$.

Solving numerically the BdG equations (Equation 6) we can determine the local order parameter χ_i and occupancy $n_{i\sigma}$

$$\chi_i = \sum_n \left[u_{in\downarrow} v^*_{in\uparrow} f\left(\mathcal{E}_n\right) - u_{in\uparrow} v^*_{in\downarrow} f\left(-\mathcal{E}_n\right) \right], \quad (7)$$

$$n_{i\sigma} = \sum_n \left[\left|u_{in\sigma}\right|^2 f\left(\mathcal{E}_n\right) + \left|v_{in\bar{\sigma}}\right|^2 f\left(-\mathcal{E}_n\right) \right], \quad (8)$$

where $f(\omega) = [1 + \exp(\omega/k_B T)]^{-1}$. In what follows, we shall inspect the spin-resolved local density of states

$$\rho_{i\sigma}(\omega) = \sum_n \left[\left|u_{in\sigma}\right|^2 \delta\left(\omega - \mathcal{E}_n\right) + \left|v_{in\sigma}\right|^2 \delta\left(\omega + \mathcal{E}_n\right) \right].$$

For its numerical computation we replace the Dirac delta function with the Lorentzian function $\delta(\omega) = \zeta/[\pi(\omega^2 + \zeta^2)]$ with a small broadening $\zeta = 0.01$ t. We have solved the BdG equations, considering a single magnetic impurity in a square lattice, comprising $N_a \times N_b = 41 \times 41$ sites. We assumed $U/t = -3$, $\mu/t = 0$, and determined the bound states for two representative values of the spin–orbit coupling λ upon varying J.

The magnetic potential has substantial influence on the local order parameter χ_0. In particular, at some critical value J_c this quantity discontinuously changes its magnitude and sign (see the upper panel in Figure 1), signaling a first-order phase transition [28-30]. This quantum phase transition at J_c is an artifact of the classical spin approximation. When spin fluctuations are allowed, a Kondo-like crossover is obtained instead of a first-order phase transition [31,32]. In general, the quasiparticle spectrum at the impurity site is characterized by two bound states $\pm E_{\mathrm{YSR}}$ inside the gap Δ of the superconducting host (displayed in the bottom panel of Figure 1). These energies $\pm E_{\mathrm{YSR}}$ and the related spectral weights depend on J. At $J = J_c$ the YSR bound states cross each other $E_{\mathrm{YSR}}(J_c) = 0$ and their crossing signifies the ground-state parity change [33] from BCS-type (spinless) to the singly occupied (spinful) configurations [8,15,21,34]. Let us remark that this quantum phase transition is also accompanied with a reversal of the YSR polarization (see bottom panel in Figure 1). A similar behavior can be observed also for multiple impurities, at several critical values of J [35].

Within the BdG approach we can inspect spatial profiles of the YSR states by integrating the spectral weights

$$\rho^{\pm}_{i\sigma} = \int_{\omega_1}^{\omega_2} \rho_{i\sigma}(\omega) \mathrm{d}\omega$$

in the interval $\omega \in (\omega_1, \omega_2)$ capturing the quasiparticles at negative/positive energies $\pm E_{\mathrm{YSR}}$ [36]. Figure 2 illustrates the results obtained for $\lambda = 0$ (left panel) and $\lambda = t$ (right panel). We clearly notice a fourfold rotational symmetry (typical for the square lattice) and the spatial extent of YSR states reaching several sites away from the magnetic impurity. The non-vanishing difference of the spectral weight $|u_{in\uparrow}|^2 - |u_{in\downarrow}|^2$ at the positive energy $\omega = +E_{YSR}$ and of $|v_{in\uparrow}|^2 - |v_{in\downarrow}|^2$ at the negative energy $\omega = -E_{YSR}$ implies the effective spin-polarization of the bound states (their polarization is illustrated in the bottom panel of Figure 1).

For a quantitative estimation of the spatially varying magnetization (driven by the particle–hole asymmetry) we have computed the displaced moving average $\overline{\rho}^{\pm}(r)$, which corresponds to an averaged spectral weight contained in a ring of the radius r and a small half-width δr. This quantity is sensitive only to the radial distance r from the magnetic impurity, averaging the angular anisotropy. Our results, presented in Figure 3, clearly indicate the spatial particle–hole oscillations $\overline{\rho}^{\pm}(r)$ of the YSR states (compare the blue and red lines). Such particle–hole oscillations decay exponentially with r in agreement with previous studies [11,37,38]. The dominant (particle or hole) contributions to the YSR bound states are displayed by the

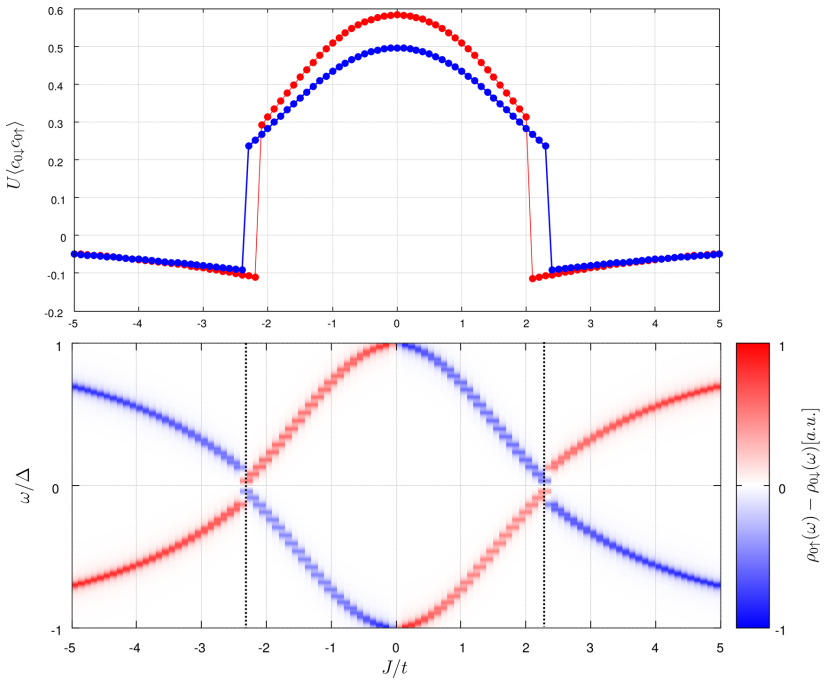

Figure 1: The local order parameter obtained at zero temperature for weak $\lambda/t = 0.1$ (red line) and strong spin–orbit coupling $\lambda/t = 1$ (blue line). The bottom panel shows the energies and magnetic polarization $\rho_{0\uparrow}(\omega) - \rho_{0\downarrow}(\omega)$ of YSR states obtained in the weak-coupling limit $\lambda/t = 0.1$.

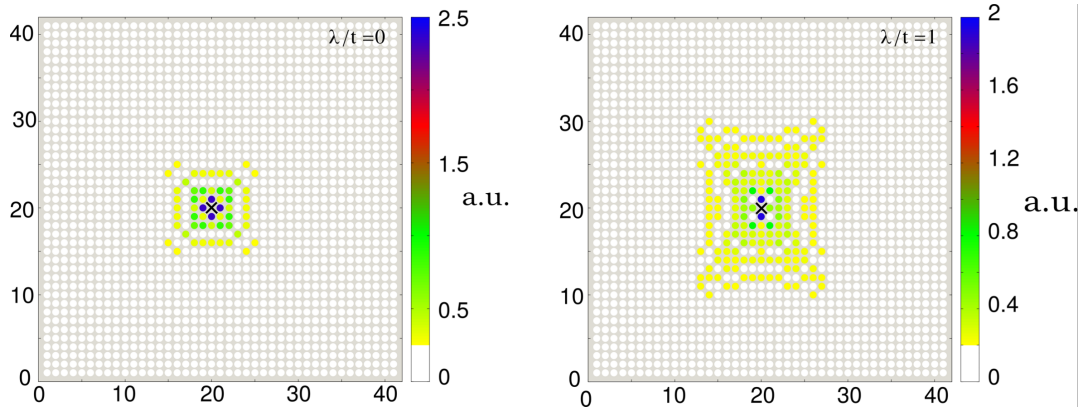

Figure 2: Spatial profiles of the YSR states $\sum_\sigma \rho^+_{i\sigma}$ obtained for $|J| < J_c$ in the absence of spin–orbit coupling (left panel) and for strong in-plane coupling $\lambda = t$ (right panel). The spin–orbit field is chosen along the *x*-axis and leads to an additional imaginary hopping term along the *y*-axis, which elongates the YSR states in the *y*-direction. The impurity spin is oriented along the (0, 0, 1) direction.

alternating color of the background in Figure 3. We notice that the spin–orbit coupling seems to suppress these particle–hole oscillations.

Summarizing this section, we point out that the quantum phase transition at J_c depends on the spin–orbit coupling λ and it has experimentally observable consequences in the magnetization induced near the impurity site. For weak magnetic scattering $|J| < J_c$ the impurity is partly screened, whereas for stronger couplings $|J| > J_c$ the impurity polarizes its neighborhood in the direction of its own magnetic moment. Similar effects have been previously discussed in [21], but here we additionally consider the role of spin–orbit coupling. First of all, such interaction shifts the quantum phase transition (to larger values of *J*) and secondly it enhances the spatial extent of YSR states and gradually smoothes the particle–hole oscillations.

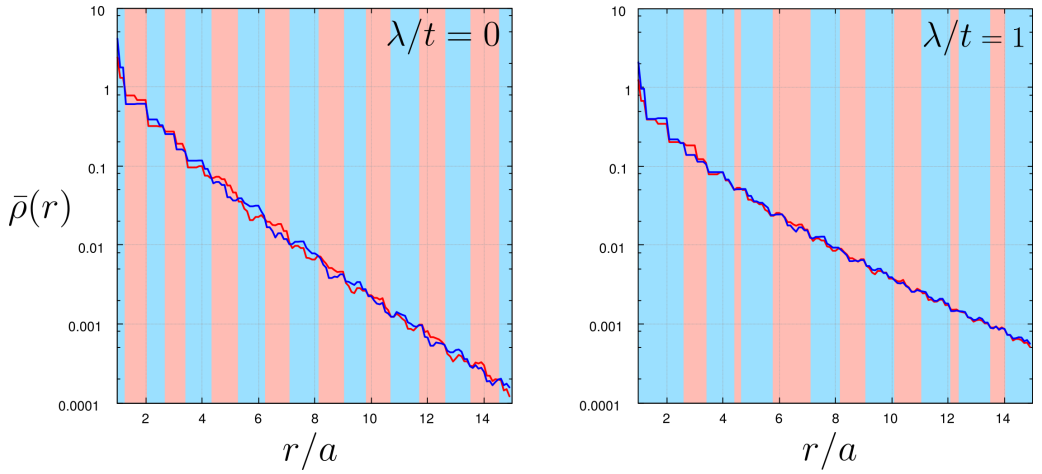

Figure 3: Hole-like (blue line) and electron-like (red line) displaced moving average $\bar{\rho}^{\pm}(r)$ as a function of the radial distance r from the impurity site obtained for $|J| < J_c$ using $\delta r = 0.5a$. The blue and red background color indicates the dominant type (hole or particle) of the YSR states at a given distance r. The left and right panels correspond to $\lambda = 0$ and $\lambda = t$, respectively.

Magnetically polarized Majorana quasiparticles

In this section we increase the number of impurities. Let us now imagine a nanoscopic chain of magnetic impurities (for instance Fe atoms) deposited on the surface of a conventional *s*-wave superconductor. We study the magnetically polarized bound states, focusing on the proximity-induced nontrivial superconducting phase. In practice, the quasiparticle spectrum can be probed within STM-type setups, by attaching a conducting [39,40], superconducting [41], or a magnetically polarized tip [42]. We assume the spin–orbit interaction aligned perpendicularly to the wire and the magnetic field parallel to it, leading to the effective intersite pairing of identical spins and (under specific conditions) inducing zero-energy end modes resembling Majorana quasiparticles. This issue has been recently studied very intensively but here we simply focus on the spin-polarized aspects of this problem.

Due to the spin–orbit interaction, momentum and spin are no longer "good" quantum numbers. By solving the problem numerically, however, we can estimate the percentage with which the true quasiparticles are represented by the initial spin. We have recently emphasized [43], that the amplitude of intersite pairing (between identical spin electrons) differs several times for ↑ and ↓ sectors. This leads to an obvious polarization of the YSR and Majorana quasiparticles (the latter appearing near the nanochain edges).

Let us consider the STM-type geometry relevant to the recent experimental situation addressed by A. Yazdani and co-workers [42], which can be described by the following Hamiltonian

$$\widehat{\mathcal{H}} = \widehat{\mathcal{H}}_{\text{tip}} + \widehat{\mathcal{H}}^{\text{prox}}_{\text{chain}} + \widehat{\mathcal{H}}_{\text{tip-chain}}. \tag{9}$$

We assume here that the STM tip describes a polarized fermion gas

$$\widehat{\mathcal{H}}_{\text{N}} = \sum_{\mathbf{k},\sigma} \xi^{\sigma}_{\mathbf{k}\text{N}} \hat{c}^{\dagger}_{\mathbf{k}\sigma\text{N}} \hat{c}_{\mathbf{k}\sigma\text{N}}$$

where the energy $\xi^{\sigma}_{\mathbf{k}\text{N}} = \varepsilon_{\mathbf{k}} - \mu_{\text{N}\sigma}$ can be controlled by some finite detuning of the chemical potentials $\mu_{\text{N}\uparrow} - \mu_{\text{N}\downarrow}$. Individual atoms of the nanochain are coupled with such STM tip through

$$\widehat{\mathcal{H}}_{\text{tip-chain}} = \sum_{\mathbf{k},\sigma} \left(V_{i,\mathbf{k}\text{N}}\ \hat{d}^{\dagger}_{i,\sigma} \hat{c}_{\mathbf{k}\sigma\text{N}} + V^{*}_{i,\mathbf{k}\beta} \hat{c}^{\dagger}_{\mathbf{k}\sigma\text{N}} \hat{d}_{i,\sigma} \right).$$

For simplicity, we assume constant couplings

$$\Gamma_{\beta} = 2\pi \sum_{\mathbf{k}} \left| V_{i,\mathbf{k}\beta} \right|^2\ \delta\left(\omega - \xi_{\mathbf{k}\beta}\right).$$

The low-energy physics of such proximitized Rashba nanowire can be described by [44]

$$\widehat{\mathcal{H}}^{\text{prox}}_{\text{chain}} = \sum_{i,j,\sigma} \left(t_{ij} - \delta_{ij}\mu\right) \hat{d}^{\dagger}_{i,\sigma} \hat{d}_{j,\sigma} + \widehat{\mathcal{H}}_{\text{Rashba}} + \widehat{\mathcal{H}}_{\text{Zeeman}} + \widehat{\mathcal{H}}_{\text{prox}}, \tag{10}$$

where $\hat{d}^{(\dagger)}_{i,\sigma}$ annihilates (creates) an electron of spin σ at site i with energy ε_i, and t_{ij} is the hopping integral. The effective intersite (*p*-wave) pairing is induced through a combined effect of the Rashba and the Zeeman terms

$$\widehat{\mathcal{H}}_{\text{Rashba}} = -\alpha \sum_{i,\sigma,\sigma'} \left[\hat{d}^{\dagger}_{i+1,\sigma} \left(i\sigma^{y} \right)_{\sigma\sigma'} \hat{d}_{i,\sigma'} + \text{H.c.} \right], \quad (11)$$

$$\widehat{\mathcal{H}}_{\text{Zeeman}} = \frac{g\mu_{\text{B}}B}{2} \sum_{i,\sigma,\sigma'} \hat{d}^{\dagger}_{i,\sigma} \left(\sigma^{z} \right)_{\sigma\sigma'} \hat{d}_{i,\sigma'}. \quad (12)$$

The proximity effect, which induces the on-site (trivial) pairing, can be modelled as [45]

$$\widehat{\mathcal{H}}_{\text{prox}} = \Delta_i \left(\hat{d}^{\dagger}_{i,\uparrow} \hat{d}^{\dagger}_{i,\downarrow} + \hat{d}_{i,\downarrow} \hat{d}_{i,\uparrow} \right) \quad (13)$$

with the local pairing potential $\Delta_i = \Gamma_S/2$.

Figure 4 shows evolution of the spin-dependent spectrum $\rho_{i\sigma}(\omega)$ as a function of a varying magnetic field. At a critical value ($B \approx 0.2$) we observe the emergence of zero-energy quasiparticles, whose spectral weights strongly depend on the spin σ.

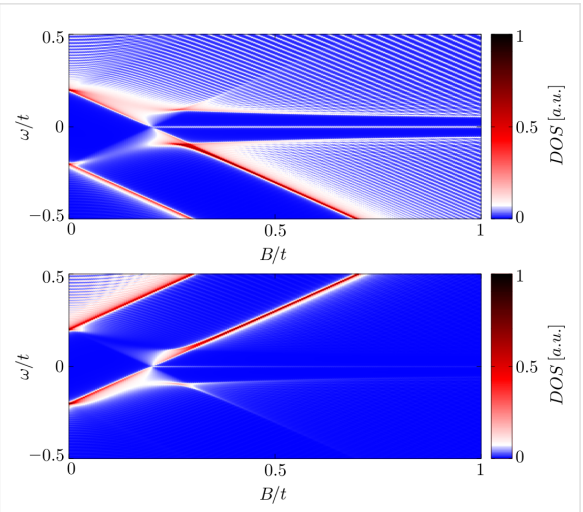

Figure 4: The effective quasiparticle spectrum $\rho_{i\sigma}(\omega)$ as a function of a magnetic field B aligned along the nanochain obtained for σ = ↑ (upper panel) and σ = ↓ (bottom panel). The magnetic field B is expressed in units of $t/(g\mu_B/2)$.

For a better understanding of the polarized zero-energy quasiparticles, we present in Figure 5 the spatial profiles of the zero-energy (Majorana) quasiparticles. As usually such quasiparticles emerge near the edges of a nanoscopic chain, practically over 10 to 15 sites (see inset). Note the substantial quantitative difference between these zero-energy quasiparticles appearing in ↑ and ↓ spin sectors. This "intrinsic polarization" of the Majorana modes has been previously suggested in [46], and recently we have proposed [47] their empirical detection by means of selective equal-spin Andreev reflection (SESAR) spectroscopy.

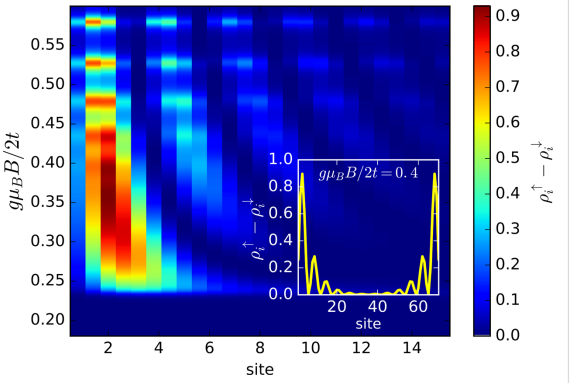

Figure 5: Magnetically polarized spectrum $\rho_{i,\uparrow}(\omega) - \rho_{i,\downarrow}(\omega)$ obtained at ω = 0 for peripheral sites of the Rashba chain.

The main idea is to apply a bias voltage V between the STM tip and the superconducting substrate, inducing a charge transport that, in a subgap regime ($|V| \ll \Delta/|e|$) originates from the Andreev (particle to hole) scattering mechanism. The polarized Andreev current can be expressed by the Landauer–Büttiker formula

$$I_i^{\sigma}(V) = \frac{e}{h} \int \mathrm{d}\omega \, T_i^{\sigma}(\omega) \left[f(\omega - eV) - f(\omega + eV) \right], \quad (14)$$

where transmittance is defined as

$$T_i^{\sigma}(\omega) = \Gamma_{\text{N}}^2 \left| \langle\langle \hat{d}_{i\sigma} \hat{d}_{i+1\sigma} \rangle\rangle \right|^2 + \Gamma_{\text{N}}^2 \left| \langle\langle \hat{d}_{i\sigma} \hat{d}_{i-1\sigma} \rangle\rangle \right|^2$$

and

$$T_1^{\sigma}(\omega) = \Gamma_{\text{N}}^2 \left| \langle\langle \hat{d}_{1\sigma} \hat{d}_{2\sigma} \rangle\rangle \right|^2,$$

$$T_{\text{N}}^{\sigma}(\omega) = \Gamma_{\text{N}}^2 \left| \langle\langle \hat{d}_{N\sigma} \hat{d}_{N-1\sigma} \rangle\rangle \right|^2.$$

The anomalous Green's functions can be computed numerically from the solution of the Bogoliubov–de Gennes equations of this model (Equation 10). The net spin current $I_i^{\text{spin}}(V) = I_i^{\uparrow}(V) - I_i^{\downarrow}(V)$ turns out to be predominantly sensitive to the Majorana end-modes. Its differential conductance $G_i^{\text{spin}}(V) = (\partial / \partial V) I_i^{\text{spin}}(V)$ can thus distinguish the polarized Majorana quasiparticle (near $V = 0$) from the YSR states (appearing at finite voltage).

Bound states can leak to other side-attached nanoscopic objects. This proximity effect has been also predicted for the Majorana quasiparticles by E. Vernek et al. [48] and it has been indeed observed experimentally by M. T. Deng and co-authors [49]. Inspired by this achievement, extensive studies have been carried out regarding the YSR states coalescencing into the zero-energy Majorana states in side-coupled quantum dots driven by electrostatic or magnetic fields [50-52]. This issue would be particularly important when attempting to braid the Majorana end modes, e.g., in T-shape nanowires upon turning on and off the topological superconducting phase in its segments. We briefly analyse here the polarized zero-energy Majorana modes leaking into the multi-site quantum dot (comprising ten lattice sites) side-attached to the proximitized Rashba chain discussed above.

Figure 6 displays the spatial profile of the polarized spectrum obtained at $\omega = 0$ as a function of the gate voltage V_g, which detunes the energies $V_g = \varepsilon_i - \mu$ of the multi-site ($1 \le i \le 10$) quantum dot. For numerical calculations we used the model parameters $\lambda = 0.15t$, $\mu = -2t$, $\Delta_i = 0.2t$ and $B > B_c$, which guarantee the Rashba chain to be in its topologically nontrivial superconducting phase, hosting the zero-energy Majorana quasiparticles (intensive black or red regions). We clearly observe that for some values of V_g these Majorana modes spread over the entire quantum dot region. By inspecting Figure 6 we furthermore notice the pronounced spatial oscillations of these zero-energy modes. In our opinion, this is a signature of a partial delocalization of the polarized Majorana quasiparticles. Surprisingly, this process seems to be less efficient in the minor spin ($\sigma = \downarrow$) section. This effect has to be taken into account, when designing nanostructures for a controllable spatial displacement of the Majorana modes (criticial for the realization of quantum computations with use of the Majorana-based qubits) either by electrostatic or magnetic means. Some proposals for such nanodevices have been recently discussed by several authors [52,53].

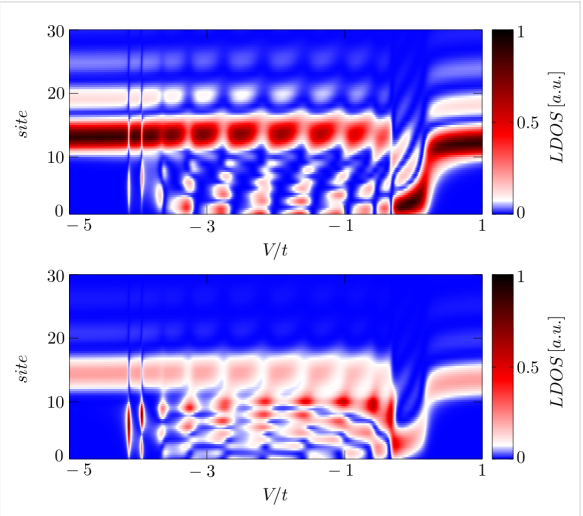

Figure 6: Leakage of the spin-polarized Majorana quasiparticles from the topological superconducting phase of the Rashba chain ($i \ge 10$) onto the side-attached multi-site ($i \in \langle 1;10 \rangle$) quantum dot. The upper and bottom panel show $\rho_{i\sigma}(\omega)$ at $\omega = 0$ for ↑ and ↓ spin, respectively.

In summary of this section, we emphasize that the Majorana modes coalescing from the YSR states in the proximitized Rashba nanowire are characterized by their magnetic polarization. Indeed, such a feature has been recently observed by STM spectroscopy with use of a polarized tip [42]. We have studied here the evolution of the polarized quasiparticle states with respect to the magnetic field (Figure 4) and investigated the spatial oscillations of the Majorana zero-energy modes near the chain edges (Figure 5). Finally, we analyzed leakage of the polarized Majorana modes on the multi-site quantum dots, revealing their partial delocalization (Figure 6).

Majorana vs Kondo effect

In previous section we have discussed the polarized Majorana modes leaking into side-attached objects, such as single impurities or segments of normal nanowires. In this section we shall focus on the correlation effects [54-56], confronting the Majorana quasiparticle with the Kondo effect (both manifested at zero energy). This can be practically achieved using STM-type configurations sketched in Figure 7. In particular, we consider the subgap Kondo effect, effectively driven by the Coulomb repulsion U and coupling of the quantum dot (QD) with the normal lead Γ_N in presence of electron pairing (induced via Γ_S), which has a significant influence on the spin-polarized bound states of the QD. The basic mechanism of this subgap Kondo effect showing up near the quantum phase transition has been earlier considered by us in absence of the Rashba nanowire

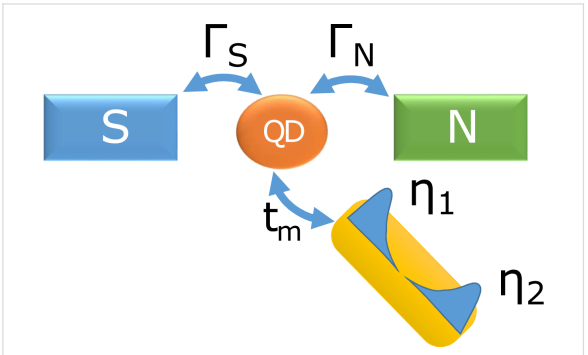

Figure 7: Schematic illustration of the quantum dot (QD) coupled between the metallic (N) and superconducting (S) leads and hybridized with the Rashba nanowire, hosting the Majorana quasiparticles η_1 and η_2 at its edges.

[24,57]. Our considerations can be practically verified within STM geometry [39,40] using magnetic atoms (e.g., Fe) and side-coupled nonmagnetic atoms (for instance Ag or Au) deposited on the superconducting substrate (such as Pb or Al) probed with a conducting STM tip [42].

The topological superconducting phase, hosting the Majorana modes, can be driven in semiconducting wires [58,59] or in nanochains of magnetic atoms [39-42] through nearest-neighbor equal-spin pairing. The efficiency of such *p*-wave pairing differs for each spin [47], giving rise to polarization of the Majorana quasiparticles, with noticeable preference for the ↑ sector (see Figure 4). In order to study the correlation effects we shall assume here a complete polarization of the Majorana quasiparticles. We thus focus, for simplicity, on the topological state originating from intersite pairing of only ↑ electrons and consider its interplay with the correlations. Let us remark, however, that the superconducting lead mixes both the QD spins with the side-attached Majorana quasiparticle [60]. In consequence we shall observe an interesting and spin-dependent relationship between the Majorana and Kondo states that could be probed by the polarized Andreev (particle-to-hole conversion) mechanism.

Our setup (Figure 7) can be described by the following Anderson-type Hamiltonian

$$\widehat{\mathcal{H}} = \sum_{\beta=S,N} \left(\widehat{\mathcal{H}}_{\beta} + \widehat{\mathcal{H}}_{\beta-QD}\right) + \widehat{\mathcal{H}}_{QD} + \widehat{\mathcal{H}}_{MQD}, \qquad (15)$$

where $\widehat{\mathcal{H}}_N$ corresponds to the metallic electrode, $\widehat{\mathcal{H}}_S$ refers to the *s*-wave superconducting substrate and the correlated QD is modeled by $\widehat{\mathcal{H}}_{QD} = \sum_\sigma \varepsilon \hat{d}_\sigma^\dagger \hat{d}_\sigma + U\hat{n}_\downarrow \hat{n}_\uparrow$, where ε denotes the energy level and *U* stands for the repulsive interaction between opposite spin electrons. The QD is coupled to both β = N,S reservoirs through $\widehat{\mathcal{H}}_{\beta-QD} = \sum_{\mathbf{k},\sigma} (V_{\mathbf{k}\beta} \hat{d}_\sigma^\dagger \hat{c}_{\mathbf{k}\sigma\beta} + \text{H.c.})$ and we assume a wide bandwidth limit, using the constant couplings Γ_β. It can be shown [61-64] that for energies $|\omega| \ll \Delta$ the superconducting electrode induces the static on-dot pairing

$$\widehat{\mathcal{H}}_S + \widehat{\mathcal{H}}_{S\text{-}QD} \approx \mathcal{H}_{prox} = \sum_\sigma \varepsilon \hat{d}_\sigma^\dagger \hat{d}_\sigma + U\hat{n}_\downarrow \hat{n}_\uparrow - \frac{\Gamma_S}{2}\left(\hat{d}_\uparrow \hat{d}_\downarrow + \hat{d}_\downarrow^\dagger \hat{d}_\uparrow^\dagger\right).$$

Taking into account the finite magnitude of superconducting gap [50] does not affect the main conclusions of our study.

The effective Majorana modes of the nanowire can be modeled by [65]

$$\widehat{\mathcal{H}}_{MQD} = i\varepsilon_m \hat{\eta}_1 \hat{\eta}_2 + \lambda\left(\hat{d}_\uparrow \hat{\eta}_1 + \hat{\eta}_1 \hat{d}_\uparrow^\dagger\right),$$

where $\hat{\eta}_i = \hat{\eta}_i^\dagger$ are Hermitian operators and ε_m corresponds to an overlap between Majoranas. We recast these operators by the standard fermionic ones [66] $\hat{\eta}_1 = (1/\sqrt{2})(\hat{f} + \hat{f}^\dagger)$ and $\hat{\eta}_2 = (-i/\sqrt{2})(\hat{f} - \hat{f}^\dagger)$. Finally, the Hamiltonian of Equation 15 simplifies to

$$\widehat{\mathcal{H}} = \widehat{\mathcal{H}}_N + \widehat{\mathcal{H}}_{N\text{-}QD} + \sum_\sigma \varepsilon \hat{d}_\sigma^\dagger \hat{d}_\sigma + U\hat{n}_\downarrow \hat{n}_\uparrow - \frac{\Gamma_S}{2}\left(\hat{d}_\uparrow \hat{d}_\downarrow + \hat{d}_\downarrow^\dagger \hat{d}_\uparrow^\dagger\right) + \varepsilon_m \hat{f}^\dagger \hat{f} + t_m\left(\hat{d}_\uparrow^\dagger - \hat{d}_\uparrow\right)\left(\hat{f} + \hat{f}^\dagger\right) - \frac{\varepsilon_m}{2}, \qquad (16)$$

with the auxiliary coupling $t_m = \lambda/\sqrt{2}$. The subgap Kondo physics originates in this model from the Coulomb term $U\hat{n}_\downarrow \hat{n}_\uparrow$ and the effective spin-exchange interactions due to $\widehat{\mathcal{H}}_{N\text{-}QD}$. It has been shown [23,24] that under specific conditions the on-dot pairing can cooperate with the subgap Kondo effect. This particular situation occurs only near the quantum phase transition.

Let us examine how the subgap Kondo effect gets along with the Majorana mode. Earlier studies of the correlated quantum dot coupled to both normal (conducting) electrodes indicated that the side-attached Rashba chain leads to a competition between the Kondo and Majorana states [67-72]. For a sufficiently long wire ($\varepsilon_m = 0$) the Kondo effect persists only in the spin-channel ↓, whereas for ↑ electrons there appears a dip in the spectral density at ω = 0. The resulting tunneling conductance is then partly reduced (from the perfect value $2e^2/h$) to the fractional value $3e^2/2h$ [67,68,71-73]. In contrast, for the short Rashba wires (with $\varepsilon_m \neq 0$) the Kondo physics persists in both spin channels.

In our present setup (Figure 7) the correlated quantum dot is between the metallic and superconducting reservoirs, therefore the Kondo effect is additionally affected by on-dot pairing. Its influence is mainly controlled by the ratio U/Γ_S and partly by the level ε, determining whether the QD ground state is in the spinful or spinless configuration [23,24,62,64,74]. Obviously the latter one cannot be screened. For instance, for the half-filled QD ($\varepsilon = -U/2$) the spinful (doublet) configuration occurs in the regime $U \geq \Gamma_S$.

For studying the correlations we adopt perturbative treatment of the Coulomb potential, treating it self-consistently to the second order in the normal and anomalous channels [62,75]. Specific expressions have been provided by us in [24]. Figure 8 shows the spectral function $\rho_\sigma(\omega)$ for both spins obtained at zero temperature for the Coulomb potential *U*, covering the (spinless)

singlet and (spinful) doublet configurations. In the weak interaction regime we observe appearance of two YSR states. For $U \approx \Gamma_S$ these peaks merge, signaling the quantum phase transition. The Kondo effect shows up only in the correlated limit ($U > \Gamma_S$), but its spectroscopic signatures are qualitatively different for each of the spins. Leakage of the Majorana quasiparticle suppresses the low-energy states of ↑ electrons. We notice that the initial density (for $t_m = 0$) is reduced by half, whereas we observe a constructive influence of the Majorana quasiparticle on opposite-spin ↓ electrons.

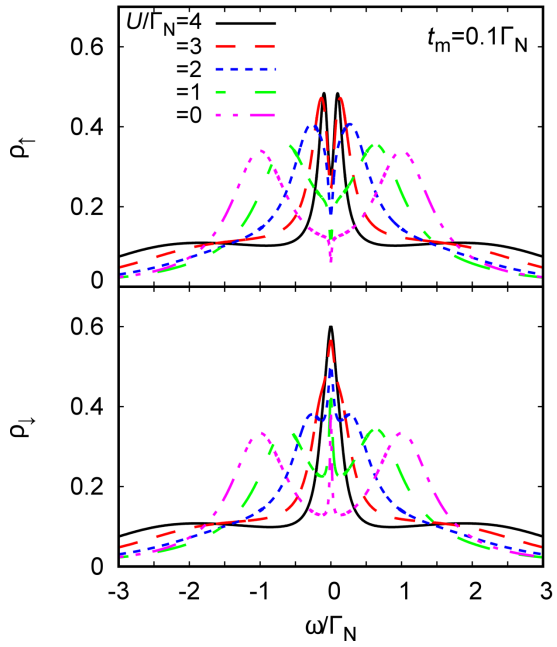

Figure 8: The polarized spectral function $\rho_\sigma(\omega)$ obtained at zero temperature for the half-filled QD ($\varepsilon = -U/2$), $\Gamma_S = 2\Gamma_N$, $t_m = 0.1\Gamma_N$ and several values of the Coulomb potential U (as indicated). Energies are expressed in units of Γ_N.

Figure 9 shows evolution of the spectral function $\rho_\uparrow(\omega)$ for various couplings t_m. In the weak-coupling limit we clearly observe a reduction (by half) of the initial density of states. With increasing t_m the spectrum develops the three-peak structure that is typical for the "molecular" limit. This behavior indicates that the Majorana and Kondo states have rather a complicated relation, which is neither competitive nor cooperative. In fact, some novel scaling laws have been recently reported by several authors [69,70,76-79] also considering the correlation effects directly in the Rashba nanowire.

Conclusion

We have studied the polarized bound states of magnetic impurities embedded in an *s*-wave superconducting material, taking

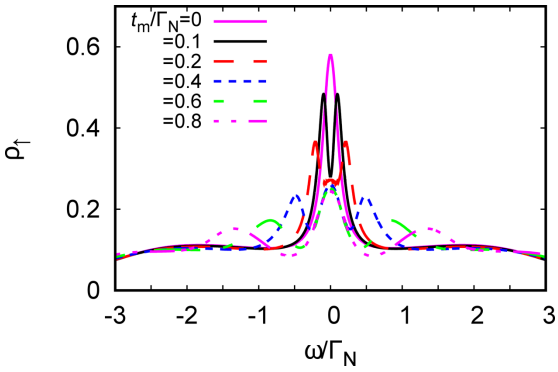

Figure 9: The spectral function $\rho_\uparrow(\omega)$ of the half-filled quantum dot ($\varepsilon = -U/2$) obtained at $T = 0$ for $\Gamma_S/\Gamma_N = 2$, $U/\Gamma_N = 4$ and several values of t_m (as indicated).

into account the spin–orbit and/or Coulomb interactions. We have shown that spin–orbit coupling strongly affects the subgap states, both of the single impurities and their conglomerate arranged into a nanoscopic chain. For the case of single magnetic impurity the spin–orbit interaction (i) shifts the quantum phase transition towards higher magnetic coupling J_c, (ii) enhances the spatial size of the YSR states, and (iii) smoothes the particle–hole oscillations. For the magnetic chain spin–orbit coupling combined with the Zeeman term induce the topologically nontrivial superconducting state and indirectly give rise to substantial polarization of the Majorana modes (Figure 4), the oscillations of which show up near the chain edges (Figure 5). The polarized Majorana quasiparticles can also leak into other side-coupled objects, such as single or multiple quantum impurities (Figure 6). These polarized Majorana quasiparticles can be controlled by a magnetic field or by an electrostatic potential. This would be important for future quantum computers using qubits based on topologically protected Majorana states. Finally, we have also confronted the Majorana quasiparticles with the subgap Kondo effect, revealing their complex relationship that can be hardly regarded as competitive or collaborative in some analogy to the Kondo effect originating from multiple degrees of freedom [80]. The aforementioned spin-polarized effects can be experimentally verified by polarized ballistic tunneling or by using STM spectroscopy, relying on the selective equal-spin Andreev reflections.

Acknowledgements

We thank for instructive remarks from R. Aguado, J. Klinovaja, R. Lutchyn, P. Simon, and R. Žitko on different parts of our study. This work was supported by the National Science Centre (Poland) under grants DEC-2014/13/B/ST3/04451 (AK, SG, TD) and DEC-2013/11/B/ST3/00824 (MMM) UMO-2017/25/

B/ST3/02586 (AP) and by the Faculty of Mathematics and Natural Sciences of the University of Rzeszów through the project WMP/GD-06/2017 (GG).

ORCID® iDs

Andrzej Ptok - https://orcid.org/0000-0002-5566-2656
Maciej M. Maśka - https://orcid.org/0000-0003-2214-3283

References

1. Choi, S.; Choi, H. J.; Ok, J. M.; Lee, Y.; Jang, W.-J.; Lee, A. T.; Kuk, Y.; Lee, S.; Heinrich, A. J.; Cheong, S.-W.; Bang, Y.; Johnston, S.; Kim, J. S.; Lee, J. *Phys. Rev. Lett.* **2017,** *119,* 227001. doi:10.1103/PhysRevLett.119.227001
2. Kenzelmann, M.; Strässle, T.; Niedermayer, C.; Sigrist, M.; Padmanabhan, B.; Zolliker, M.; Bianchi, A. D.; Movshovich, R.; Bauer, E. D.; Sarrao, J. L.; Thompson, J. D. *Science* **2008,** *321,* 1652. doi:10.1126/science.1161818
3. Meul, H. W.; Rossel, C.; Decroux, M.; Fischer, Ø.; Remenyi, G.; Briggs, A. *Phys. Rev. Lett.* **1984,** *53,* 497. doi:10.1103/PhysRevLett.53.497
4. Balatsky, A. V.; Vekhter, I.; Zhu, J.-X. *Rev. Mod. Phys.* **2006,** *78,* 373. doi:10.1103/RevModPhys.78.373
5. Heinrich, B. W.; Pascual, J. I.; Franke, K. J. *Prog. Surf. Sci.* **2018,** *93,* 1. doi:10.1016/j.progsurf.2018.01.001
6. Yazdani, A.; Jones, B. A.; Lutz, C. P.; Crommie, M. F.; Eigler, D. M. *Science* **1997,** *275,* 1767. doi:10.1126/science.275.5307.1767
7. Ji, S.-H.; Zhang, T.; Fu, Y.-S.; Chen, X.; Ma, X.-C.; Li, J.; Duan, W.-H.; Jia, J.-F.; Xue, Q.-K. *Phys. Rev. Lett.* **2008,** *100,* 226801. doi:10.1103/PhysRevLett.100.226801
8. Franke, K. J.; Schulze, G.; Pascual, J. I. *Science* **2011,** *332,* 940. doi:10.1126/science.1202204
9. Ruby, M.; Pientka, F.; Peng, Y.; von Oppen, F.; Heinrich, B. W.; Franke, K. J. *Phys. Rev. Lett.* **2015,** *115,* 087001. doi:10.1103/PhysRevLett.115.087001
10. Hatter, N.; Heinrich, B. W.; Ruby, M.; Pascual, J. I.; Franke, K. J. *Nat. Commun.* **2015,** *6,* 8988. doi:10.1038/ncomms9988
11. Ménard, G. C.; Guissart, S.; Brun, C.; Pons, S.; Stolyarov, V. S.; Debontridder, F.; Leclerc, M. V.; Janod, E.; Cario, L.; Roditchev, D.; Simon, P.; Cren, T. *Nat. Phys.* **2015,** *11,* 1013. doi:10.1038/nphys3508
12. Jellinggaard, A.; Grove-Rasmussen, K.; Madsen, M. H.; Nygård, J. *Phys. Rev. B* **2016,** *94,* 064520. doi:10.1103/PhysRevB.94.064520
13. Choi, D.-J.; Rubio-Verdú, C.; de Bruijckere, J.; Ugeda, M. M.; Lorente, N.; Pascual, J. I. *Nat. Commun.* **2017,** *8,* 15175. doi:10.1038/ncomms15175
14. Assouline, A.; Feuillet-Palma, C.; Zimmers, A.; Aubin, H.; Aprili, M.; Harmand, J.-C. *Phys. Rev. Lett.* **2017,** *119,* 097701. doi:10.1103/PhysRevLett.119.097701
15. Salkola, M. I.; Balatsky, A. V.; Schrieffer, J. R. *Phys. Rev. B* **1997,** *55,* 12648. doi:10.1103/PhysRevB.55.12648
16. Flatté, M. E.; Byers, J. M. *Phys. Rev. Lett.* **1997,** *78,* 3761. doi:10.1103/PhysRevLett.78.3761
17. Ugeda, M. M.; Bradley, A. J.; Zhang, Y.; Onishi, S.; Chen, Y.; Ruan, W.; Ojeda-Aristizabal, C.; Ryu, H.; Edmonds, M. T.; Tsai, H.-Z.; Riss, A.; Mo, S.-K.; Lee, D.; Zettl, A.; Hussain, Z.; Shen, Z.-X.; Crommie, M. F. *Nat. Phys.* **2016,** *12,* 92. doi:10.1038/nphys3527
18. Kezilebieke, S.; Dvorak, M.; Ojanen, T.; Liljeroth, P. *Nano Lett.* **2018,** *18,* 2311. doi:10.1021/acs.nanolett.7b05050
19. Santos, H.; Soriano, D.; Palacios, J. J. *Phys. Rev. B* **2014,** *89,* 195416. doi:10.1103/PhysRevB.89.195416
20. Kim, Y.; Zhang, J.; Rossi, E.; Lutchyn, R. M. *Phys. Rev. Lett.* **2015,** *114,* 236804. doi:10.1103/PhysRevLett.114.236804
21. Kaladzhyan, V.; Bena, C.; Simon, P. *Phys. Rev. B* **2016,** *93,* 214514. doi:10.1103/PhysRevB.93.214514
22. Ptok, A.; Głodzik, S.; Domański, T. *Phys. Rev. B* **2017,** *96,* 184425. doi:10.1103/PhysRevB.96.184425
23. Žitko, R.; Lim, J. S.; López, R.; Aguado, R. *Phys. Rev. B* **2015,** *91,* 045441. doi:10.1103/PhysRevB.91.045441
24. Domański, T.; Weymann, I.; Barańska, M.; Górski, G. *Sci. Rep.* **2016,** *6,* 23336. doi:10.1038/srep23336
25. Smith, E. D. B.; Tanaka, K.; Nagai, Y. *Phys. Rev. B* **2016,** *94,* 064515. doi:10.1103/PhysRevB.94.064515
26. Goertzen, S. L.; Tanaka, K.; Nagai, Y. *Phys. Rev. B* **2017,** *95,* 064509. doi:10.1103/PhysRevB.95.064509
27. Koerting, V.; Andersen, B. M.; Flensberg, K.; Paaske, J. *Phys. Rev. B* **2010,** *82,* 245108. doi:10.1103/PhysRevB.82.245108
28. Pershoguba, S. S.; Björnson, K.; Black-Schaffer, A. M.; Balatsky, A. V. *Phys. Rev. Lett.* **2015,** *115,* 116602. doi:10.1103/PhysRevLett.115.116602
29. Głodzik, S.; Ptok, A. *J. Supercond. Novel Magn.* **2018,** *31,* 647. doi:10.1007/s10948-017-4360-6
30. Mashkoori, M.; Björnson, K.; Black-Schaffer, A. M. *Sci. Rep.* **2017,** *7,* 44107. doi:10.1038/srep44107
31. Satori, K.; Shiba, H.; Sakai, O.; Shimizu, Y. *J. Phys. Soc. Jpn.* **1992,** *61,* 3239–3254. doi:10.1143/JPSJ.61.3239
32. Sakai, O.; Shimizu, Y.; Shiba, H.; Satori, K. *J. Phys. Soc. Jpn.* **1993,** *62,* 3181–3197. doi:10.1143/JPSJ.62.3181
33. Sakurai, A. *Prog. Theor. Phys.* **1970,** *44,* 1472. doi:10.1143/PTP.44.1472
34. van Gerven Oei, W.-V.; Tanasković, D.; Žitko, R. *Phys. Rev. B* **2017,** *95,* 085115. doi:10.1103/PhysRevB.95.085115
35. Morr, D. K.; Yoon, J. *Phys. Rev. B* **2006,** *73,* 224511. doi:10.1103/PhysRevB.73.224511
36. Röntynen, J.; Ojanen, T. *Phys. Rev. Lett.* **2015,** *114,* 236803. doi:10.1103/PhysRevLett.114.236803
37. Morr, D. K.; Stavropoulos, N. A. *Phys. Rev. B* **2003,** *67,* 020502. doi:10.1103/PhysRevB.67.020502
38. Kawakami, T.; Hu, X. *Phys. Rev. Lett.* **2015,** *115,* 177001. doi:10.1103/PhysRevLett.115.177001
39. Nadj-Perge, S.; Drozdov, I. K.; Li, J.; Chen, H.; Jeon, S.; Seo, J.; MacDonald, A. H.; Bernevig, B. A.; Yazdani, A. *Science* **2014,** *346,* 602. doi:10.1126/science.1259327
40. Pawlak, R.; Kisiel, M.; Klinovaja, J.; Maier, T.; Kawai, S.; Glatzel, T.; Loss, D.; Meyer, E. *npj Quantum Inf.* **2016,** *2,* 16035. doi:10.1038/npjqi.2016.35
41. Ruby, M.; Pientka, F.; Peng, Y.; von Oppen, F.; Heinrich, B. W.; Franke, K. J. *Phys. Rev. Lett.* **2015,** *115,* 197204. doi:10.1103/PhysRevLett.115.197204
42. Jeon, S.; Xie, Y.; Li, J.; Wang, Z.; Bernevig, B. A.; Yazdani, A. *Science* **2017,** *358,* 772. doi:10.1126/science.aan3670
43. Maśka, M. M.; Gorczyca-Goraj, A.; Tworzydło, J.; Domański, T. *Phys. Rev. B* **2017,** *95,* 045429. doi:10.1103/PhysRevB.95.045429
44. Liu, X.; Li, X.; Deng, D.-L.; Liu, X.-J.; Das Sarma, S. *Phys. Rev. B* **2016,** *94,* 014511. doi:10.1103/PhysRevB.94.014511
45. Stanescu, T. D.; Tewari, S. *J. Phys.: Condens. Matter* **2013,** *25,* 233201. doi:10.1088/0953-8984/25/23/233201
46. Sticlet, D.; Bena, C.; Simon, P. *Phys. Rev. Lett.* **2012,** *108,* 096802. doi:10.1103/PhysRevLett.108.096802

47. Maśka, M. M.; Domański, T. *Sci. Rep.* **2017,** *7,* 16193. doi:10.1038/s41598-017-16323-3
48. Vernek, E.; Penteado, P. H.; Seridonio, A. C.; Egues, J. C. *Phys. Rev. B* **2014,** *89,* 165314. doi:10.1103/PhysRevB.89.165314
49. Deng, M. T.; Vaitiekenas, S.; Hansen, E. B.; Danon, J.; Leijnse, M.; Flensberg, K.; Nygård, J.; Krogstrup, P.; Marcus, C. M. *Science* **2016,** *354,* 1557. doi:10.1126/science.aaf3961
50. Liu, C.-X.; Sau, J. D.; Stanescu, T. D.; Das Sarma, S. *Phys. Rev. B* **2017,** *96,* 075161. doi:10.1103/PhysRevB.96.075161
51. Hoffman, S.; Chevallier, D.; Loss, D.; Klinovaja, J. *Phys. Rev. B* **2017,** *96,* 045440. doi:10.1103/PhysRevB.96.045440
52. Ptok, A.; Kobiałka, A.; Domański, T. *Phys. Rev. B* **2017,** *96,* 195430. doi:10.1103/PhysRevB.96.195430
53. Chevallier, D.; Szumniak, P.; Hoffman, S.; Loss, D.; Klinovaja, J. *Phys. Rev. B* **2018,** *97,* 045404. doi:10.1103/PhysRevB.97.045404
54. Chirla, R.; Moca, C. P. *Phys. Rev. B* **2016,** *94,* 045405. doi:10.1103/PhysRevB.94.045405
55. Prada, E.; Aguado, R.; San-Jose, P. *Phys. Rev. B* **2017,** *96,* 085418. doi:10.1103/PhysRevB.96.085418
56. Barański, J.; Kobiałka, A.; Domański, T. *J. Phys.: Condens. Matter* **2017,** *29,* 075603. doi:10.1088/1361-648X/aa5214
57. Domański, T.; Žonda, M.; Pokorný, V.; Górski, G.; Janiš, V.; Novotný, T. *Phys. Rev. B* **2017,** *95,* 045104. doi:10.1103/PhysRevB.95.045104
58. Mourik, V.; Zuo, K.; Frolov, S. M.; Plissard, S. R.; Bakkers, E. P. A. M.; Kouwenhoven, L. P. *Science* **2012,** *336,* 1003. doi:10.1126/science.1222360
59. Gül, Ö.; Zhang, H.; Bommer, J. D. S.; de Moor, M. W. A.; Car, D.; Plissard, S. R.; Bakkers, E. P. A. M.; Geresdi, A.; Watanabe, K.; Taniguchi, T.; Kouwenhoven, L. P. *Nat. Nanotechnol.* **2018,** *13,* 192. doi:10.1038/s41565-017-0032-8
60. Golub, A. *Phys. Rev. B* **2015,** *91,* 205105. doi:10.1103/PhysRevB.91.205105
61. Bauer, J.; Oguri, A.; Hewson, A. C. *J. Phys.: Condens. Matter* **2007,** *19,* 486211. doi:10.1088/0953-8984/19/48/486211
62. Yamada, Y.; Tanaka, Y.; Kawakami, N. *Phys. Rev. B* **2011,** *84,* 075484. doi:10.1103/PhysRevB.84.075484
63. Martín-Rodero, A.; Levy Yeyati, A. *Adv. Phys.* **2011,** *60,* 899. doi:10.1080/00018732.2011.624266
64. Barański, J.; Domański, T. *J. Phys.: Condens. Matter* **2013,** *25,* 435305. doi:10.1088/0953-8984/25/43/435305
65. Liu, D. E.; Cheng, M.; Lutchyn, R. M. *Phys. Rev. B* **2015,** *91,* 081405. doi:10.1103/PhysRevB.91.081405
66. Elliott, S. R.; Franz, M. *Rev. Mod. Phys.* **2015,** *87,* 137. doi:10.1103/RevModPhys.87.137
67. Ruiz-Tijerina, D. A.; Vernek, E.; Dias da Silva, L. G. G. V.; Egues, J. C. *Phys. Rev. B* **2015,** *91,* 115435. doi:10.1103/PhysRevB.91.115435
68. Lee, M.; Lim, J. S.; López, R. *Phys. Rev. B* **2013,** *87,* 241402. doi:10.1103/PhysRevB.87.241402
69. Cheng, M.; Becker, M.; Bauer, B.; Lutchyn, R. M. *Phys. Rev. X* **2014,** *4,* 031051. doi:10.1103/PhysRevX.4.031051
70. van Beek, I. J.; Braunecker, B. *Phys. Rev. B* **2016,** *94,* 115416. doi:10.1103/PhysRevB.94.115416
71. Weymann, I. *J. Phys.: Condens. Matter* **2017,** *29,* 095301. doi:10.1088/1361-648X/aa5526
72. Weymann, I.; Wójcik, K. P. *Phys. Rev. B* **2017,** *95,* 155427. doi:10.1103/PhysRevB.95.155427
73. López, R.; Lee, M.; Serra, L.; Lim, J. S. *Phys. Rev. B* **2014,** *89,* 205418. doi:10.1103/PhysRevB.89.205418
74. Tanaka, Y.; Kawakami, N.; Oguri, A. *J. Phys. Soc. Jpn.* **2007,** *76,* 074701. doi:10.1143/JPSJ.76.074701
75. Vecino, E.; Martín-Rodero, A.; Levy Yeyati, A. *Phys. Rev. B* **2003,** *68,* 035105. doi:10.1103/PhysRevB.68.035105
76. Béri, B.; Cooper, N. R. *Phys. Rev. Lett.* **2012,** *109,* 156803. doi:10.1103/PhysRevLett.109.156803
77. Galpin, M. R.; Mitchell, A. K.; Temaismithi, J.; Logan, D. E.; Béri, B.; Cooper, N. R. *Phys. Rev. B* **2014,** *89,* 045143. doi:10.1103/PhysRevB.89.045143
78. Plugge, S.; Zazunov, A.; Eriksson, E.; Tsvelik, A. M.; Egger, R. *Phys. Rev. B* **2016,** *93,* 104524. doi:10.1103/PhysRevB.93.104524
79. Béri, B. *Phys. Rev. Lett.* **2017,** *119,* 027701. doi:10.1103/PhysRevLett.119.027701
80. Jacob, D.; Soriano, M.; Palacios, J. J. *Phys. Rev. B* **2013,** *88,* 134417. doi:10.1103/PhysRevB.88.134417

License and Terms

The definitive version of this article is the electronic one which can be found at: doi:10.3762/bjnano.9.129

IOP Publishing Journal of Physics: Condensed Matter
J. Phys.: Condens. Matter **32** (2020) 235501 (8pp) https://doi.org/10.1088/1361-648X/ab786d

In-gap states of magnetic impurity in quantum spin Hall insulator proximitized to a superconductor

Szczepan Głodzik[1] **and Tadeusz Domański**

Institute of Physics, M. Curie-Skłodowska University, 20-031 Lublin, Poland

E-mail: szglodzik@kft.umcs.lublin.pl and doman@kft.umcs.lublin.pl

Received 3 October 2019, revised 2 January 2020
Accepted for publication 20 February 2020
Published 12 March 2020

Abstract

We study in-gap states of a single magnetic impurity embedded in a honeycomb monolayer which is deposited on superconducting substrate. The intrinsic spin–orbit coupling induces the quantum spin Hall insulating (QSHI) phase gapped around the Fermi energy. Under such circumstances we consider the emergence of Shiba-like bound states driven by the superconducting proximity effect. We investigate their topography, spin-polarization and signatures of the quantum phase transition manifested by reversal of the local currents circulating around the magnetic impurity. These phenomena might be important for more exotic in-gap quasiparticles in such complex nanostructures as magnetic nanowires or islands, where the spin–orbit interaction along with the proximity induced electron pairing give rise to topological phases hosting the protected boundary modes.

Keywords: bound states, Yu-Shiba-Rusinov states, superconductivity

(Some figures may appear in colour only in the online journal)

1. Introduction

Even a tiny content of impurities introduced to insulating and semiconducting materials can tremendously affect their charge transport, contributing particle/hole carriers from the donor/acceptor level to the conduction/valence band. This is in contrast with completely opposite (destructive) effect played by the magnetic impurities in superconductors where they break the Cooper pairs, leading to formation of the bound Yu-Shiba-Rusinov (YSR) or briefly Shiba states inside the energy gap [1]. These in-gap states can eventually activate the charge transport in interfaces and heterostructures, owing to the anomalous particle-to-hole (or hole-to-particle) Andreev scattering mechanism [2]. In all such cases impurities are intimately related with existence of the subgap states, whose nature differs depending on the host material. One may hence ask, whether *there can be established any connection between such contrasting in-gap states of insulators and superconductors?*

A promising platform for addressing this question could be a graphene sheet deposited on *s*-wave superconducting substrate. Electrons of such carbon atoms layer reveal a number of unique properties. Besides their Dirac-like behavior, stemming simply from a honeycomb geometry, the intrinsic spin–orbit coupling (SOC) can induce the QSHI phase [3] with the spin currents circulating along its boundaries. Such effect has been experimentally observed in graphene randomly decorated with the dilute Bi_2Te_3 nanoparticles [4] and in a heterostructure, consisting of a monolayer of WTe_2 placed between two layers of hexagonal boron nitride which has revealed topological properties up to relatively high temperatures of about 100 K [5]. Further phenomena related with electron pairing arise when a graphene sheet is proximitized to superconducting material [6–11]. For instance, graphene deposited on aluminum films acquires superconductivity with the effective coherence length $\xi \simeq 400$ nm [11], whereas grown on rhenium it shows high transparency of the interface, with the induced pairing gap $\Delta = 330 \pm 10\,\mu$eV [8]. Upon introducing impurities into proximitized graphene, there emerge various in-gap states, manifesting either the topologically trivial or non-trivial phases [12]. Another system for investigating the bound states of magnetic impurities might be possible in bilayer graphene, where upon twisting the carbon

[1] The author to whom any correspondence to be addressed.

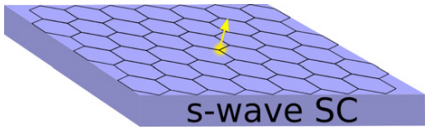

Figure 1. Scheme of a magnetic impurity embedded in a honeycomb monolayer and proximitized to *s*-wave superconductor.

sheets to a small 'magic' angle [13, 14] or tuning the interlayer coupling [15] the intrinsic unconventional superconducting phase is induced.

Here we investigate the properties of in-gap bound states formed at magnetic impurity embedded into the single honeycomb two-dimensional layer and proximitized to superconductor (figure 1), discussing feasible tools to unambiguously distinguish their Shiba-type character in presence of the QSHI phase. This problem has recently gained a great deal of interest, both experimentally [16–20] and theoretically [21–23] because similar magnetic structures, e.g. nanowires [24, 25] and nanostripes [26, 27] could enable realization of the Majorana quasiparticles.

The spin–orbit gap in graphene is often claimed to be rather small, although Sichau et al [28] have estimated its magnitude (by means of the resistively-detected electron spin resonance) to be 40 μeV. Under such circumstances the superconducting gap might be comparable to the SOC and this would be sufficient for appearance of the in-gap bound states strictly related with electron pairing. In what follows we perform a systematic study of the Shiba states, inspecting (a) their spatial extent and topography, (b) magnetic polarization, and (c) observable features of the quantum phase ($0-\pi$) transition manifested by reversal of the orbital currents circulating around the impurity site.

The paper is organized as follows. In section 2 we introduce the microscopic model and present the method for studying the bound states of magnetic impurity existing in honeycomb sheet. Section 3 discusses influence of the insulating and superconducting phases on the in-gap quasiparticles and presents their detailed properties. Finally, in section 4, we summarize the results.

2. Model and method

We describe the magnetic impurity embedded in a honeycomb sheet (figure 1) by the tight-binding Hamiltonian

$$\hat{H} = \hat{H}_{\rm imp} + \hat{H}_{K-M} + \hat{H}_{\rm Rashba} + \hat{H}_{\rm prox}. \tag{1}$$

In what follows, this impurity is treated classically

$$\hat{H}_{\rm imp} = -J\left(c^{\dagger}_{\mathbf{i}_0\uparrow}c_{\mathbf{i}_0\uparrow} - c^{\dagger}_{\mathbf{i}_0\downarrow}c_{\mathbf{i}_0\downarrow}\right), \tag{2}$$

where we denote the impurity site as $\mathbf{i}_0$, and we apply the Kane–Mele scenario [3] for description of the itinerant electrons

$$\begin{aligned}\hat{H}_{K-M} = &-t\sum_{\langle\mathbf{ij}\rangle\sigma\sigma'} c^{\dagger}_{\mathbf{i}\sigma}c_{\mathbf{j}\sigma} - \mu\sum_{\mathbf{i}\sigma} c^{\dagger}_{\mathbf{i}\sigma}c_{\mathbf{i}\sigma}\\ &+ i\lambda_{\rm SO}\sum_{\langle\langle\mathbf{ij}\rangle\rangle\sigma\sigma'} \nu_{\mathbf{ij}}c^{\dagger}_{\mathbf{i}\sigma}s_z^{\sigma\sigma'}c_{\mathbf{j}\sigma'},\end{aligned} \tag{3}$$

with the nearest-neighbor hopping t, the chemical potential μ (which we assume to be zero unless otherwise stated), and the imaginary, spin-dependent, next-nearest neighbor hopping amplitude $\lambda_{\rm SO}$. The latter term is responsible for inducing the helical edge states. The sign $\nu_{\mathbf{ij}} = \pm 1$ depends on the direction of electron hopping between the next-nearest-neighbor sites ($+1$ for clockwise and -1 for anticlockwise). The hopping terms involve the summation over (next-)nearest $\langle\langle\mathbf{ij}\rangle\rangle$ $\langle\mathbf{ij}\rangle$ neighbors. Since the substrate violates the mirror inversion $z \longrightarrow -z$ symmetry, we also consider the Rashba spin–orbit interactions

$$\hat{H}_{\rm Rashba} = i\lambda_R\sum_{\langle\mathbf{ij}\rangle\sigma\sigma'} c^{\dagger}_{\mathbf{i}\sigma}\left(\mathbf{s}^{\sigma\sigma'}\times\mathbf{d}_{\mathbf{ij}}\right)_{\vec{z}}c_{\mathbf{j}\sigma'}. \tag{4}$$

Here $\mathbf{s}^{\sigma\sigma'}$ is the vector of the Pauli matrices, referring to spin $\frac{1}{2}$, and the vector $\mathbf{d}_{\mathbf{ij}}$ connects site $\mathbf{i}$ with its nearest neighbor site $\mathbf{j}$.

Finally, we assume that the honeycomb layer is proximitized to *s*-wave superconductor

$$\hat{H}_{\rm prox} = \sum_{\mathbf{i}}\left(\Delta c^{\dagger}_{\mathbf{i}\uparrow}c^{\dagger}_{\mathbf{i}\downarrow} + \text{h.c.}\right), \tag{5}$$

which induces the on-site pairing Δ. For computing the observables of interest, we perform the Bogoliubov–Valatin transformation

$$c_{\mathbf{i}\sigma} = \sum_{n}{}' (u^n_{\mathbf{i}\sigma}\gamma_n - \sigma v^{*n}_{\mathbf{i}\sigma}\gamma^{\dagger}_n), \tag{6}$$

where $'$ denotes summation over the positive eigenvalues, and numerically solve the equations

$$\sum_{\mathbf{j}}\hat{H}_{\mathbf{ij}}\hat{\Phi}_{\mathbf{j}} = E_n\hat{\Phi}_{\mathbf{i}}, \tag{7}$$

in the auxiliary (Nambu spinor) representation $\Phi_{\mathbf{i}} = (u^n_{\mathbf{i}\uparrow}, u^n_{\mathbf{i}\downarrow}, v^n_{\mathbf{i}\uparrow}, v^n_{\mathbf{i}\downarrow})^{\rm T}$. The matrix elements read

$$\hat{H}_{\mathbf{ij}} = \begin{pmatrix} \tilde{t}_{\mathbf{ij}\uparrow} & \lambda_R^{\uparrow\downarrow} & 0 & \Delta \\ \lambda_R^{\downarrow\uparrow} & \tilde{t}_{\mathbf{ij}\downarrow} & \Delta & 0 \\ 0 & \Delta^* & -(\tilde{t}_{\mathbf{ij}\uparrow})^* & (\lambda_R^{\uparrow\downarrow})^* \\ \Delta^* & 0 & (\lambda_R^{\downarrow\uparrow})^* & -(\tilde{t}_{\mathbf{ij}\downarrow})^* \end{pmatrix}, \tag{8}$$

where $\tilde{t}_{\mathbf{ij}\sigma} = t_{\mathbf{j}}\delta_{\langle\mathbf{ij}\rangle} - (\mu + \sigma J\delta_{\mathbf{ii_0}})\delta_{\mathbf{ij}} + \sigma i\lambda_{\rm SO}\nu_{\mathbf{j}}\delta_{\langle\langle\mathbf{ij}\rangle\rangle}$ and $\lambda_R^{\sigma\sigma'}$ $= i\lambda_R\sum_{\sigma\sigma'\langle\mathbf{j}\rangle}\left(\mathbf{s}^{\sigma\sigma'}\times\mathbf{d}_{\mathbf{ij}}\right)_{\vec{z}} = (\lambda_R^{\sigma'\sigma})^*$.

Results discussed in this paper are obtained from numerical diagonalization of the Hamiltonian matrix on 40×40 lattice with the periodic boundary conditions in both directions. We do not consider any intrinsic pairing mechanism, assuming that it originates solely from the proximity effect (5). Self-consistent treatment of electron pairing is in general important [29, 30], however, in the present case it would not imply any significant changes of the local order parameter [31].

3. Subgap quasiparticles

For a systematic analysis of the subgap quasiparticles we shall start by discussing the in-gap states hosted in the insulating (QSHI) phase and next consider their mutation caused by the electron pairing Δ.

3.1. Impurity bound states in QSHI phase

Let us consider the magnetic impurity in a finite-size graphene layer, neglecting the superconducting substrate ($\Delta = 0$). Figure 2 shows how the intrinsic spin–orbit interaction affects the low-energy quasiparticles. We notice that insulating energy gap of the QSHI phase grows linearly upon increasing the Kane–Mele coupling and, around $\lambda_{\rm SO} = 0.2t$, it saturates to $\sim 1t$. Concomitantly there appear two in-gap states (purple-dotted lines in figure 2), which are fully spin-polarized. Similar bound states have been previously found for a single impurity whose magnetic moment is parallel to the graphene plane [32]. When impurity is close enough to a perimeter of the sample they have been shown to hybridize with the topological edge states, inducing antiresonances in the transmission matrix. It has been also emphasized, that the bound states around point impurity in a two-dimensional insulator could distinguish between the topological and trivial phases of the host material [33].

Bottom panel in figure 2 displays the topography of the occupied ($E < E_F$) bound state for two different values of $\lambda_{\rm SO}$. From careful examination of the spectral weight on the lattice sites adjacent to the impurity, we can notice an oscillatory decay of the wavefunction of the bound state. Practically its spatial extent does not exceed 10 atomic distances, and it quickly vanishes for higher magnitudes of the SOC. This loss of spatial extent is accompanied by the simultaneous reduction of the spectral weight of the bound state. Closely related effects have been previously pointed out for the magnetic [34–38], non-magnetic [12, 39, 40] and both types of the scattering potential as well [41–43].

3.2. Shiba quasiparticles

Upon coupling the honeycomb lattice to superconducting substrate, the energy gap around the Fermi energy results from a combined effect of the proximity induced pairing ($\Delta \neq 0$) and the insulating phase. In general, these phenomena are known to be competitive as indeed manifested by suppression of the bulk order parameter $\langle c_{i\downarrow} c_{i\uparrow}\rangle$ (section 3.3). From a perspective of the local physics (at impurity site), however, relationship between the QSHI and superconducting phases is much more intriguing. By gradually increasing the pairing potential Δ, what can be achieved e.g. by reducing the external magnetic field or varying the temperature, we observe *development of the Shiba quasiparticles* [1] *directly from in-gap quasiparticles of the insulating phase* (figure 3). Let us remark, that direct transition from the insulating to superconducting phase has been theoretically considered for bulk materials within the mean field [44] and more sophisticated many-body methods [45]. Such scenario could be practically realized in variety of systems, e.g. thin superconducting films [46], at oxide interfaces [47], in organic materials [48] and possibly in the doped cuprate superconductors [49]. In the present context we focus on the subgap Shiba-like quasiparticles, which to our knowledge have not been considered so far. To compare our results with less exotic situation, we plot in the bottom panel of figure 3 the same situation as in the top panel, but with a value of chemical potential which is known to close the spin–orbit gap. The system is then metallic and opening the superconducting gap results in a picture similar to traditionally understood Shiba states [1].

Let us focus in more detail on the Shiba quasiparticles. In the present case they do not obey the original formula $E_{\rm YSR} = \pm\Delta\,(1 - \pi\rho_n(E_F)J)\,/\,(1 + \pi\rho_n(E_F)J)$ derived for conventional superconductors because of the vanishing normal density of states in graphene $\rho_n(E_F) = 0$ [50, 51].

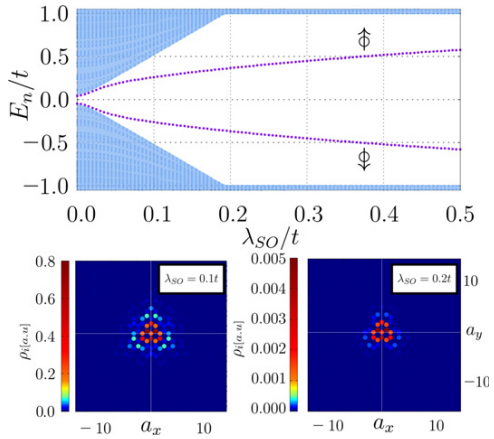

Figure 2. Low energy spectrum of the honeycomb lattice with the single magnetic impurity as a function of the Kane–Mele coupling $\lambda_{\rm SO}$, assuming $J = 6t$ and $\lambda_R = 0$, $\Delta = 0$. Bottom panel: topography of the occupied bound state for $\lambda_{\rm SO} = 0.1t$ and $\lambda_{\rm SO} = 0.2t$.

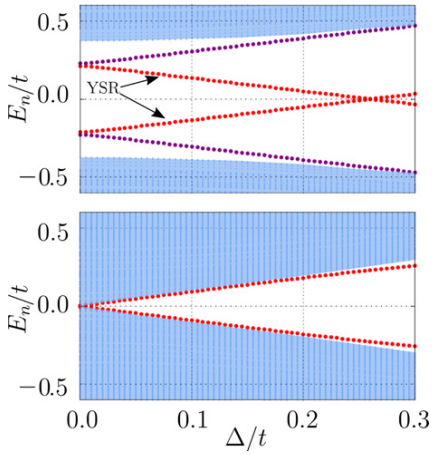

Figure 3. Top panel: emergence of YSR states (dotted red lines) from in-gap quasiparticles of the QSHI phase (dotted violet lines) driven by the proximity induced pairing Δ for $J = 6t$, $\lambda_{\rm SO} = 0.1t$, $\mu = 0$. Bottom panel: same but for $\mu = 3\sqrt{3}\lambda_{\rm SO}$.

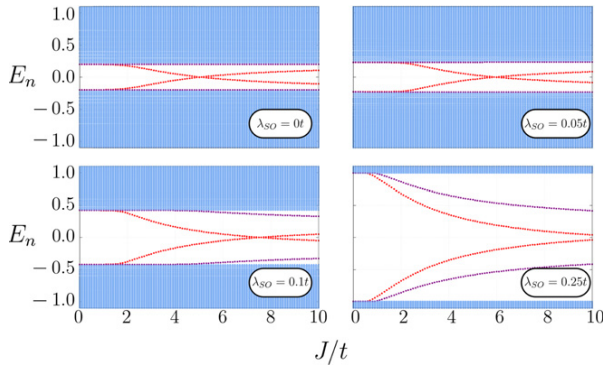

Figure 4. Evolution of the subgap spectrum with respect to the impurity potential J obtained for $\Delta = 0.2t$, $\lambda_R = 0.05t$ and several values of λ_{SO}, as indicated. The dotted red and violet lines refer to the YSR states and in-gap quasiparticles of insulating phase, respectively.

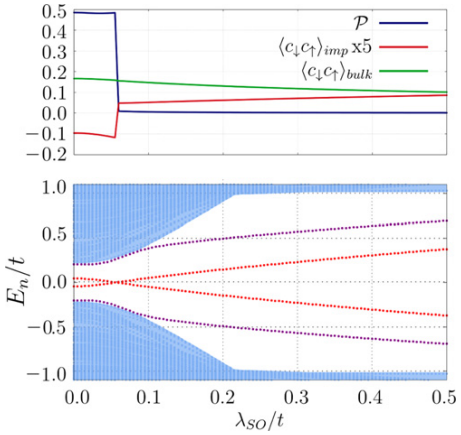

Figure 5. The polarization $\mathcal{P}$ and order parameter at the impurity site and for the bulk as functions of λ_{SO} (top panel). QPT driven at $\lambda_{SO} \simeq 0.05t$ (bottom panel). Results obtained for the model parameters $\Delta = 0.2t$, $\lambda_R = 0.05t$, and $J = 6t$.

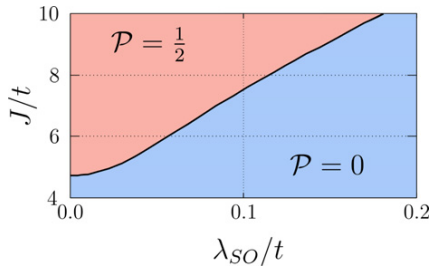

Figure 6. Variation of the QPT point (corresponding to crossing of the Shiba states) versus the Kane–Mele coupling λ_{SO} and impurity potential J.

Figure 4 displays the quasiparticle energies obtained numerically for our model as a function of the magnetic potential J for several values of Kane–Mele coupling λ_{SO}. The dense (light-blue) dots refer to a continuum, whereas the single dotted lines represent the in-gap bound states. Amongst these in-gap branches we can recognize the Shiba-like quasiparticles by their strong variation with respect to J. In particular, at some critical value J_c they eventually cross each other, signaling a qualitative changeover of the ground state [52]. This quantum phase transition (QPT) manifests itself by: sign-reversal of the local order parameter ($0 - \pi$ transition), abrupt onset of the spin polarization (section 3.3), and by qualitative changes (both, in magnitude and vorticity) of the locally circulating currents (section 3.5).

Our analysis indicates, that Kane–Mele coupling λ_{SO} affects the QPT, by (i) shifting the critical coupling J_C to higher values (figures 4 and 6) and (ii) leading to substantial changes both in topography and spatial extent of the Shiba-like states (section 3.4). Thus the spin–orbit interaction weakens the efficiency of magnetic coupling J between the impurity and conduction electrons. Furthermore, the Shiba states no longer merge with a continuum even in the extremely strong coupling limit $J \to \infty$, in stark contrast to behavior of magnetic impurities in triangular lattice of the two-dimensional superconductor [21] where the Kane–Mele interaction is absent.

3.3. QPT

Let us now focus on the QPT, driven by the intrinsic SOC. Even though variation of λ_{SO} would be rather not feasible experimentally, we deem that its effect can be instructive for understanding mutual relationship between the on-site pairing and the spin–orbit interaction. Bottom panel of figure 5 presents the eigenenergies, corresponding to the same set of model parameters as in figure 2 but in presence of finite Δ and λ_R. We observe that energy gap of superconducting states ($\sim 0.2t$) gradually evolves into the gap of QSHI which saturates around $\lambda_{SO} \simeq 0.2t$. We have selected strong enough magnetic coupling $J = 6t$ which allows for the QPT driven by λ_{SO}. The upper panel of figure 5 displays the bulk polarization, defined as

$$\mathcal{P} = \frac{1}{2}\sum_{\mathbf{i}} \left(\langle n_{\mathbf{i}\uparrow} \rangle - \langle n_{\mathbf{i}\downarrow} \rangle \right), \tag{9}$$

where $n_{\mathbf{i}\sigma} = \sum_n' \left[|u^n_{\mathbf{i}\sigma}|^2 f(E_n, T) + |v^n_{\mathbf{i}\sigma}|^2 f(-E_n, T) \right]$ is the average number of electrons with spin σ at site $\mathbf{i}$, the order parameter at the impurity site, and its value averaged over the entire sample. At $\lambda_{SO} \approx 0.05t$ the order parameter at impurity site reverses its sign and its absolute value gradually increases upon increasing the Kane–Mele coupling. Simultaneously the bulk magnetization is abruptly quenched as the system shifts to the unpolarized ground state. These characteristic features of the QPT [1] in the present case originate from the intrinsic SOC. On the other hand, the bulk order parameter does not undergo any dramatic changes (it slowly diminishes upon increasing λ_{SO}). Such conditions should be taken into account when considering formation of the Majorana bound states at the ends of magnetic chains deposited on the proximitized honeycomb sheet [25].

The shift of J_c with increasing λ_{SO} is displayed as a phase diagram in figure 6. The black continuous line denotes the

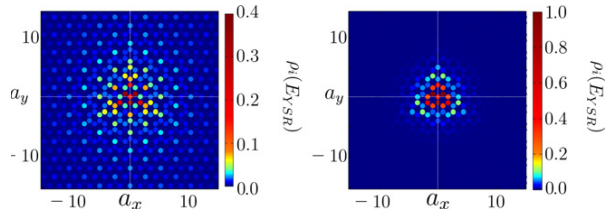

Figure 7. Spatial distribution of the occupied (negative value) Shiba quasiparticle obtained for $\Delta = 0.2t$, $\lambda_R = 0.05t$, $J = 4t$, using $\lambda_{SO} = 0$ (left panel) and $\lambda_{SO} = 0.1t$ (right panel). The density of states $\rho_i(E_{Shiba})$ is normalized with respect to the largest value in the bottom panel.

critical coupling J_c at different values of λ_{SO}. Initially the shift of QPT is not meaningful, but starting from $\lambda_{SO} = 0.03t$ we observe onset of a linear variation. This increase also points out, that the spin–orbit interaction suppresses the effective coupling of the impurity spin with the conduction electrons [36].

3.4. Topography of Shiba quasiparticles

Let us now inspect the real-space shape (topography) of the Shiba states. Figure 7 presents spatial maps of the density of states at the energy of electron-like (occupied) bound state, both in absence and in presence of the intrinsic spin–orbit interaction. One can see that without the Kane–Mele interaction, the topography of Shiba state has its usual character with exponential variation of the wavefunction $\sim \exp(-r/\xi)$.

We remark, that spectral weight is differently distributed in each sublattice. Close to the impurity site $r_0 = (0, 0)$ most of the spectral weight of the Shiba quasiparticles appears in the B-sublattice sites, whereas further away the A-sublattice (in which the impurity resides) gains more and more spectral weight. Also the rotational symmetry of the topographic shape reveals a bipartite character. Close to the impurity site the shape has a C_3 rotational symmetry, reflecting the fact that each site has three nearest-neighbors (cf bottom panels in figure 2), whereas at larger distances, the spectral weight distributed in the A sublattice resembles a hexagon with C_6 rotational symmetry. Precise evaluation of the bound states wavefuntions in this case would be a challenging task for future experimental measurements. Topography of the bound states changes dramatically, when the intrinsic SOC is taken into account. Bottom panel in figure 7 illustrates a strong tendency towards localization of the Shiba states in vicinity of the magnetic impurity. Their spectral weight is spread over a few adjacent sites and we no longer observe any preference for dominance of only one sublattice. These properties of the Shiba states resemble the features typical for in-gap quasiparticles of magnetic impurity embedded in a non-superconducting QSHI. Such reduction of the spatial extent could be important for engineering the topologically non-trivial phases, as e.g. chain of magnetic impurities can host the Majorana quasiparticles only when the bound states of dilute impurities hybridize to form a Shiba band capable of undergoing the topological phase transition.

3.5. Local currents

Another signature of the QPT in our system can be seen by currents induced around the magnetic impurity [53]. We compute the local charge flow, using the Heisenberg equation $i\hbar\frac{\partial\langle n_i\rangle}{\partial t} = \langle[n_i, \hat{H}]\rangle$. Setting the convention $\hbar \equiv 1$, and ignoring the terms which merely induce on-site fluctuations of charge, we obtain

$$\begin{aligned}\frac{\partial\langle n_{\mathbf{i}}\rangle}{\partial t} = &-it\sum_{\sigma\langle\mathbf{j}\rangle}\left(\langle c^{\dagger}_{\mathbf{i}\sigma}c_{\mathbf{j}\sigma}\rangle - \langle c^{\dagger}_{\mathbf{j}\sigma}c_{\mathbf{i}\sigma}\rangle\right)\\ &+\lambda_{SO}\sum_{\sigma\sigma'\langle\langle\mathbf{j}\rangle\rangle}\left(\nu_{\mathbf{ij}}s_z^{\sigma\sigma'}\langle c^{\dagger}_{\mathbf{i}\sigma'}c_{\mathbf{j}\sigma}\rangle - \nu_{\mathbf{ji}}s_z^{\sigma'\sigma}\langle c^{\dagger}_{\mathbf{j}\sigma'}c_{\mathbf{i}\sigma}\rangle\right)\\ &+\lambda_R\sum_{\sigma\sigma'\langle\mathbf{j}\rangle}\Big[\Big(\mathbf{s}^{\sigma\sigma'}\times\mathbf{d}_{\mathbf{ij}}\Big)_{\vec{z}}\langle c^{\dagger}_{\mathbf{i}\sigma}c_{\mathbf{j}\sigma'}\rangle\\ &-\Big(\mathbf{s}^{\sigma'\sigma}\times\mathbf{d}_{\mathbf{ji}}\Big)_{\vec{z}}\langle c^{\dagger}_{\mathbf{j}\sigma'}c_{\mathbf{i}\sigma}\rangle\Big].\end{aligned} \tag{10}$$

Applying the Bogoliubov–Valatin transformation (6), and making use of the fact that if $\Phi_{\mathbf{i}} = (u^n_{\mathbf{i}\uparrow}, u^n_{\mathbf{i}\downarrow}, v^n_{\mathbf{i}\uparrow}, v^n_{\mathbf{i}\downarrow})^{\mathrm{T}}$ is the eigenvector of matrix (8) with an eigenvalue E_n, then $\tilde{\Phi}_{\mathbf{i}} = (-v^{n*}_{\mathbf{i}\uparrow}, v^{n*}_{\mathbf{i}\downarrow}, -u^{n*}_{\mathbf{i}\uparrow}, u^{n*}_{\mathbf{i}\downarrow})^{\mathrm{T}}$ is also an eigenvector of the same matrix, but with an eigenvalue $-E_n$, we get

$$\begin{aligned}\langle\widehat{J}_{\mathbf{i}}\rangle = &-it\sum_{\langle\mathbf{j}\rangle\sigma n}\left(u^{n*}_{\mathbf{i}\sigma}u^{n}_{\mathbf{j}\sigma}f_{FD}(E_n) - \text{c.c.}\right)\\ &+\sum_{\langle\mathbf{j}\rangle\sigma\sigma' n}\left(\lambda_R^{\sigma\sigma'}u^{n*}_{\mathbf{i}\sigma}u^{n}_{\mathbf{j}\sigma'}f_{FD}(E_n) + \text{c.c.}\right)\\ &+\lambda_{SO}\sum_{\langle\langle\mathbf{j}\rangle\rangle\sigma\sigma' n}\left(\nu_{\mathbf{ij}}s_z^{\sigma\sigma'}u^{n*}_{\mathbf{i}\sigma}u^{n}_{\mathbf{j}\sigma'}f_{FD}(E_n) + \text{c.c.}\right),\end{aligned} \tag{11}$$

where $\lambda_R^{\sigma\sigma'}$ defined in section 2.

Figure 8 shows the real-space maps of microscopic currents and the maximum magnitude of bond current in the system with respect to the impurity coupling strength J. We emphasize, that reversal of these currents vorticity (compare the top panels of figure 8) occurs exclusively when the system is in the non-trivial QSHI phase. Explanation of this behavior could be the following. It has been shown in reference [36] that the intrinsic SOC supresses the effective coupling J of impurity with the conduction electrons. We have observed that with $\lambda_{SO} = 0$ the sites belonging to the same sublattice as the impurity site polarize easily in the direction of the magnetic moment of the impurity. This effect is pronounced only for $J > J_C$, as more sites around the impurity align their magnetic moments. The situation changes with increasing SOC which weakens the effective impurity coupling. For small J, the magnetic moment is hardly screened by the closest neighboring sites and becomes more efficient when the coupling exceeds the critical value J_C, forcing the neighboring sites to align their magnetization with the impurity. This in turn reverses the direction of the current. The Shiba states (labeled YSR in red vector plots in figure 8) are the ones that cross the Fermi energy during the QPT, hence only their contribution to the current shows this change of direction, in contrast to the bound states (BS in blue vector plots in figure 8) discussed in section 3.1. Those states hardly change their energy with increasing J, and their contribution to the current does not change during the QPT. Bottom

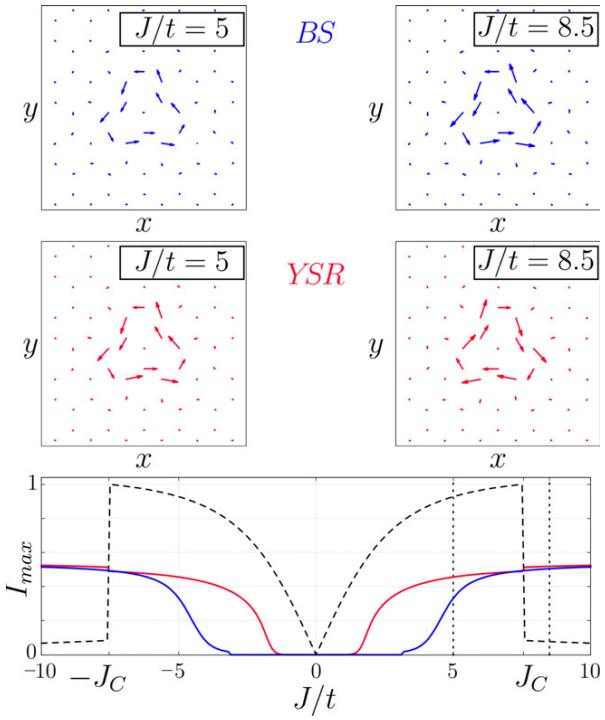

Figure 8. Vector maps of the currents around the magnetic impurity obtained for $J = 5t$ (left) and $J = 8.5t$ (right) presenting contributions of QSHI bound states (BS) and Shiba states (YSR). Bottom panel shows the maximum current versus the coupling J when taking into account the whole spectrum (black dashed line), only QSHI bound states and Shiba states (blue and red lines respectively). Other parameters: $\Delta = 0.2t$, $\lambda_{SO} = 0.1t$, $\lambda_R = 0.05t$.

panel in figure 8 presents the maximum value of the current in the system. When summing over every state n in equation (11), the current drops discontinuously at QPT. This is because as can be observed from the contribution of only the Shiba states (red) and the QSHI bound states (blue), after the reversal of current direction of the Shiba states, both contributions compete, and the effective maximum current is greatly reduced. Detection of such orbital patterns might be performed using an integrated quantum imaging platform where graphene sheet is connected to an array of the atomic-sized magnetic sensors [54, 55] or local conductivity atomic force microscopy suitable for probing electronic current paths with a diameter in the nanometer range [56].

4. Conclusions

We have theoretically investigated the energetic, magnetic and topographic features of in-gap quasiparticles of a single magnetic impurity embedded in the graphene sheet and proximitized to the superconducting substrate. We have shown that subtle interplay between the intrinsic spin–orbit interaction (responsible for the energy gap of the QSHI phase) and the proximity-induced electron pairing enables *emergence of the Shiba-type quasiparticles directly from in-gap states of the insulating phase*. We have discussed in detail this intriguing behavior and proposed several methods for its empirical verification.

Furthermore we have found, that upon varying either the magnetic coupling J (feasible in STM experiments [18]) or strength of the spin–orbit coupling λ_{SO} a pair of the Shiba bound states could cross at the Fermi energy, causing quantum phase transition of the ground state. This usually leads to sign-change of the local order parameter [1], but in the present situation it would be also uniquely manifested by a reversal of the vorticity and abrupt change of the absolute magnitude of the local currents circulating around the impurity site. Our numerical calculations have additionally revealed, that the spin–orbit coupling pushes such QPT crossing towards much higher values of J and substantially reduces the extent of Shiba states (similar to the in-gap states of insulating phase), partly affecting their topographic patterns. We have carefully inspected their spatial profiles in each sublattice of the graphene sheet.

We hope that phenomena discussed here for the single-site magnetic defects [57, 58] might stimulate further considerations of the topological insulating and/or superconducting phases in more complex magnetic structures, like nanowires [24, 25], nanoscopic islands [19] or stripes [26, 27], where the Majorana-type quasiparticles can be realized. It would be also worth to extend our study on the quantum impurities, addressing the subgap Kondo physics of the conventional [59, 60] and topological [61] superconductors.

Acknowledgments

This work was supported by National Science Center (NCN, Poland) under the grants 2017/27/N/ST3/01762 (S G) and UMO-2017/27/B/ST3/01911 (T D).

ORCID iDs

Szczepan Głodzik https://orcid.org/0000-0001-7928-9959
Tadeusz Domański https://orcid.org/0000-0003-1977-3989

References

[1] Balatsky A V, Vekhter I and Zhu J-X 2006 Impurity-induced states in conventional and unconventional superconductors *Rev. Mod. Phys.* **78** 373
[2] Heinrich B W, Pascual J I and Franke K J 2018 Single magnetic adsorbates on s-wave superconductors *Prog. Surf. Sci.* **93** 1
[3] Kane C L and Mele E J 2005 Quantum spin Hall effect in graphene *Phys. Rev. Lett.* **95** 226801
[4] Hatsuda K, Mine H, Nakamura T, Li J, Wu R, Katsumoto S and Haruyama J 2018 Evidence for a quantum spin hall phase in graphene decorated with Bi_2Te_3 nanoparticles *Sci. Adv.* **4**
[5] Wu S, Fatemi V, Gibson Q D, Watanabe K, Taniguchi T, Cava R J and Jarillo-Herrero P 2018 Observation of the quantum spin Hall effect up to 100 kelvin in a monolayer crystal *Science* **359** 76–9
[6] Heersche H B, Jarillo-Herrero P, Oostinga J B, Vandersypen L M K and Morpurgo A F 2007 Bipolar supercurrent in graphene *Nature* **446** 56–9
[7] Komatsu K, Li C, Autier-Laurent S, Bouchiat H and Guéron S 2012 Superconducting proximity effect in long

superconductor/graphene/superconductor junctions: From specular Andreev reflection at zero field to the quantum Hall regime *Phys. Rev. B* **86** 115412
[8] Tonnoir C, Kimouche A, Coraux J, Magaud L, Delsol B, Gilles B and Chapelier C 2013 Induced superconductivity in graphene grown on rhenium *Phys. Rev. Lett.* **111** 246805
[9] Han Z, Allain A, Arjmandi-Tash H, Tikhonov K, Feigelman M, Sacépé B and Bouchiat V 2014 Collapse of superconductivity in a hybrid tin–graphene Josephson junction array *Nat. Phys.* **10** 380
[10] Calado V E, Goswami S, Nanda G, Diez M, Akhmerov A R, Watanabe K, Taniguchi T, Klapwijk T M and Vandersypen L M K 2015 Ballistic Josephson junctions in edge-contacted graphene *Nat. Nanotechnol.* **10** 761
[11] Natterer F D, Ha J, Baek H, Zhang D, Cullen W G, Zhitenev N B, Young K and Stroscio J A 2016 Scanning tunneling spectroscopy of proximity superconductivity in epitaxial multilayer graphene *Phys. Rev. B* **93** 045406
[12] González J W and Fernández-Rossier J 2012 Impurity states in the quantum spin Hall phase in graphene *Phys. Rev. B* **86** 115327
[13] Cao Y, Fatemi V, Fang S, Watanabe K, Taniguchi T, Kaxiras E and Jarillo-Herrero P 2018 Unconventional superconductivity in magic-angle graphene superlattices *Nature* **556** 43
[14] Lu X *et al* 2019 Superconductors, orbital magnets and correlated states in magic-angle bilayer graphene *Nature* **574** 653
[15] Yankowitz M, Chen S, Polshyn H, Zhang Y, Watanabe K, Taniguchi T, Graf D, Young A F and Dean C R 2019 Tuning superconductivity in twisted bilayer graphene *Science* **363** 1059 https://science.sciencemag.org/content/363/6431/1059.full.pdf
[16] Ménard G C *et al* 2015 Coherent long-range magnetic bound states in a superconductor *Nat. Phys.* **11** 1013
[17] Hatter N, Heinrich B W, Rolf D and Franke K J 2017 Scaling of Yu-Shiba-Rusinov energies in the weak-coupling Kondo regime *Nat. Commun.* **8** 2016
[18] Farinacci L, Ahmadi G, Reecht G, Ruby M, Bogdanoff N, Peters O, Heinrich B W, von Oppen F and Franke K J 2018 Tuning the coupling of an individual magnetic impurity to a superconductor: quantum phase transition and transport *Phys. Rev. Lett.* **121** 196803
[19] Ménard G C, Brun C, Leriche R, Trif M, Debontridder F, Demaille D, Roditchev D, Simon P and Cren T 2019 Yu-Shiba-Rusinov bound states versus topological edge states in Pb/Si(111) *Eur. Phys. J. Special Topics* **227** 2303–13
[20] Kezilebieke S, Dvorak M, Ojanen T and Liljeroth P 2018 Coupled Yu-Shiba-Rusinov states in molecular dimers on $NbSe_2$ *Nano Lett.* **18** 2311–5
[21] Ptok A, Głodzik S and Domański T 2017 Yu-Shiba-Rusinov states of impurities in a triangular lattice of $NbSe_2$ with spin-orbit coupling *Phys. Rev. B* **96** 184425
[22] Körber S, Trauzettel B and Kashuba O 2018 Collective Yu-Shiba-Rusinov states in magnetic clusters at superconducting surfaces *Phys. Rev. B* **97** 184503
[23] Senkpiel J *et al* 2019 Robustness of Yu-Shiba-Rusinov resonances in the presence of a complex superconducting order parameter *Phys. Rev. B* **100** 014502
[24] Christensen M H, Schecter M, Flensberg K, Andersen B M and Paaske J 2016 Spiral magnetic order and topological superconductivity in a chain of magnetic adatoms on a two-dimensional superconductor *Phys. Rev. B* **94** 144509
[25] Teixeira R L R C, Kuzmanovski D, Black-Schaffer A M and Dias da Silva L G G V 2019 Gap oscillations and Majorana bound states in magnetic chains on superconducting honeycomb lattices *Phys. Rev. B* **99** 035127
[26] Fornieri A *et al* 2019 Evidence of topological superconductivity in planar Josephson junctions *Nature* **569** 89
[27] Ren H *et al* 2019 Topological superconductivity in a phase-controlled Josephson junction *Nature* **569** 93
[28] Sichau J, Prada M, Anlauf T, Lyon T J, Bosnjak B, Tiemann L and Blick R H 2019 Resonance microwave measurements of an intrinsic spin-orbit coupling gap in graphene: A possible indication of a topological state *Phys. Rev. Lett.* **122** 046403
[29] Meng T, Klinovaja J, Hoffman S, Simon P and Loss D 2015 Superconducting gap renormalization around two magnetic impurities: From Shiba to Andreev bound states *Phys. Rev. B* **92** 064503
[30] Hoffman S, Klinovaja J, Meng T and Loss D 2015 Impurity-induced quantum phase transitions and magnetic order in conventional superconductors: Competition between bound and quasiparticle states *Phys. Rev. B* **92** 125422
[31] Black-Schaffer A M 2011 Self-consistent superconducting proximity effect at the quantum spin Hall edge *Phys. Rev. B* **83** 060504
[32] Zheng J H and Cazalilla M A 2018 Nontrivial interplay of strong disorder and interactions in quantum spin-Hall insulators doped with dilute magnetic impurities *Phys. Rev. B* **97** 235402
[33] Slager R J, Rademaker L, Zaanen J and Balents L 2015 Impurity-bound states and Green's function zeros as local signatures of topology *Phys. Rev. B* **92** 085126
[34] Maciejko J, Liu C, Oreg Y, Qi X-L, Wu C and Zhang S-C 2009 Kondo effect in the helical edge liquid of the quantum spin Hall state *Phys. Rev. Lett.* **102** 256803
[35] Goth F, Luitz D J and Assaad F F 2013 Magnetic impurities in the Kane–Mele model *Phys. Rev. B* **88** 075110
[36] Hu F M, Wehling T O, Gubernatis J E, Frauenheim T and Nieminen R M 2013 Magnetic impurity affected by spin–orbit coupling: Behavior near a topological phase transition *Phys. Rev. B* **88** 045106
[37] Liu Q, Liu C-X, Xu C, Qi X-L and Zhang S-C 2009 Magnetic impurities on the surface of a topological insulator *Phys. Rev. Lett.* **102** 156603
[38] Zyuzin A A and Loss D 2014 RKKY interaction on surfaces of topological insulators with superconducting proximity effect *Phys. Rev. B* **90** 125443
[39] Lee H-H, Liu J-Y, Chang C-R and Shen S-Q 2013 Impurity influence in quantum spin Hall transport *Phys. Rev. B* **88** 195149
[40] Black-Schaffer A M and Balatsky A V 2012 Strong potential impurities on the surface of a topological insulator *Phys. Rev. B* **85** 121103
[41] Sessi P *et al* 2016 Dual nature of magnetic dopants and competing trends in topological insulators *Nat. Commun.* **7** 12027
[42] Biswas R R and Balatsky A V 2010 Impurity-induced states on the surface of three-dimensional topological insulators *Phys. Rev. B* **81** 233405
[43] Black-Schaffer A M, Balatsky A V and Fransson J 2015 Filling of magnetic-impurity-induced gap in topological insulators by potential scattering *Phys. Rev. B* **91** 201411
[44] Nozières P and Pistolesi F 1999 From semiconductors to superconductors: a simple model for pseudogaps *Eur. Phys. J. B* **10** 649–62
[45] Loh Y L, Randeria M, Trivedi N, Chang C-C and Scalettar R 2016 Superconductor-insulator transition and Fermi-Bose crossovers *Phys. Rev. X* **6** 021029
[46] Yazdani A and Kapitulnik A 1995 Superconducting-insulating transition in two-dimensional *a*-MoGe thin films *Phys. Rev. Lett.* **74** 3037
[47] Caviglia A D, Gariglio S, Reyren N, Jaccard D, Schneider T, Gabay M, Thiel S, Hammerl G, Mannhart J and Triscone J-M 2008 Electric field control of the $LaAlO_3/SrTiO_3$ interface ground state *Nature* (*London*) **456** 624–7
[48] Kanoda K and Kato R 2011 Mott physics in organic conductors with triangular lattices *Annu. Rev. Condens. Matter Phys.* **2** 167–88
[49] Bollinger A T, Dubuis G, Yoon J, Pavuna D, Misewich J and Bozovic I 2011 Superconductor–insulator transition in

$La_{2-x}Sr_xCuO_4$ at the pair quantum resistance *Nature* (*London*) **472** 458–60
[50] Lado J L and Ferńendez-Rossier J 2016 Unconventional Yu-Shiba-Rusinov states in hydrogenated graphene *2D Mater.* **3** 025001
[51] Wehling T O, Dahal H P, Lichtenstein A I and Balatsky A V 2008 Local impurity effects in superconducting graphene *Phys. Rev. B* **78** 035414
[52] Sakurai A 1970 Comments on superconductors with magnetic impurities *Prog. Theor. Phys.* **44** 1472
[53] Pershoguba S S, Björnson K, Black-Schaffer A M and Balatsky A V 2015 Currents induced by magnetic impurities in superconductors with spin-orbit coupling *Phys. Rev. Lett.* **115** 116602
[54] Tetienne J-P, Dontschuk N, Broadway D A, Stacey A, Simpson D A and Hollenberg L C L 2017 Quantum imaging of current flow in graphene *Sci. Adv.* **3**
[55] Casola F, van der Sar T and Yacoby A 2018 Probing condensed matter physics with magnetometry based on nitrogen-vacancy centres in diamond *Nat. Rev. Mater.* **3** 17088
[56] Rodenbücher C, Bihlmayer G, Speier W, Kubacki J, Wojtyniak M, Rogala M, Wrana D, Krok F and Szot K 2018 Local surface conductivity of transition metal oxides mapped with true atomic resolution *Nanoscale* **10** 11498
[57] Yazyev O V and Helm L 2007 Defect-induced magnetism in graphene *Phys. Rev. B* **75** 125408
[58] Lopez-Bezanilla A and Lado J L 2019 Defect-induced magnetism and Yu-Shiba-Rusinov states in twisted bilayer graphene *Phys. Rev. Mater.* **3** 084003
[59] Bauer J, Oguri A and Hewson A C 2007 Spectral properties of locally correlated electrons in a Bardeen–Cooper–Schrieffer superconductor *J. Phys.: Condens. Matter* **19** 486211
[60] Liu C, Huang Y, Chen Y and Ting C S 2019 Temperature-dependent spectral function of a Kondo impurity in an *s*-wave superconductor *Phys. Rev. B* **99** 174502
[61] Wang R, Su W, Zhu J-X, Ting C S, Li H, Chen C, Wang B and Wang X 2019 Kondo signatures of a quantum magnetic impurity in topological superconductors *Phys. Rev. Lett.* **122** 087001

New Journal of Physics
The open access journal at the forefront of physics

Deutsche Physikalische Gesellschaft DPG
IOP Institute of Physics

Published in partnership with: Deutsche Physikalische Gesellschaft and the Institute of Physics

OPEN ACCESS

RECEIVED
5 August 2019

REVISED
22 November 2019

ACCEPTED FOR PUBLICATION
13 December 2019

PUBLISHED
20 January 2020

PAPER

Engineering nodal topological phases in Ising superconductors by magnetic superstructures

Szczepan Głodzik[1,3] **and Teemu Ojanen**[2]

[1] Institute of Physics, M. Curie-Skłodowska University, 20-031 Lublin, Poland
[2] Computational Physics Laboratory, Tampere University, PO Box 692, FI-33014 Tampere, Finland
[3] Author to whom any correspondence should be addressed.

E-mail: szglodzik@kft.umcs.lublin.pl **and** teemu.ojanen@tuni.fi

Keywords: nodal superconductors, topological superconductors, magnetic impurities

Abstract

Recently it was discovered that superconductivity in transition metal dichalcogenides (TMDs) is strongly affected by an out-of-plane spin–orbit coupling. In addition, new techniques of fabricating 2d ferromagnets on van der Waals materials are rapidly emerging. Combining these breakthroughs, we propose a realization of nodal topological superconductivity in TMDs by fabricating nanostructured ferromagnets with an in-plane magnetization on the top surface. The proposed procedure does not require application of external magnetic fields and applies to monolayer and multilayer (bulk) systems. The signatures of the topological phase include Majorana flat bandsthat can be directly observed by scanning tunneling microscopy techniques. We concentrate on $NbSe_2$ and argue that the proposed structures demonstrating the nodal topological phase can be realized within existing technology.

1. Introduction

According to the modern approach to condensed matter physics, novel states of matter can be realized in designer systems by combining simpler building blocks. This view implies that our access to new phases of matter and emergent quantum particles is ultimately limited only by our imagination and ability to manipulate matter. The designer approach to 1d topological superconductivity [1, 2] has stirred enormous activity, aiming to fabricate Majorana quasiparticles [3, 4] and harness them in applications. While most of the previous work has targeted gapped phases, here we propose fabrication of a 2d nodal phase with flat Majorana edge bands.

Our proposal is based on two recent breakthroughs, the observation of Ising superconductivity in transition metal dichalcogenides (TMDs) [5–12] and the discovery of novel techniques to fabricate 2d magnetic structures on van der Waals materials [13]. Due to the inversion-breaking structure of monolayers, the quasiparticles experience strong valley-dependent out-of-plane spin–orbit coupling (SOC). As a result, superconductivity exhibits remarkable robustness in the presence of large magnetic fields inducing a Zeeman splitting far exceeding the Pauli limit. The importance of the SOC in bulk 2H layer structures has been long overlooked probably because the bulk has inversion symmetry. While the stacked monolayers that make up the bulk exhibit staggered SOC that restores inversion symmetry as a whole, the layers are weakly coupled and quasiparticles in individual layers are subject to strong Ising SOC [14]. This is particularly interesting since the pioneering work by Kane and Mele [15] identified an Ising type SOC in graphene as a crucial ingredient of the quantum spin-Hall phase.

The rich electronic properties of TMDs have stimulated several proposals for topological and unconventional superconductivity [16–26]. In [27, 28] it was proposed that an Ising spin–orbit coupled monolayer TMD (e.g. $NbSe_2$) in the presence of an in-plane magnetic field could realize a topological superconducting state characterized by a nodal bulk and flat Majorana edge bands. In our work we consider how the state can be observed in magnetic structures fabricated on top of an Ising superconductor, treating $NbSe_2$ as a particular realization. We show how magnetic nanostructures on 2H-$NbSe_2$ give rise to the nodal topological

phase signaled by the appearance of flat Majorana edge bands. In the light of the ground-breaking success in fabricating 2d magnetic nanostructures on van der Waals materials, our design takes advantage of the latest advances and has several crucial advantages over the magnetic field induced phase [29–32]. Our setup does not only remove the necessity of external fields but, importantly, relaxes the requirement of manufacturing monolayer or few layer systems. The proposed topological state engineering works equally well for bulk systems since disruptive orbital effects arising from the in-plane magnetic fields are completely absent in our design. In multilayer systems the topological state is formed in the surface layer in the area in contact with the magnetic structure. The further advantages of the proposed setup include the possibility of fabricating well-defined nanostructures of topological elements. This comes with the benefit that the Majorana flat bands can be directly observed by scanning tunneling microscopy (STM) by studying the local density of states (LDOS) on magnetic islands. The STM measurements could be employed in resolving the spatial structure of the flat bands, thus providing a smoking-gun signature of the nodal topological phase. Considering that the process of growing magnetic islands on top of $NbSe_2$ systems is already experimentally on the way, we expect that our predictions will find experimental confirmation in the near future.

2. Model

As a particular model of a TMD we consider a tight-binding representation of 2H-$NbSe_2$. This layered structure consists of stacked units of Nb atoms on a triangular lattice sandwiched by Se layers. To study the appearance and the properties of the nodal topological phase, it is convenient to device a minimum phenomenological model that faithfully displays the essential features of a real material. Since the relevant bands near the Fermi energy mostly derive from Nb *d* orbitals, the band structure can be qualitatively reproduced by a model with one orbital per site on a triangular lattice. This approximation treats the system effectively as quasi-2d structure, neglecting the less important Se-derived 3d bands near the Γ point. While the tight-binding parameters and the band structure vary with the number of layers, the quasi-2d bands remain largely unchanged due to the weak interlayer coupling. Also, experimental observations of magnetic impurities in bulk 2H-$NbSe_2$ highlight the 2d nature of the magnetic subgap spectrum and the qualitative validity of treating the layers as effectively decoupled [33]. Thus, while our model is expected to be most faithful in monolayer systems, the experimental evidence suggests it can reasonably capture the qualitative behavior of the top layer in contact with the magnet in multilayer systems. In a recent experiment examining Shiba states of Fe impurities in NbSe2 ([34]), it was observed that the subgap energy of single magnetic impurity states may get modulated by the presence of the charge density wave (CDW). In the magnetic island structure we study (see figure 1 for a schematic view), similar effect could perhaps give rise to modulation of magnetically induced subgap bands with CDW periodicity. However, this is not expected to be crucial for the flat edge bands. The Hamiltonian on a triangular lattice with the zigzag edge parallel to the *x* direction can be written as $\hat{H} = \hat{H}_{\rm kin} + \hat{H}_{\rm SOC} + \hat{H}_M + \hat{H}_{\rm SC}$, where

$$\begin{aligned}
\hat{H}_{kin} &= -t \sum_{\langle \mathbf{i},\mathbf{j}\rangle,\sigma} c^{\dagger}_{\mathbf{i}\sigma} c_{\mathbf{j}\sigma} - \mu \sum_{\mathbf{i},\sigma} c^{\dagger}_{\mathbf{i}\sigma} c_{\mathbf{i}\sigma} - t_2 \sum_{\langle\langle \mathbf{i},\mathbf{j}\rangle\rangle,\sigma} c^{\dagger}_{\mathbf{i}\sigma} c_{\mathbf{j}\sigma},\\
\hat{H}_{SOC} &= -i\lambda \sum_{\langle \mathbf{i},\mathbf{j}\rangle,\sigma,\sigma'} e^{3i\theta_{\mathbf{ij}}} \sigma_z^{\sigma\sigma'} c^{\dagger}_{\mathbf{i}\sigma} c'_{\mathbf{j}\sigma},\\
\hat{H}_M &= -\sum_{\mathbf{i},\sigma,\sigma'} M_y(\mathbf{i}) \sigma_y^{\sigma,\sigma'} c^{\dagger}_{\mathbf{i}\sigma} c'_{\mathbf{i}\sigma},\\
\hat{H}_{SC} &= \sum_{\mathbf{i}} \Delta (c^{\dagger}_{\mathbf{i}\uparrow} c^{\dagger}_{\mathbf{i}\downarrow} + H.c.).
\end{aligned} \tag{1}$$

Symbols t and t_2 correspond to the nearest and next-nearest neighbor hopping and μ is the chemical potential. Additionally, λ parametrizes the out-of-plane Ising-type SOC, the magnetic material gives rise to magnetic splitting $\mathbf{M_y}$ and Δ describes the superconducting pairing. Pauli matrices σ act on the spin degrees of freedom. The symbols $\langle \mathbf{i}, \mathbf{j}\rangle$ and $\langle\langle \mathbf{i}, \mathbf{j}\rangle\rangle$ denote the summation over nearest and next-nearest neighbors respectively, $\theta_{\mathbf{ij}}$ is the angle the vector connecting **i** and **j** sites makes with the positive *x* axis (so that $e^{3i\theta_{\mathbf{ij}}} = \pm 1$).

The system is most conveniently analyzed by passing to momentum space and working in the Nambu basis $\psi = (c_{k\uparrow}, c_{k\downarrow}, c^{\dagger}_{k\uparrow}, c^{\dagger}_{k\downarrow})^T$ where the Bogoliubov–de Gennes Hamiltonian becomes

$$H = E_0(k)\tau_z + E_{\rm SO}(k)\sigma_z + M\sigma_y + \Delta\tau_y\sigma_y. \tag{2}$$

The additional set of Pauli matrices τ act in the particle–hole space. The normal and spin–orbit hopping terms are given by

$$E_0(k) = -2t\left[\cos(k_x a) + 2\cos\left(\frac{k_x a}{2}\right)\cos\left(\frac{k_y a\sqrt{3}}{2}\right)\right] - 2t_2\left[\cos(k_y\sqrt{3}\,a) + 2\cos\left(\frac{k_x 3a}{2}\right)\cos\left(\frac{k_y\sqrt{3}\,a}{2}\right)\right] - \mu$$

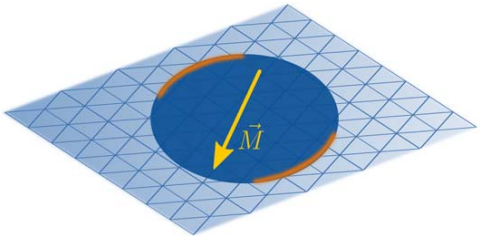

Figure 1. Schematic view of the studied system. A magnetic island with in-plane polarization (blue circle) on a top surface of $NbSe_2$ structure. Triangular lattice sites indicate the positions of Nb atoms. The in-plane TMD structure determines the positions of the flat bands. This is independent on the magnetization direction.

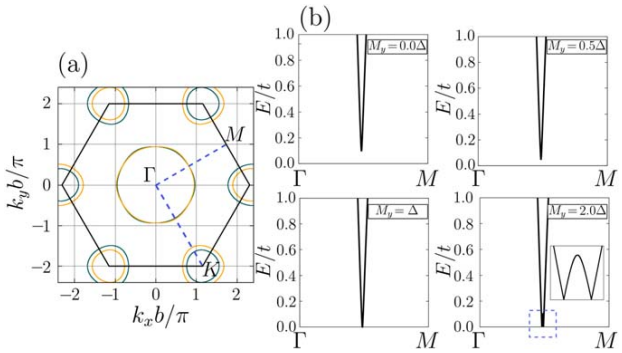

Figure 2. Momentum space characteristics of a monolayer TMD. (a) Fermi surface and the Brillouin zone with high symmetry directions as dashed purple lines. Parameters used: $t_2 = t, \mu = -0.8t, \lambda = 0.1t$ and $b = \sqrt{3}\,a$, where a is the lattice constant. (b) The evolution of point nodes along a high symmetry Γ–M line in the superconducting state with the values of Zeeman field in inset boxes. Same parameters as (a) but with $\Delta = 0.1t$. The inset in the last panel shows a close-up of the purple dashed box.

and

$$E_{\mathrm{SO}}(k) = 2\lambda\left[\sin(k_x a) - \sin\left(\frac{k_x a}{2} - \frac{k_y\sqrt{3}\,a}{2}\right) - \sin\left(\frac{k_x a}{2} + \frac{k_y\sqrt{3}\,a}{2}\right)\right]. \tag{3}$$

Diagonalization of the Hamiltonian reveals four energy bands:

$$E^2 = E_0^2 + E_{\mathrm{SO}}^2 + M^2 + \Delta^2 \pm 2\sqrt{E_0^2(E_{\mathrm{SO}}^2 + M^2) + M^2\Delta^2}. \tag{4}$$

In the next section we show how the essential normal state features of $NbSe_2$ as well as the nodal topological superconducting state emerge from this model.

3. Nodal topological superconductivity and flat edge bands

3.1. Normal state properties

To model the system in the normal state without magnetization, we first set $M = \Delta = 0$ and plot the Fermi surface in figure 2, for a set of parameters that qualitatively reproduces the numerically calculated and experimentally resolved band-structure of $NbSe_2$ [14, 35]. We observe the spin–orbit split Γ pocket and more visibly split pockets around K and K' points. Within the second-neighbor hopping model that we use, we are also able to resolve a slight trigonal warping of the pockets. The SOC polarizes the electron spins at K and K' points in the opposite out-of-plane directions. The splitting vanishes along Γ–M that define mirror symmetric lines. Note that in a multilayer system the spin–orbit coupling is staggered and λ has opposite sign in adjacent layers. Nevertheless, the top layer relevant for the topological nodal state in multilayer systems will experience a strong Ising SOC just as a monolayer system.

3.2. Nodal topological state

In the presence of superconductivity and magnetization the spectrum is given by equation (4). The spectrum is symmetric with respect to zero energy and branches with the minus sign in front of the square root will determine the properties near Fermi energy. For $\Delta > M$ the system is fully gapped while for $M \geqslant \Delta$ the system

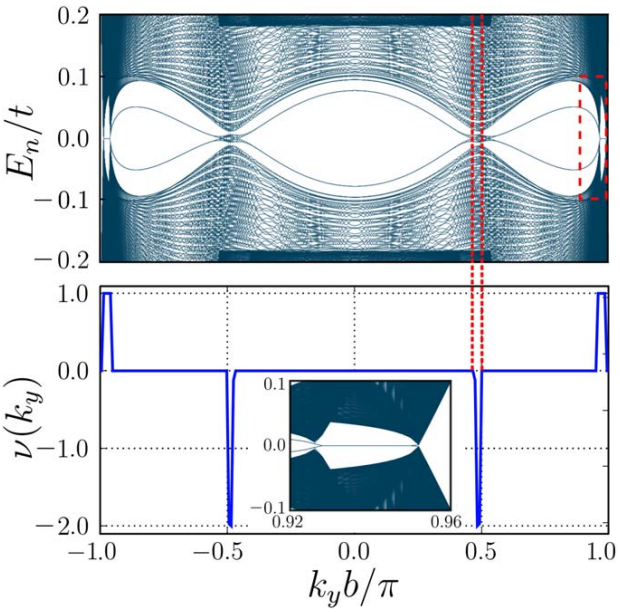

Figure 3. Results in the infinite strip geometry. Top panel: $E(k_y)$ spectrum of the nanoribbon. The number of atoms parallel to the zigzag direction $N = 4001$. The red dashed line marks the range of k_y for which we expect a flat band to form. Bottom panel: winding number equation (5). The inset shows a close-up of the red dashed box. Parameters used: $t_2 = t, \mu = -0.8t, \lambda = 0.1t, \Delta = 0.1t$, $M_y = 2\Delta$.

becomes gapless with isolated nodal points k_0 satisfying $E(k_0) = 0$. From the dispersion (4) we can calculate that at $M = \Delta$ a pair of nodes (with opposite winding) nucleate on the crossing point of the Fermi surface and the Γ–M lines. This will give rise to six pairs of nodes in the Brillouin zone. By increasing M the nodes of opposite winding move away from the Fermi surface along the Γ–M lines. This evolution of the nodes is presented in figure 2(b). The nodes cannot be gapped out by small lattice-symmetric perturbations, hinting to a topological nature of the phase. The topological character will be made more explicit below when we discuss the appearance of the flat edge bands.

In analogy to the Fermi arc surface states that connect the surface projections of bulk band-touching points in topological semimetals, the 2d nodal phase supports edge states that connect the edge projections of the nodes. Due to superconductivity, the edge states in the studied system have a Majorana character. The dispersion of the edge bands is flat and the bands appear on edge terminations for which the projections of the nodes with opposite winding do not cancel. Atomic positions on a single layer of $NbSe_2$ form a hexagonal lattice with triangular Nb and Se sublattices. The flat band is the most prominent for an armchair edge termination while it shrinks to a point for a zigzag edge. In order to probe the flat bands, we envision the studied system in an infinite ribbon geometry. We assume periodic boundary conditions (PBCs) in y direction, yielding a flat band with maximal extension. So obtained strip spectrum $E(k_y)$ is presented in the top panel of figure 3. The large mismatch of the relevant energy scales $\Delta \sim 0.01t$ would require considering system sizes that are impractical for numerical calculations. Therefore we employ exaggerated parameters $\Delta \sim 0.1t$ for real-space calculations. However, below we argue that the flat bands remain well-defined even for realistic parameters (see figure 6). Close to the nanoribbon BZ edge we see a perfectly flat band at zero energy which connects the nodes. Closer to $k_y b/\pi \simeq \pm 0.5$, there exists another flat band connecting opposite nodes. For the employed parameters, the gap between the bulk states and the edge band is much smaller and the states are less localized to the edge. As a result, the flat band exhibits oscillating departures from the gap center. As shown below, the direct evaluation of the topological invariant protecting the flat band confirms that the inner edge bands exhibit perfect flatness in the large system limit.

To elucidate the topological nature of the nodal phase, we calculate the topological invariant protecting the flat bands. This will also provide a definite connection between the edge bands and the edge projection of the nodes. The Hamiltonian (2) anticommutes with matrix $\mathcal{C} = \tau_y \sigma_x$, hence it belongs to the class BDI, and can be characterized by the winding number in odd spatial dimensions. In a strip geometry we can Fourier transform the 2d tight-binding Hamiltonian in y direction. Thus, the resulting partially transformed Hamiltonian describes hopping in a 1d chain perpendicular to the strip while k_y is regarded as a parameter. For some intervals of k_y the 1d Hamiltonian is topologically non-trivial and the 1d chain hosts end states. The flat band can be regarded as the union of the end states of the 1d Hamiltonian. The winding number as a function of k_y can be

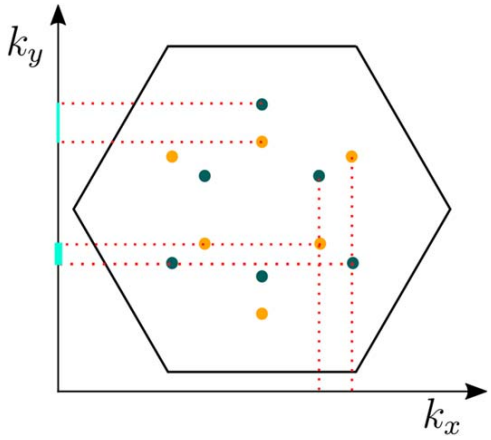

Figure 4. Flat bands are formed between edge projections of nodes with opposite chirality. The edge parallel to y direction supports four edge bands (two shown) with maximal extension. The band that connects the projections of two pairs of nodes is doubly degenerate. On the edge parallel to x axis the opposite nodes project on top of each other and the flat band vanishes.

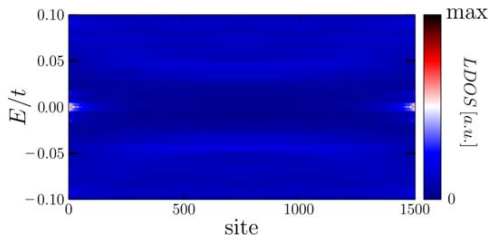

Figure 5. The local density of states w.r. to the energy E and the site index in the nanoribbon geometry. Parameters same as in figure 3, expect for $\Delta = 0.3t$.

obtained by evaluating the invariant [36]

$$\nu(k_y) = \frac{1}{2\pi \mathrm{i}} \int_{-2\pi}^{2\pi} \mathrm{d}k_x \, \mathrm{Tr}[\tau_y \sigma_x H^{-1} \partial_{k_x} H], \tag{5}$$

and is illustrated for the studied model in the bottom panel of figure 3. We can see that close to the ribbon BZ edge, where there is a visible flat band, the value of the invariant is $\nu(k_y) = 1$. There is also an interval of non-trivial momenta around $k_y b/\pi = 0.5$, with higher value of the topological invariant $\nu(k_y) = -2$. The different signs and values of the winding number come from the addition of nodes when projecting them onto the k_y direction as depicted in figure 4. Physically this means that the flat band is doubly degenerate when $|\nu(k_y)| = 2$. Close to the BZ edge, one pair of nodes adds up and the invariant is equal to unity. The mid-gap bands close to the middle of the BZ that suffer from the proximity of the bulk bands, coincide with invariant value $\nu(k_y) = -2$. Thus they are unambiguously identified as flat bands in the large system limit.

To see that the flat bands are indeed localized at the edges of the nanoribbon, we calculated the LDOS as a function of energy and the site index in the direction perpendicular to the PBC

$$A(\mathbf{i}, E) = \sum_{k_y, n, \sigma} [|u_{\mathbf{i}n\sigma}(k_y)|^2 \delta(E - E_n(k_y) + |v_{\mathbf{i}n\sigma}(k_y)|^2 \delta(E + E_n(k_y)], \tag{6}$$

where we sum over all values of momentum, every state n and both spin directions $\sigma = \uparrow, \downarrow$. The Dirac functions are approximated by Lorentzians with broadening $0.001t$. The result presented in figure 5 shows a strong enhancement of the zero-energy LDOS at the edges of the strip.

3.3. Nodal phase on magnetic islands

The most direct link between our theory and experiments is probably provided by TMD systems with magnetic islands grown on top. These systems, expected to display rich interplay of competing orders, are currently becoming accessible in experiments. The study of coexistence of superconductivity and magnetization has a long history. A single magnetic impurity induces a pair of bound states in the superconducting energy gap. Their shape in real space reflects the symmetry of the underlying lattice, and can extend far away from the impurity

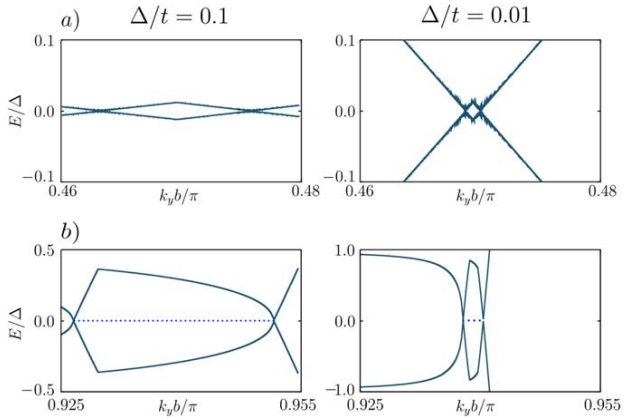

Figure 6. Evolution of the point nodes (crossing points) and low-lying spectrum for different values of Δ/t. (a) 'Inner' nodes (b) 'outer', close to the Brillouin zone edge nodes. Dotted lines in (b) denote the position of flat bands in a finite system. While the length of the flat band is diminished, the gap to the bulk states remains significant.

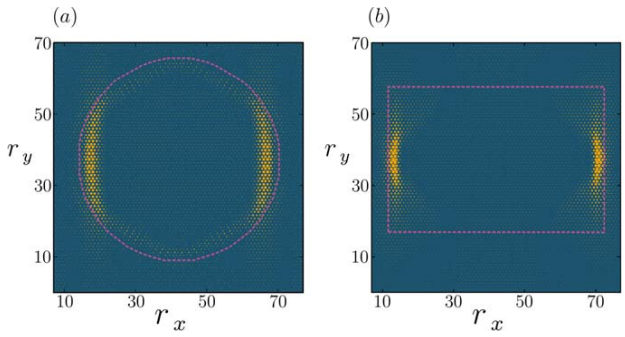

Figure 7. Local density of states integrated over the two lowest-lying states, expressed as the size of the yellow dots. Dashed lines outline the shapes of magnetic islands. Parameters used: $t_2 = t, \mu = -0.8, \lambda = 0.1t, \Delta = 0.3t, M_y = 2\Delta$.

depending on the dimensionality of the substrate and other factors like e.g. spin–orbit interaction [33, 37]. In the case of a collection of impurities, a Shiba band forms which can undergo a topological phase transition in the deep-dilute limit. Such two-dimensional islands of magnetic impurities are recently receiving much attention in extensive theoretical and experimental studies [38–41], with proposals of engineering hybrids with different dimensionality [42]. In this context, the present work turns a new leaf on topological state engineering through magnetization, generalizing the previous efforts to obtain gapless topological phases.

For real space calculations we have constructed a triangular lattice consisting of 85×86 atomic sites and applied PBCs in both directions. Then we have applied Zeeman field pointing in the y direction on a collection of sites that comprise the magnetic island. Our approach of fully diagonalizing the lattice model is laden with high computational cost, hence the limited finite size of the lattice. Due to the finite size limitations, the flat band physics can be properly resolved only for the two lowest-lying (closest to zero energy) states, and for the toy parameters, in which the superconducting energy gap is strongly exaggerated ($\Delta \sim t$). However, this is sufficient to demonstrate qualitatively the effects of the nodal phase. To demonstrate that we show in figure 6 how the low-lying spectrum between the nodal points evolve as values of Δ/t are decreasing. One can see that the distance from the gap center to the bulk bands is approximately the same for different values of Δ, and for the outer nodes its value remains a significant fraction of the superconducting gap. This means that the flat bands are always clearly resolved from the bulk states and that the calculations with exaggerated Δ/t values do not qualitatively change the results. The summed LDOS of the low-energy states is shown in figure 7. In panel (a) we assumed a circular shape of the magnetic island with radius $r = 28a$ from the center of the lattice, whereas in (b) the island has a rectangular shape of the size $60a \times 40a$, where a is the lattice constant, assumed to be equal to unity. The number of atomic sites comprising the island region is approximately equal in both geometries. The underlying lattice is periodic in every direction, hence the edge of the island is the only edge in our system. The nodal topological phase emerges only when there is an in-plane magnetization, so the edge of the island is the

boundary between a gapped trivial phase and the nodal topological phase. Because of the structure of point nodes (as explained in section 3.2) and their mutual annulment in the k_x projection, the edge states will never appear in parallel to x direction. We observe that indeed, regardless of the shape of the magnetic island, localized Majorana modes appear only on the edges parallel to y direction. As stressed above, a quantitative study of the edge bands in real space comes with substantial computational cost and is beyond the scope of the present work.

3.4. Note on the Rashba effect

In general, monolayer systems on a substrate and surfaces of a bulk system break the mirror symmetry perpendicular to layers. Therefore a Rashba-type spin–orbit coupling may be non-zero. The Rashba effect, giving rise to an in-plane spin–orbit field, has adversarial effect on the nodal state as it generally gaps out the nodes. The Rashba contribution to equation (2) can be implemented through the nearest-neighbor hopping term

$$H_{\mathrm{R}} = E_{\mathrm{R}_x}(k)\sigma_x + E_{\mathrm{R}_y}(k)\tau_z\sigma_y, \tag{7}$$

with

$$E_{\mathrm{R}_x}(k) = \alpha_{\mathrm{R}}\sqrt{3}\,\sin\left(\frac{k_y a\sqrt{3}}{2}\right)\cos\left(\frac{k_x a}{2}\right),$$
$$E_{\mathrm{R}_y}(k) = -\alpha_{\mathrm{R}}\left(\sin(k_x a) + \sin\left(\frac{k_x a}{2}\right)\cos\left(\frac{k_y a\sqrt{3}}{2}\right)\right),$$

where α_{R} is the Rashba constant. As can be easily verified, the chiral symmetry protecting the edge band is broken and a strict topological protection is not realized. Unlike time-reversal symmetry (which is always present in the absence of magnetism) and particle-hole symmetry (which is exact for superconducting systems), chiral symmetry typically requires some degree of tuning of external conditions. A typical example is the direction of magnetic field. For some field orientations the system exhibits chiral symmetry while for other this does not hold. Since some degree of disorder is almost unavoidable in solid state systems, chiral symmetry is typically only approximate. However, the magnitude of breaking of this symmetry is important in assessing how detrimental it is for the observability of the edge modes. A small symmetry-breaking perturbation pushes the edge modes away from the zero energy and they acquire a weak dispersion, but they are still present. In contrast to the Ising SOC which is determined by the lattice structure of TMDs, the Rashba SOC is case specific. Therefore it can also be very weak, especially in multilayer systems where ripples do not play a role.

4. Discussion and outlook

The physical realization of the proposed system could be a multilayer or monolayer TMD in contact with magnetic insulating material grown on top. The material should support in-plane magnetization and not perturb the system significantly. A 2d magnetic insulator with a high-quality contact to TMD would be ideal for this purpose. In fact, the requirement to be an insulator is inconsequential since proximity effect can make a thin magnet superconducting. The recent breakthroughs in fabricating 2d magnets down to monolayer thickness on van der Waals systems provide a promising avenue for our proposal [13, 29–32]. An interesting candidate for the ferromagnet is VSe_2 which is a TMD itself and can be epitaxially grown on $NbSe_2$ and other systems of interest. Furthermore, it has been observed that structures based on VSe_2 layers exhibit an in-plane magnetization on different substrates [31]. Considering the emerging nature and rapid development of the field of 2d magnets, increasing number of material candidates are likely to emerge soon. In practice the magnetic material also induces a non-magnetic potential which could shift the chemical potential of substrate and thus change the Fermi surface. However, the precise filling is not crucial for realization of the nodal phase. It seems plausible that in the recent experiment [43] the magnetism in the system was not sufficiently homogeneous or that it is significant only near the edges of the VSe_2 islands. While the first experimental result does not seem to exhibit the signatures of the flat band, it is quite possible that further development in the sample fabrication and experimental methods could yield the desired result.

The nodal phase can be experimentally identified by observing the Majorana flat bands. As discussed above, the flat bands give rise to enhanced zero-energy LDOS on certain edge terminations on the island. An ideal probe to access this information is STM. In principle, the surface LDOS can be directly measured as a function of energy. This would resolve the flat bands in space and energy. As long as the in-plane magnetization is sufficiently strong to drive islands to the nodal phase, the flat band is most pronounced and suppressed in the same spatial directions for all islands irrespective of the direction of their magnetization. Observation of an enhanced zero energy LDOS on edges with common tangent for multiple islands would constitute a smoking evidence on the nodal phase.

In the present work we employed $NbSe_2$ as a candidate material for the topological state engineering. However, for the existence of the nodal phase the crucial features are the (quasi-)2d nature of the system, the Ising SOC within a layer, superconductivity and in-plane magnetization. Thus we expect that other TMDs would also provide promising candidates for the proposed system.

In summary, we proposed transition metal dichalcogenides with ferromagnetic structure on top as promising candidates to realize nodal topological superconductivity and flat Majorana edge bands. The systems could be fabricated and analyzed within existing experimental techniques.

Acknowledgments

This work was supported by National Science Centre (NCN, Poland) grant 2017/27/N/ST3/01762 (SG). We would like to thank Peter Liljeroth for initial stimulus of the project and for the numerous discussions regarding experimental realizations. We also acknowledge fruitful discussions with Tadeusz Domański.

ORCID iDs

Szczepan Głodzik https://orcid.org/0000-0001-7928-9959

References

[1] Oreg Y, Refael G and von Oppen F 2010 Helical liquids and Majorana bound states in quantum wires *Phys. Rev. Lett.* **105** 177002
[2] Lutchyn R M, Sau J D and Sarma S D 2010 Majorana fermions and a topological phase transition in semiconductor-superconductor heterostructures *Phys. Rev. Lett.* **105** 077001
[3] Mourik V, Zuo K, Frolov S M, Plissard S R, Bakkers E P A M and Kouwenhoven L P 2012 Signatures of Majorana fermions in hybrid superconductor–semiconductor nanowire devices *Science* **336** 1003–7
[4] Das A, Ronen Y, Most Y, Oreg Y, Heiblum M and Shtrikman H 2012 Zero-bias peaks and splitting in an Al–InAs nanowire topological superconductor as a signature of Majorana fermions *Nat. Phys.* **8** 887
[5] Saito Y *et al* 2015 Superconductivity protected by spin-valley locking in ion-gated MoS_2 *Nat. Phys.* **12** 144
[6] Xi X, Wang Z, Zhao W, Park J-H, Law K T, Berger H, Forró L, Shan J and Mak K F 2015 Ising pairing in superconducting $NbSe_2$ atomic layers *Nat. Phys.* **12** 139
[7] Xi X, Berger H, Forró L, Shan J and Mak K F 2016 Gate tuning of electronic phase transitions in two-dimensional $NbSe_2$ atomic layers *Phys. Rev. Lett.* **117** 106801
[8] Lu J M, Zheliuk O, Leermakers I, Yuan N F Q, Zeitler U, Law K T and Ye J T 2015 Evidence for two-dimensional Ising superconductivity in gated MoS_2 *Science* **350** 1353–7
[9] Navarro-Moratalla E *et al* 2016 Enhanced superconductivity in atomically thin TaS_2 *Nat. Commun.* **7** 11043
[10] Huang C *et al* 2018 Inducing strong superconductivity in WTe_2 by a proximity effect *ACS Nano* **12** 7185–96
[11] de la Barrera S C *et al* 2018 Tuning Ising superconductivity with layer and spin–orbit coupling in two-dimensional transition-metal dichalcogenides *Nat. Commun.* **9** 1427
[12] Sohn E *et al* 2018 An unusual continuous paramagnetic-limited superconducting phase transition in 2d $NbSe_2$ *Nat. Mater.* **17** 504–8
[13] Shabbir B, Nadeem M, Dai Z, Fuhrer M S, Xue Q-K, Wang X and Bao Q 2018 Long range intrinsic ferromagnetism in two dimensional materials and dissipationless future technologies *Appl. Phys. Rev.* **5** 041105
[14] Bawden L *et al* 2016 Spin-valley locking in the normal state of a transition-metal dichalcogenide superconductor *Nat. Commun.* **7** 11711
[15] Kane C L and Mele E J 2005 Quantum spin Hall effect in graphene *Phys. Rev. Lett.* **95** 226801
[16] Zhou B T, Yuan N F Q, Jiang H-L and Law K T 2016 Ising superconductivity and Majorana fermions in transition-metal dichalcogenides *Phys. Rev.* B **93** 180501
[17] Shaffer D, Kang J, Burnell F J and Fernandes R M 2019 Crystalline nodal topological superconductivity in monolayer $NbSe_2$ arXiv:1904.05470
[18] Yuan N F Q, Mak K F and Law K T 2014 Possible topological superconducting phases of MoS_2 *Phys. Rev. Lett.* **113** 097001
[19] Hsu Y-T, Vaezi A, Fischer M H and Kim E-A 2017 Topological superconductivity in monolayer transition metal dichalcogenides *Nat. Commun.* **8** 14985
[20] Fischer M H, Sigrist M and Agterberg D F 2018 Superconductivity without inversion and time-reversal symmetries *Phys. Rev. Lett.* **121** 157003
[21] Taniguchi K, Matsumoto A, Shimotani H and Takagi H 2012 Electric-field-induced superconductivity at 9.4 K in a layered transition metal disulphide MoS_2 *Appl. Phys. Lett.* **101** 042603
[22] Oiwa R, Yanagi Y and Kusunose H 2018 Theory of superconductivity in hole-doped monolayer MoS_2 *Phys. Rev.* B **98** 064509
[23] Möckli D and Khodas M 2018 Robust parity-mixed superconductivity in disordered monolayer transition metal dichalcogenides *Phys. Rev.* B **98** 144518
[24] Sosenko E, Zhang J and Aji V 2017 Unconventional superconductivity and anomalous response in hole-doped transition metal dichalcogenides *Phys. Rev.* B **95** 144508
[25] Liu C-X 2017 Unconventional superconductivity in bilayer transition metal dichalcogenides *Phys. Rev. Lett.* **118** 087001
[26] Chen W and An J 2019 *Phys. Rev.* B **100** 054503
[27] He W-Y, Zhou B T, He J J, Yuan N F Q, Zhang T and Law K T 2018 Magnetic field driven nodal topological superconductivity in monolayer transition metal dichalcogenides *Commun. Phys.* **1** 40
[28] Wang L, Rosdahl T O and Sticlet D 2018 Platform for nodal topological superconductors in monolayer molybdenum dichalcogenides *Phys. Rev.* B **98** 205411

[29] O'Hara D J *et al* 2018 Room temperature intrinsic ferromagnetism in epitaxial manganese selenide films in the monolayer limit *Nano Lett.* **18** 3125–31
[30] Gong C *et al* 2017 Discovery of intrinsic ferromagnetism in two-dimensional van der Waals crystals *Nature* **546** 265
[31] Bonilla M, Kolekar S, Ma Y, Diaz H C, Kalappattil V, Das R, Eggers T, Gutierrez H R, Phan M-H and Batzill M 2018 Strong room-temperature ferromagnetism in VSe_2 monolayers on van der Waals substrates *Nat. Nanotechnol.* **13** 289–93
[32] Huang B *et al* 2017 Layer-dependent ferromagnetism in a van der Waals crystal down to the monolayer limit *Nature* **546** 270
[33] Ménard G C *et al* 2015 Coherent long-range magnetic bound states in a superconductor *Nat. Phys.* **11** 1013
[34] Liebhaber E, Gonzalez S A, Baba R, Reecht G, Heinrich B W, Rohlf S, Rossnagel K, von Oppen F and Franke K J 2019 Yu–Shiba–Rusinov states in the charge-density modulated superconductor $NbSe_2$ arXiv:1903.09663 [condmat.mes-hall]
[35] Wijayaratne K, Zhao J, Malliakas C, Chung D Y, Kanatzidis bc M G and Chatterjee U 2017 Spectroscopic signature of moment-dependent electron-phonon coupling in 2H-TaS_2 *J. Mater. Chem.* C **5** 11310
[36] Volovik G E 2009 *The Universe in a Helium Droplet* (International Series of Monographs on Physics) (Oxford: Oxford University Press)
[37] Ptok A, Głodzik S and Domański T 2017 Yu–Shiba–Rusinov states of impurities in a triangular lattice of $NbSe_2$ with spin–orbit coupling *Phys. Rev.* B **96** 184425
[38] Röntynen J and Ojanen T 2015 Topological superconductivity and high Chern numbers in 2d ferromagnetic Shiba lattices *Phys. Rev. Lett.* **114** 236803
[39] Röntynen J and Ojanen T 2016 Chern mosaic: topology of chiral superconductivity on ferromagnetic adatom lattices *Phys. Rev.* B **93** 094521
[40] Palacio-Morales A, Mascot E, Cocklin S, Kim H, Rachel S, Morr D K and Wiesendanger R 2019 Atomic-scale interface engineering of Majorana edge modes in a 2d magnet-superconductor hybrid system *Sci. Adv.* **5** eaav6600
[41] Ménard G C, Guissart S, Brun C, Leriche R T, Trif M, Debontridder F, Demaille D, Roditchev D, Simon P and Cren T 2017 Two-dimensional topological superconductivity in Pb/Co/Si(111) *Nat. Commun.* **8** 2040
[42] Kobialka A, Domanski T and Ptok A 2019 Delocalisation of Majorana quasiparticles in plaquette-nanowire hybrid system *Sci. Rep.* **9** 12933
[43] Kezilebieke S *et al* 2019 Electronic and magnetic characterization of epitaxial VSe_2 monolayers on superconducting $NbSe_2$ arXiv:1909.10208 [cond-mat.mtrlsci]

Topological superconductivity in a designer ferromagnet-superconductor van der Waals heterostructure

Shawulienu Kezilebieke,[1,*] Md Nurul Huda,[1] Viliam Vaňo,[1] Markus Aapro,[1] Somesh C. Ganguli,[1] Orlando J. Silveira,[1] Szczepan Głodzik,[2] Adam S. Foster,[1,3] Teemu Ojanen,[4,5,*] and Peter Liljeroth[1,*]

[1]*Department of Applied Physics, Aalto University School of Science, PO Box 15100, 00076 Aalto, Finland*

[2]*Institute of Physics, M. Curie-Skłodowska University, 20-031 Lublin, Poland*

[34]*WPI Nano Life Science Institute (WPI-NanoLSI), Kanazawa University, Kakuma-machi, Kanazawa 920-1192, Japan*

[4]*Computational Physics Laboratory, Physics Unit, Faculty of Engineering and Natural, Sciences, Tampere University, PO Box 692, FI-33014 Tampere, Finland*

[5]*Helsinki Institute of Physics PO Box 64, FI-00014, Finland*

(Dated: February 11, 2020)

Abstract

The designer approach has become a new paradigm in accessing novel quantum phases of matter. Moreover, the realization of exotic states such as topological insulators, superconductors and quantum spin liquids often poses challenging or even contradictory demands for any single material. For example, it is presently unclear if topological superconductivity, which has been suggested as a key ingredient for topological quantum computing, exists at all in any naturally occurring material. This problem can be circumvented by using designer heterostructures combining different materials, where the desired physics emerges from the engineered interactions between the different components. Here, we employ the designer approach to demonstrate two major breakthroughs – the fabrication of van der Waals (vdW) heterostructures combining 2D ferromagnetism with superconductivity and the observation of 2D topological superconductivity. We use molecular-beam epitaxy (MBE) to grow two-dimensional islands of ferromagnetic chromium tribromide ($CrBr_3$) on superconducting niobium diselenide ($NbSe_2$) and demonstrate the existence of the one-dimensional Majorana edge modes using low-temperature scanning tunneling microscopy (STM) and spectroscopy (STS). The fabricated two-dimensional vdW heterostructure provides a high-quality controllable platform for electronic devices harnessing topological superconductivity.

There has been a surge of interest in designer materials that would realize electronic responses not found in naturally occurring materials[1–7]. Topological superconductors are one of the main targets of these efforts and they are currently attracting intense attention due to their potential as building blocks for Majorana-based qubits for topological quantum computation[7–9]. Majorana zero-energy modes (MZM) have been reported in several different experimental platforms, with the most prominent examples being semiconductor nanowires with strong spin-orbit coupling and ferromagnetic atomic chains proximitized with an s-wave superconductor[7,9–14]. It is also possible to realize MZMs in vortex cores on a proximitized topological insulator surface[15–17] or on $FeTe_{0.55}Se_{0.45}$ superconductor surface[18,19]. In these cases the MZM were spectroscopically identified as zero energy conductance signals that are localized at the ends of the one dimensional (1D) chain or in the vortex core. In two-dimensional systems, 1D dispersive chiral Majorana fermions are expected to localize near the edge of the system (Fig. 1A). For example, it was proposed that the dispersing Majorana states can be created at the edges of an island of magnetic adatoms on the surface of an s-wave superconductor[20–22]. Experimentally, promising signatures of such 1D chiral Majorana modes have recently been reported around nanoscale magnetic islands either buried below a single atomic layer of Pb[23], or adsorbed on a Re substrate[24], and in domain walls in $FeTe_{0.55}Se_{0.45}$[25]. However, these types of systems can be sensitive to disorder and may require interface engineering through, *e.g.*, the use of an atomically thin separation layer. In addition, it is difficult to incorporate these materials into device structures. These problems can be circumvented in van der Waals (vdW) heterostructures, where the different layers interact only through vdW forces[1]. VdW heterostructures naturally allow for very high quality interfaces and a multitude of practical devices have been demonstrated. While vdW materials with a wide range of properties have been discovered, ferromagnetism has been notably absent until recent discoveries of atomically thin $Cr_2Ge_2Te_6$[26], CrI_3[27] and $CrBr_3$[28,29]. The first reports relied on mechanical exfoliation for the sample preparation, but $CrBr_3$[30] and Fe_3GeTe_2[31] have also been grown using molecular-beam epitaxy (MBE) in ultra-high vacuum (UHV). This is essential for realizing clean edges and interfaces.

Among the various known vdW materials, the recently discovered monolayer ferromagnet transition metal trihalides combined with transition metal dichalcogenide (TMD) superconductors form an ideal platform for realizing 2D topological superconductivity (Fig. 1A). Here, we use MBE to grow high-quality monolayer ferromagnet $CrBr_3$ on a $NbSe_2$ super-

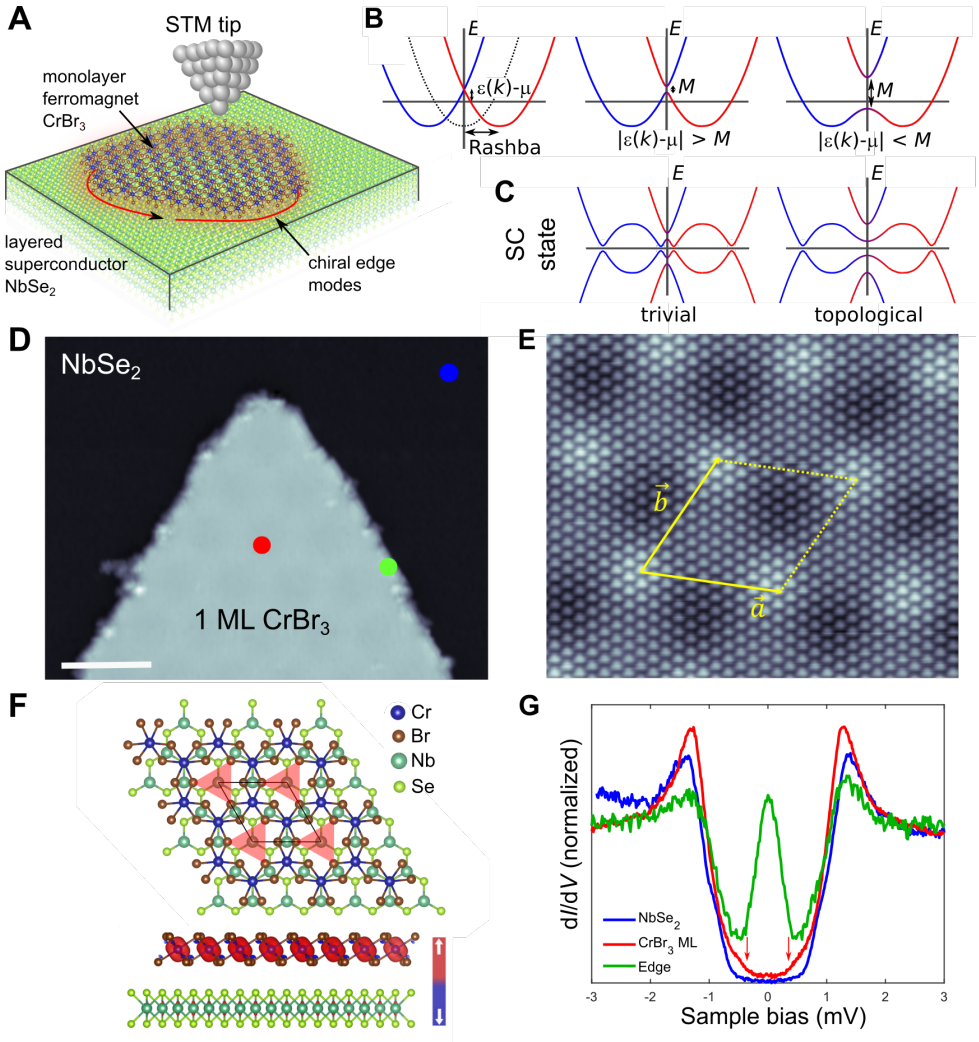

FIG. 1. **Realization of topological superconductivity in $CrBr_3$-$NbSe_2$ heterostructures.** (**A**) Schematic of the experimental setup. (**B,C**) Schematic of the bandstructure engineering to realize topological superconductivity. Effect of adding spin-orbit interactions and weaker and stronger Zeeman-type magnetization on the low-energy band structure in the normal (B) and superconducting states (C). (**D**) STM image of a monolayer thick $CrBr_3$ island grown on $NbSe_2$ using MBE (STM feedback parameters: $V_{\text{bias}} = +1$ V, $I = 10$ pA, scale bar: 10 nm). (**E**) Atomically resolved image on the $CrBr_3$ layer (STM feedback parameters: $V_{\text{bias}} = +1.7$ V, $I = 0.5$ nA, image size: 19×19 nm^2). (**F**) Calculated structure and the induced spin-polarization from density-functional theory calculations. (**G**) Experimental $\mathrm{d}I/\mathrm{d}V$ spectroscopy on the $NbSe_2$ substrate (blue), the middle of the $CrBr_3$ island (red) and at the edge of the $CrBr_3$ island (green) measured at $T = 350$ mK.

conducting substrate. The mirror symmetry is broken at the interface between the different materials and this lifts the spin degeneracy due to the Rashba effect. Therefore, we have all the necessary ingredients – magnetism, superconductivity and Rashba spin-orbit coupling – required to realize a designer topological superconductor[32,33]. We demonstrate the existence of the one-dimensional Majorana edge modes using low-temperature scanning tunneling microscopy (STM) and spectroscopy (STS). Realizing topological superconductivity in a van der Waals heterostructure has significant advantages compared to the other possible platforms: vdW heterostructures can potentially be manufactured by simple mechanical exfoliation, the interfaces are naturally very uniform and of high quality, and the structures can be straightforwardly integrated in device structures. Finally, layered heterostructures can be readily accessed by a large variety of external stimuli making external control of 2D topological superconductivity potentially possible by electrical[34], mechanical[35], chemical[36], and optical approaches[29].

Pioneering theoretical works[32,33] demonstrated that topological superconductivity may arise from a combination of out-of-plane ferromagnetism, superconductivity and Rashba-type spin-orbit coupling, as illustrated in Fig. 1B,C. In this scheme, the Rashba coupling lifts the spin-degeneracy of the conduction band while Zeeman splitting due to proximity magnetization lifts the remaining Kramers degeneracy. Adding superconductivity creates a particle-hole symmetric band structure and the superconducting pairing opens gaps at the Fermi energy. In our theoretical model for magnetically covered $NbSe_2$, a similar picture arises for the real band structure around any of the high symmetry points of the hexagonal Brillouin zone (Γ, K, or M) where Rashba coupling vanishes. Depending on the magnitude of the magnetization induced gap M and the position of the Fermi energy μ, the system enters a topological phase when $|\epsilon(\vec{k_0}) - \mu| \leq M$, where $\epsilon(\vec{k_0})$ is the energy of the band crossing at the high symmetry point in the absence of magnetization. This is due to the created effective p-wave pairing symmetry. The power of the designer approach with vdW heterostructures comes from the fact that the different components retain their intrinsic properties allowing for rational design of emergent quantum phases of matter and realizing schemes such as shown in Fig. 1B,C.

In Fig. 1D, we show a constant-current STM image of the $CrBr_3$ island grown on a freshly cleaved bulk $NbSe_2$ substrate by MBE (details of sample growth and STM experiments are given in the Supplementary Material (SM)). The $CrBr_3$ islands show a well-ordered moiré

superstructure with 6.3 nm periodicity arising from the lattice mismatch between the $CrBr_3$ and the $NbSe_2$ layers. Fig. 1E shows an atomically resolved STM image of the $CrBr_3$ monolayer, revealing periodically spaced triangular protrusions. These features are formed by the three neighboring Br atoms as highlighted in the Fig. 1F (red triangle) showing the fully relaxed geometry of $CrBr_3/NbSe_2$ heterostructure obtained through density functional theory (DFT) calculations (see SM for details). The measured in-plane lattice constant is 6.5 Å, consistent with the recent experimental value (6.3 Å) of monolayer $CrBr_3$ grown on graphite[30] and our DFT calculations. As expected for a weakly-interacting vdW heterostructure, DFT calculations further confirm that the $CrBr_3$ monolayer retains its ferromagnetic ordering with a magnetocrystalline anisotropy favouring an out-of-plane spin orientation as shown in Fig. 1F. The magnetization density (Fig. 1F) shows that the magnetism arises from the partially filled d orbitals of the Cr^{3+} ion. While the largest magnetization density is found close to the Cr atoms, as expected, there is also significant proximity induced magnetization on the Nb atoms in the underlying $NbSe_2$ layer.

This establishes that our system our system has the required key ingredients for topological superconductivity and now we probe the resulting emergent quantum matter with STS measurements at a temperature of $T = 350$ mK. Fig. 1G shows experimental $\mathrm{d}I/\mathrm{d}V$ spectra (raw data) taken at different locations indicated in Fig. 1D (marked by filled circles). The $\mathrm{d}I/\mathrm{d}V$ spectrum of bare $NbSe_2$ has a hard gap with an extended region of zero differential conductance around zero bias, which can be fitted by a double gap s-wave BCS-type spectrum (see SM for details). In contrast, the spectra taken in the middle of the $CrBr_3$ island have small but distinctly non-zero differential conductance inside the gap of the $NbSe_2$ substrate. Moreover, we observe pairs of conductance onsets at ± 0.3 mV around zero bias (red arrows). The magnetization causes the formation of energy bands (dubbed Shiba bands) that exist inside the superconducting gap of the substrate[9,32]. By introducing spin-orbit interactions (as discussed above), the system can be driven into a topological phase with associated closing and reopening of the gap between the Shiba bands.

We observe edge modes consistent with the expected Majorana modes along the edge of the magnetic island that are the hallmark of 2D topological superconductivity[9,23,24]. Moreover, the spectroscopic feature of the Majorana edge mode appears inside the gap defined by the Shiba bands (the topological gap) and is centred around the Fermi level (E_{F}). A typical spectrum taken at the edge of the $CrBr_3$ island is shown in Fig. 1G, where a peak

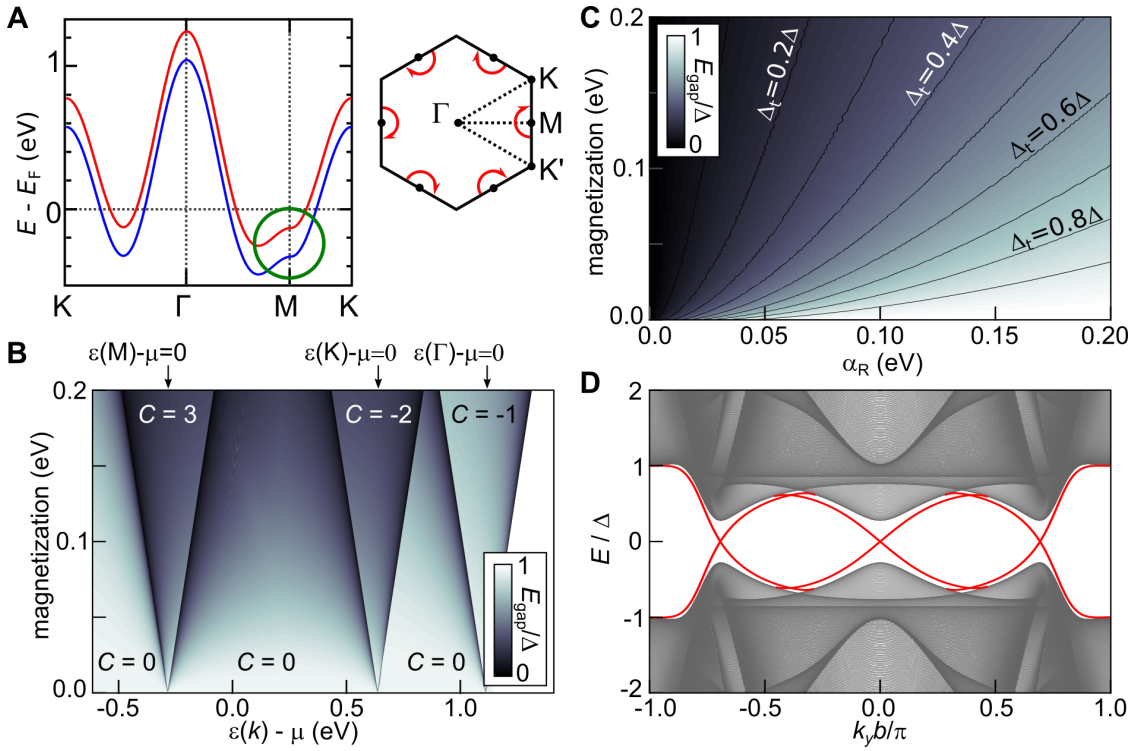

FIG. 2. **Electronic structure of $CrBr_3$-$NbSe_2$ heterostructures.** (**A**) The band structure of the spin-split Nb d-band used in the effective model for topological superconductivity with magnetization $M = 100$ meV. The inset shows the 1st Brillouin zone, where the six M-points and the Rashba texture around them has been highlighted. (**B**) Calculated phase diagram of the magnetized $NbSe_2$ based on the effective low-energy model. The color scale indicates the energy gap $E_{\rm gap}$ (in the units of Δ). (**C**) The calculated topological gap Δ_t as a function of the Rashba and magnetization energies (in units of the superconducting gap Δ). (**D**) Calculated band structure of the topological phase based on a phenomenological tight-binding model (see SM for details).

localized at $E_{\rm F}$ is clearly seen. Furthermore, there are two side peaks located at ± 0.41 mV (see SM for a more detailed analysis) that are very close in energy to the Shiba bands on the $CrBr_3$ layer.

To account for the experimental observations and to corroborate the topological nature of the edge modes, we model the system through DFT calculations and develop an effective low-energy model for the system (see SM for details). The band structure of the Nb d-states derived band used in the effective model is shown in Fig. 2A (direct comparison with DFT is shown in the SM). Topological superconductivity can be generated when magnetization is sufficiently strong to push one of the spin-degenerate bands at a high-symmetry point above

the Fermi energy. We identify the observed topological phase as a state arising from the gap-closing transition at M point with a Chern number $C = 3$. The calculated topological phase diagram in Fig. 2B indicates that for a reasonable magnetization of $M \lesssim 100$ meV, the $C = 3$ state lies approximately 100-200 meV below the Fermi energy of pristine $NbSe_2$. Thus, a small renormalization of the chemical potential resulting from the contact with the magnetic material will drive the system to the topological phase. The two other nontrivial phases that originate from gap closings at the Γ point and K points give rise to topological phases with $C = -1$ and $C = -2$. Realization of either of these phases would require notably larger shifts in chemical potential (~ 0.6 eV), making them improbable for the experimental observations. The absolute values of the nontrivial Chern numbers can be understood by a three-fold rotational symmetry (see SM).

The key quantity characterizing robustness of the nontrivial phase is the topological energy gap Δ_t. This scale should be much larger than temperature for the state to be observable in experiment. In the simple parabolic band model this quantity can be estimated by $\Delta_t = \alpha k_F/[(\alpha k_F)^2 + M^2]^{1/2}$, where α is the Rashba coupling and k_F the Fermi wavelength[37]. The calculated gap based on our more realistic tight-binding (TB) model is shown in Fig. 2C. Based on the experimental results shown in Fig. 1G, the topological gap is $\Delta_t \approx 0.3\Delta$. The calculated band structure in a strip geometry corresponding to the experimental gap is shown in Fig. 2D, where we see the Majorana edge modes crossing the topological gap. The edge modes are seen to coexist with the bulk states in a finite subgap energy window in agreement with experimental observations.

To further elucidate the properties of the Majorana edge modes, we have carried out spatially resolved $\mathrm{d}I/\mathrm{d}V$ spectroscopy over the edge of the $CrBr_3$ island (Fig. 3A). It can be seen that the edge mode is more localized at the edge at zero bias (deeper within the topological gap), but becomes more delocalized at energies closer to the topological gap edge. Moreover, the energy dependence of the main feature of the edge mode LDOS is such that it splits off from the top edge of the topological gap inside the $CrBr_3$ island, smoothly crosses the topological gap and merges with its lower edge outside the $CrBr_3$ island. In order to visualize the evolution of the spatial extension of the Majorana edge modes, we have recorded grid $\mathrm{d}I/\mathrm{d}V$ spectroscopy maps (Fig. 3B-G). At E_F, the Majorana edge modes are confined within ~ 2.4 nm of the edge of the island (see SM). In addition to the edge mode signature close to the Fermi level, there is also enhanced LDOS at the energies similar to size of the

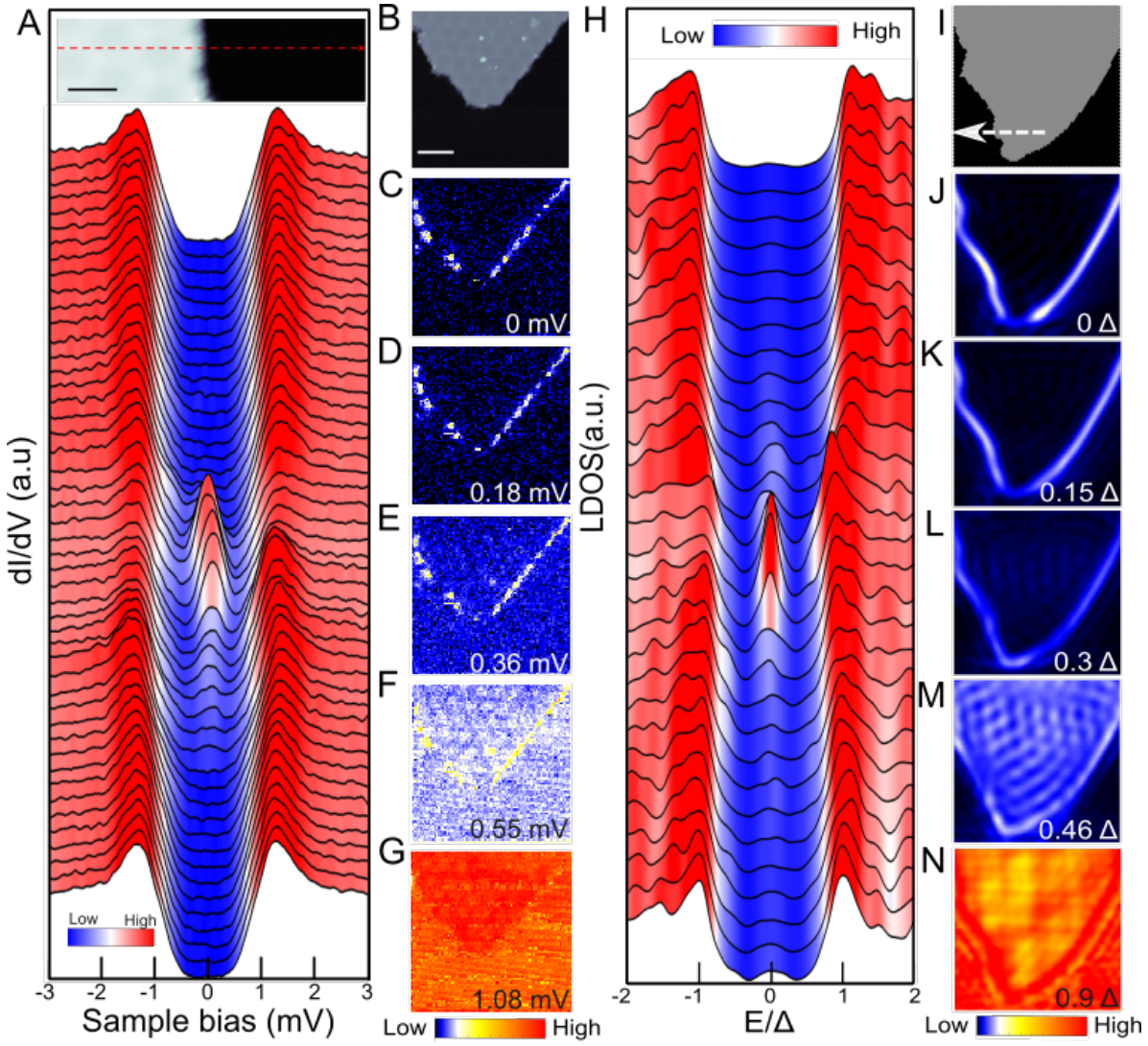

FIG. 3. **Spatially resolved spectroscopy of the Majorana zero modes.** (**A**) dI/dV spectroscopy over the edge of the $CrBr_3$ island (STM topography shown on the top). (**B-G**) STM topography and spatially resolved LDOS maps extracted from grid spectroscopy experiments. STM feedback parameters: (A) $V_{\text{bias}} = +1$ V, $I = 10$ pA; (B) $V_{\text{bias}} = +0.8$ V, $I = 10$ pA. Scale bars: (A) 4 nm; (B) 12 nm. (**H-N**) Corresponding calculated linespectra (H) and LDOS maps (J-N) with the island shape shown in (I) (see SM for details).

topological gap (Fig. 3E,F) where we also see significant excitations inside the magnetic island. The theoretically computed LDOS (Fig. 3H-N, see SM for details) reproduces the essential features of the experimental results and shows exponential localization of Majorana edge modes at the edge of the island at subgap energies. In particular, we confirm the

experimental finding that the distribution of the spectral weight of the edge mode along the edge (excluding the regular moiré pattern) should be non-uniform. This stems from the geometric irregularities of the island boundary with characteristic length scale that is comparable to the edge mode penetration depth. However, this does not imply the edge modes are discontinuous along the edge. It simply means that the interference effects near edge irregularities suppress the visibility of the edge mode due to finite experimental resolution. The simulations also reproduce the slightly dispersing peaked LDOS across the island edge, and the enhanced LDOS at the islands edges at and above the topological gap edge.

It is conceivable that the experimentally observed edge modes could possess a topologically trivial origin, unrelated to the existence of a topological superconducting state. However, in addition to the near quantitative match with the theoretical results incorporating the main ingredients of the experimental system, the edge mode signature is experimentally very robust. We consistently observe it in our hybrid vdW heterostructures on all $CrBr_3$ islands, irrespective of their specific size and shape (see SM for more examples). To prove the observed edge modes of the hybrid heterostructures are strongly linked to the superconductivity of the $NbSe_2$ substrate, we have carried out experiments in magnetic fields up to 4 T, suppressing superconductivity in the $NbSe_2$ substrate. All features associated with the gap at the center of the island and the edge modes disappear in the absence of superconductivity in $NbSe_2$ (see SM for details). This rules out trivial edge modes as the cause of the observed results. Another non-topological reason for resonances close to the Fermi energy, the Kondo effect, should also be present in the normal state and can hence be ruled out as well.

In conclusion, our work constitutes two breakthroughs in designer quantum materials. By fabricating vdW heterostructures with 2D ferromagnet epitaxially coupled to superconducting $NbSe_2$, we obtained a near ideal designer structure exhibiting two competing electronic orders. The induced magnetization and spin-orbit coupling renders the superconductor topologically nontrivial, supporting Majorana edge channels which we characterized by STM and STS measurements. The demonstrated heterostructure provides a high-quality platform for electrical devices employing topological superconductivity. This is an essential step towards practical devices employing topological superconductivity and the demonstrated system would in principle allow electrical control of the topological phase through

electrostatic tuning of the chemical potential.

ACKNOWLEDGMENTS

This research made use of the Aalto Nanomicroscopy Center (Aalto NMC) facilities and was supported by the European Research Council (ERC-2017-AdG no. 788185 "Artificial Designer Materials"), Academy of Finland (Academy professor funding no. 318995 and 320555, and Academy postdoctoral researcher no. 309975), and the Aalto University Centre for Quantum Engineering (Aalto CQE). SG acknowledges the support of National Science Centre (NCN, Poland) under grant 2017/27/N/ST3/01762. Computing resources from the Aalto Science-IT project and CSC, Helsinki are gratefully acknowledged. ASF has been supported by the World Premier International Research Center Initiative (WPI), MEXT, Japan.

---

* Email: kezilebieke.shawulienu@aalto.fi, teemu.ojanen@tuni.fi, peter.liljeroth@aalto.fi

[1] A. K. Geim, I. V. Grigorieva, Van der Waals heterostructures, *Nature* **499**, 419 (2013).

[2] K. S. Novoselov, A. Mishchenko, A. Carvalho, A. H. Castro Neto, 2D materials and van der Waals heterostructures, *Science* **353**, aac9439 (2016).

[3] Y. Cao, *et al.*, Unconventional superconductivity in magic-angle graphene superlattices, *Nature* **556**, 43 (2018).

[4] M. Gibertini, M. Koperski, A. F. Morpurgo, K. S. Novoselov, Magnetic 2D materials and heterostructures, *Nat. Nanotechnol.* **14**, 408 (2019).

[5] L. Yan, P. Liljeroth, Engineered electronic states in atomically precise artificial lattices and graphene nanoribbons, *Adv. Phys. X* **4**, 1651672 (2019).

[6] A. A. Khajetoorians, D. Wegner, A. F. Otte, I. Swart, Creating designer quantum states of matter atom-by-atom, *Nat. Rev. Phys.* (2019).

[7] R. M. Lutchyn, *et al.*, Majorana zero modes in superconductor-semiconductor heterostructures, *Nat. Rev. Mater.* **3**, 52 (2018).

[8] C. Nayak, S. H. Simon, A. Stern, M. Freedman, S. Das Sarma, Non-Abelian anyons and topological quantum computation, *Rev. Mod. Phys.* **80**, 1083 (2008).

[9] M. Sato, Y. Ando, Topological superconductors: a review, *Rep. Prog. Phys.* **80**, 076501 (2017).

[10] V. Mourik, *et al.*, Signatures of Majorana fermions in hybrid superconductor-semiconductor nanowire devices, *Science* **336**, 1003 (2012).

[11] S. Nadj-Perge, *et al.*, Observation of Majorana fermions in ferromagnetic atomic chains on a superconductor, *Science* **346**, 602 (2014).

[12] H. Kim, *et al.*, Toward tailoring Majorana bound states in artificially constructed magnetic atom chains on elemental superconductors, *Sci. Adv.* **4**, eaar5251 (2018).

[13] P. Liu, J. R. Williams, J. J. Cha, Topological nanomaterials, *Nat. Rev. Mater.* **4**, 479 (2019).

[14] B. Jäck, *et al.*, Observation of a Majorana zero mode in a topologically protected edge channel, *Science* **364**, 1255 (2019).

[15] L. Fu, C. L. Kane, Superconducting proximity effect and Majorana fermions at the surface of a topological insulator, *Phys. Rev. Lett.* **100**, 096407 (2008).

[16] H.-H. Sun, *et al.*, Majorana zero mode detected with spin selective Andreev reflection in the vortex of a topological superconductor, *Phys. Rev. Lett.* **116**, 257003 (2016).

[17] S. Zhu, *et al.*, Nearly quantized conductance plateau of vortex zero mode in an iron-based superconductor, *Science* **367**, 189 (2020).

[18] P. Zhang, *et al.*, Observation of topological superconductivity on the surface of an iron-based superconductor, *Science* **360**, 182 (2018).

[19] D. Wang, *et al.*, Evidence for Majorana bound states in an iron-based superconductor, *Science* **362**, 333 (2018).

[20] J. Röntynen, T. Ojanen, Topological superconductivity and high Chern numbers in 2D ferromagnetic Shiba lattices, *Phys. Rev. Lett.* **114**, 236803 (2015).

[21] J. Li, *et al.*, Two-dimensional chiral topological superconductivity in Shiba lattices, *Nat. Commun.* **7**, 12297 (2016).

[22] S. Rachel, E. Mascot, S. Cocklin, M. Vojta, D. K. Morr, Quantized charge transport in chiral Majorana edge modes, *Phys. Rev. B* **96**, 205131 (2017).

[23] G. C. Ménard, *et al.*, Two-dimensional topological superconductivity in Pb/Co/Si(111), *Nat. Commun.* **8**, 2040 (2017).

[24] A. Palacio-Morales, *et al.*, Atomic-scale interface engineering of Majorana edge modes in a 2D magnet-superconductor hybrid system, *Sci. Adv.* **5**, eaav6600 (2019).

[25] Z. Wang, *et al.*, Evidence for dispersing 1D Majorana channels in an iron-based superconductor, *Science* **367**, 104 (2020).

[26] C. Gong, *et al.*, Discovery of intrinsic ferromagnetism in two-dimensional van der Waals crystals, *Nature* **546**, 265 (2017).

[27] B. Huang, *et al.*, Layer-dependent ferromagnetism in a van der Waals crystal down to the monolayer limit, *Nature* **546**, 270 (2017).

[28] D. Ghazaryan, *et al.*, Magnon-assisted tunnelling in van der Waals heterostructures based on $CrBr_3$, *Nature Electronics* **1**, 344 (2018).

[29] Z. Zhang, *et al.*, Direct photoluminescence probing of ferromagnetism in monolayer two-dimensional $CrBr_3$, *Nano Lett.* **19**, 3138 (2019).

[30] W. Chen, *et al.*, Direct observation of van der Waals stacking–dependent interlayer magnetism, *Science* **366**, 983 (2019).

[31] S. Liu, *et al.*, Wafer-scale two-dimensional ferromagnetic Fe_3GeTe_2 thin films grown by molecular beam epitaxy, *npj 2D Mater. Appl.* **1**, 30 (2017).

[32] M. Sato, S. Fujimoto, Topological phases of noncentrosymmetric superconductors: Edge states, Majorana fermions, and non-Abelian statistics, *Phys. Rev. B* **79**, 094504 (2009).

[33] J. D. Sau, R. M. Lutchyn, S. Tewari, S. Das Sarma, Generic new platform for topological quantum computation using semiconductor heterostructures, *Phys. Rev. Lett.* **104**, 040502 (2010).

[34] S. Jiang, J. Shan, K. F. Mak, Electric-field switching of two-dimensional van der Waals magnets, *Nat. Mater.* **17**, 406 (2018).

[35] Z. Wu, J. Yu, S. Yuan, Strain-tunable magnetic and electronic properties of monolayer CrI_3, *Phys. Chem. Chem. Phys.* **21**, 7750 (2019).

[36] S. Jiang, L. Li, Z. Wang, K. F. Mak, J. Shan, Controlling magnetism in 2D CrI_3 by electrostatic doping, *Nat. Nanotechnol.* **13**, 549 (2018).

[37] J. Alicea, Majorana fermions in a tunable semiconductor device, *Phys. Rev. B* **81**, 125318 (2010).

How to measure a Majorana: The Majorana polarization of a topological planar Josephson junction

Szczepan Głodzik,* Nicholas Sedlmayr,† and Tadeusz Domański‡
Institute of Physics, M. Curie-Skłodowska University, 20-031 Lublin, Poland
(Dated: April 6, 2020)

We analyze the topological superconductivity, and investigate the spectroscopic properties manifested by zero-energy modes, induced in a metallic strip embedded into a Josephson-type junction. Focusing on the Majorana polarization of such quasiparticles we propose feasible means for its empirical detection, using the spin selective Andreev reflection method. Our study reveals a gradual development of a transverse gradient of the Majorana polarization across the metallic strip upon increasing its width. We also inspect the spatial profile and polarization of the Majorana quasiparticles in the presence of a strong electrostatic defect. We show that, depending on its position, such a defect can lead to a substantial localization of the Majorana mode.

I. INTRODUCTION

Topological materials, including those which are either insulators or superconductors, differ qualitatively from their ordinary counterparts due to the emergence of in-gap modes. Such quasiparticles develop at boundaries or internal defects and are topologically protected (thus being good candidates for stable qubits), and obey fractional statistics (which is appealing for quantum computations). Experimental efforts for the realization of these exotic quasiparticles have so far largely focused on one-dimensional structures, e.g. semiconducting nanowires proximitized to superconductors,[1–5] nanochains of magnetic atoms deposited on superconducting substrates,[6–11] and lithographically fabricated nanostructures.[12] Another direction in pursuit of topological superconductivity relies on two-dimensional systems, where the in-gap quasiparticles are chiral modes.[13–17] Such Majorana edge modes have indeed been observed in STM measurements, using nanoscopic islands of magnetic atoms deposited on superconducting substrates.[18–20] Further interesting perspectives are related with mixed-dimensionality systems, where the localized and delocalized Majorana quasiparticles coexist with one another.[21,22] In particular, nanowires attached to larger structures[23] could enable a controllable transfer of the Majorana modes between these constituents,[24] indirectly probing their Chern numbers.[25]

Yet another promising platform for the realization of topological superconductivity hosting localized Majorana modes has been suggested in Refs.[26,27] using metallic strips with strong spin-orbit coupling embedded between two superconducting leads with differing phases (see Fig. 1). Signatures of zero-energy modes have been observed in such heterostructures, consisting both of aluminium on indium arsenide[28] and an HgTe quantum well coupled to thin-film aluminium.[29] The major virtue of a Josephson-type geometry is its tunability to the topologically non-trivial regime, easily controlled experimentally by varying the phase difference. Another way for a controllable transition to the topological phase is possible by using two gate-tunable Josephson junctions (i.e. a SQUID geometry), as recently reported for epitaxial Al/InAs structures.[30]

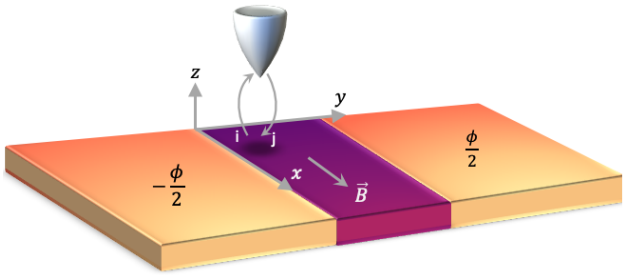

FIG. 1. A schematic view of a metallic strip (dark purple), embedded between superconducting regions (yellow) which differ in phase by ϕ, probed by a polarized STM tip (light gray). A magnetic field $\vec{B} = B_0\hat{x}$ is applied to the whole structure.

Experiments on these Josephson junction heterostructures[28–30] have triggered further intensive studies.[31–34] The proximitized metallic strips are hoped, for instance, to enable a current-controlled braiding of the Majorana modes.[35] It has also been suggested[36] that weak disorder promotes localization of the Majorana quasiparticles.

Intrigued by this prediction, we study here the spatial profiles and polarizations of the Majorana modes. We also consider a single strong point-like electrostatic scattering potential placed in various regions of the proximitized metallic strip. For this purpose we perform numerical calculations within the Bogoliubov-de Gennes treatment. Our study reveals that, when this local defect is placed in an interior of the metallic stripe its influence on the Majorana modes is naturally practically negligible, but when placed near a region of the existing Majorana quasiparticle we observe a tendency towards reducing the spatial extent of the zero-energy modes, in some analogy to what has been predicted by Haim and Stern.[36] These phenomena are in stark contrast to the properties of Majorana quasiparticles of strictly 1-dimensional systems, where sufficiently strong local defects can produce additional pairs of the Majorana modes.

We also inspect the *Majorana polarization* introduced

in Refs. 21, 37–39 and considered by one of us.[40] We show that this quantity could be particularly useful in characterizing the zero-energy quasiparticles of metallic strips whose experimentally reported length-to-width ratio was about 20 (Ref. 28) or 100 (Ref. 29). It is known that quasi 2-dimensionality induces transverse gradients in the Majorana polarization.[21,38,41] Similarly quasi 1-dimensional systems, such as those considered here, can have long localization length scales for the Majorana bound states which can also induce transverse gradients in the Majorana polarization. Strictly the gradient is induced in the phase of the Majorana polarization, and in the magnitude of the Majorana polarization *relative to its density*. We prove that the magnitude (absolute value) can be probed by selective equal spin Andreev reflection spectroscopy.[42] A similar method has previously been applied for inspecting the spin polarization of the Majorana quasiparticles of Fe atom chains using a magnetic STM tip.[10] The advantage of the method proposed here is that it would be a direct probe of the Majorana nature of the quasiparticles. Transverse gradients of the Majorana polarization, relative to the density, are an indication of a delocalization process that ultimately could be detrimental to the zero-energy modes.

This paper is organized as follows. In Sec. II we present the microscopic model and briefly outline methodological details. In Sec. III we investigate the spatial profiles and polarization of the Majorana modes, focusing on their evolution with respect to varying the width of the homogeneous metallic strip. Sec. V discusses the Majorana localization driven by a point-like electrostatic defect, and Sec. VI summarizes the main results.

II. MICROSCOPIC MODEL

For a description of the planar Josephson heterostructure, see Fig. 1, we employ the microscopic scenario discussed in Refs. 26, 27, and 43. The model Hamiltonian,

$$\mathcal{H} = \mathcal{H}_0 + \mathcal{H}_Z + \mathcal{H}_S \,, \tag{1}$$

consists first of the free term

$$\mathcal{H}_0 = \sum_{\substack{\langle i,j\rangle \\ \sigma,\sigma'}} \left[\mathrm{i}\lambda(\mathbf{d}_{ij}\times\vec{\boldsymbol{\sigma}}_{\sigma\sigma'})_z - t\delta_{\sigma\sigma'}\right] d^\dagger_{i\sigma} d_{j\sigma'} - \mu \sum_{i\sigma} d^\dagger_{i\sigma} d_{i\sigma} \tag{2}$$

describing itinerant electrons hopping all over the sample. t is the hopping integral between the nearest neighbor sites on a square lattice, λ is the strength of the Rashba spin-orbit coupling, $\mathbf{d}_{ij}$ is the vector connecting nearest neighbors, and $\boldsymbol{\sigma}$ stands for the vector of the Pauli matrices. The second (Zeeman) term

$$\mathcal{H}_Z = B_0 \sum_i \sum_{\sigma\sigma'} d^\dagger_{i\sigma} \boldsymbol{\sigma}^x_{\sigma\sigma'} d_{i\sigma'} \tag{3}$$

accounts for the influence of an external magnetic field B_0 which is parallel to the interface between the metallic and superconducting regions, as reported experimentally.[28,29] The last part appearing in the model Hamiltonian (1) describes the on-site pairing in the left (S_L) and right (S_R) superconducting regions,

$$\mathcal{H}_S = \sum_i \left(\Delta_i d^\dagger_{i\downarrow} d^\dagger_{i\uparrow} + \mathrm{H.c.}\right) \,, \tag{4}$$

where

$$\Delta_i = \begin{cases} \Delta \mathrm{e}^{-\mathrm{i}\phi/2} & \text{for } i \in S_L \,, \\ \Delta \mathrm{e}^{\mathrm{i}\phi/2} & \text{for } i \in S_R \,, \text{ and} \\ 0 & \text{for } i \in N \,. \end{cases} \tag{5}$$

Here the metallic strip region is denoted by N. The phase difference between the superconducting layers S_R and S_L is ϕ and Δ is real.

We studied the finite-size version of this model, consisting of N_x sites along x-direction and N_y sites along y-axis. For specific computations we assumed $N_x = 91$ and $N_y = 30$, unless stated otherwise. The eigenstates and eigenenergies of the heterostructure were determined numerically, solving the Bogoliubov de-Gennes equations with the canonical transformation

$$\begin{pmatrix} d_{i\uparrow} \\ d^\dagger_{i\downarrow} \end{pmatrix} = \sum_n \begin{bmatrix} u^n_{i\uparrow} & (v^n_{i\downarrow})^* \\ -v_{i\downarrow} & (u_{i\uparrow})^* \end{bmatrix} \begin{pmatrix} \gamma_n \\ \gamma^\dagger_n \end{pmatrix} \,, \tag{6}$$

where $\gamma^{(\dagger)}_n$ stand for the Bogoliubov quasiparticles which diagonalize the Hamiltonian: $H = \sum_n E_n \gamma^\dagger_n \gamma_n + \text{const.}$

In particular we have calculated the local density of states

$$\rho_i(\omega) = \sum_{n,\sigma} \left(|u^n_{i\sigma}|^2 \delta(\omega - E_n) + |v^n_{i\sigma}|^2 \delta(\omega + E_n)\right) \,. \tag{7}$$

As we consider a finite size system we have broadened the delta function peaks to Lorentzian functions of width 0.02Δ.

Another quantity of interest is the Majorana polarization[21,38] for an eigenstate $|\psi_n\rangle$,

$$\mathcal{P}_{in} = \langle\psi_n|\mathcal{C}\hat{r}_i|\psi_n\rangle = \sum_\sigma \boldsymbol{\sigma}^z_{\sigma\sigma} 2u^n_{i\sigma} v^n_{i\sigma} \,, \tag{8}$$

where $\hat{r}_i$ is projection onto site i and $\mathcal{C}$ is the particle-hole operator. This quantity allows one to probe directly the Majorana nature of the eigenstates, and its experimental measurement is discussed in Sec. III B. For convenience we introduce

$$\mathcal{P}_i = \mathcal{P}_{i\uparrow} - \mathcal{P}_{i\downarrow} \tag{9}$$

where

$$\mathcal{P}_{i\sigma} = 2u^{n_0}_{i\sigma} v^{n_0}_{i\sigma} \,. \tag{10}$$

for the zero-energy ($n = n_0$) quasiparticles. More generally one may wish to consider the particle-hole overlap $u^n_{i\sigma_1} v^m_{j\sigma_2}$. In particular the equal-spin pairing ($\sigma_1 = \sigma_2$) induced between the neighboring sites i and j for the zero-energy quasiparticles ($E_n = 0 = E_m$) is of interest. More details on this issue are discussed in Sec. III B.

III. TOPOGRAPHY OF MAJORANA MODES

Upon substituting the metallic strip between the superconducting reservoirs, their Cooper pairs leak into the normal region, inducing on-site electron pairing. This proximity effect is efficient nearby the bulk superconductors, up to distances smaller than the coherence length ξ. Here we consider metallic samples comprising a few N_w atomic rows, whose spatial width $N_w a \leq \xi$, where a is the inter-atomic distance. Under such a condition the proximity effect induces superconductivity across the entire metallic region. The appearance of the topological superconducting phase, however, can be realized only with triplet pairing which can be achieved by combining conventional superconductivity with the spin-orbit Rashba interaction and Zeeman splitting.[5]

It has been demonstrated[26,27] that a transition from the topologically trivial to the nontrivial superconducting state is sensitive to the Josephson phase ϕ. Characteristic features of the emerging Majorana quasiparticles can, however, additionally depend on the width $N_w a$ of the metallic strip. In what follows we analyze such qualitative changes and propose a method for their empirical detection (Sec. IV).

A. Zero-energy spectral function

Focusing on the optimal condition for the topological superconducting state $\phi = \pi$, we have checked that the on-site pairing $\langle d_{i\downarrow} d_{i\uparrow} \rangle$ spreads nearly uniformly onto the metallic strip, both along and across it. Furthermore, we also noticed some feedback of the metallic sector onto superconducting regions manifested by partial reduction of the local pairing (sometimes referred to as the inverse superconducting proximity effect). Next, when combined with the spin-orbit interaction and the Zeeman field, the proximitized metallic stripe develops inter-site pairing of identical spin electrons, i.e. triplet pairing. For sufficiently strong magnetic fields B_0, such a triplet superconducting phase becomes topologically nontrivial, leading to the emergence of the zero-energy quasiparticles.[26,27]

Fig. 2 displays the spatial profiles of the local density of states at zero energy $\rho_i(0)$, obtained for very narrow metallic strips. We note that the Majorana quasiparticles of the narrow metallic strip are well localized at its ends. Their overall topography is practically identical with all features of one-dimensional systems, including the characteristic oscillations along the metallic strip.[44] It comes as perhaps some surprise that this narrow width of metallic region is neither essential for the development of the topological superconducting phase, nor important for the spatial profile of the Majorana modes. Even in the extreme case $N_w = 0$, i.e. without any metallic piece between the phase-differing superconductors, such modes are still present. On the other hand, when the width N_w increases we see a gradual smearing of the zero-energy quasiparticles and novel features appearing in the Majorana polarization. This is a consequence of the reduced proximity induced gap in wider strips which naturally reduces the localization of any mid-gap states.

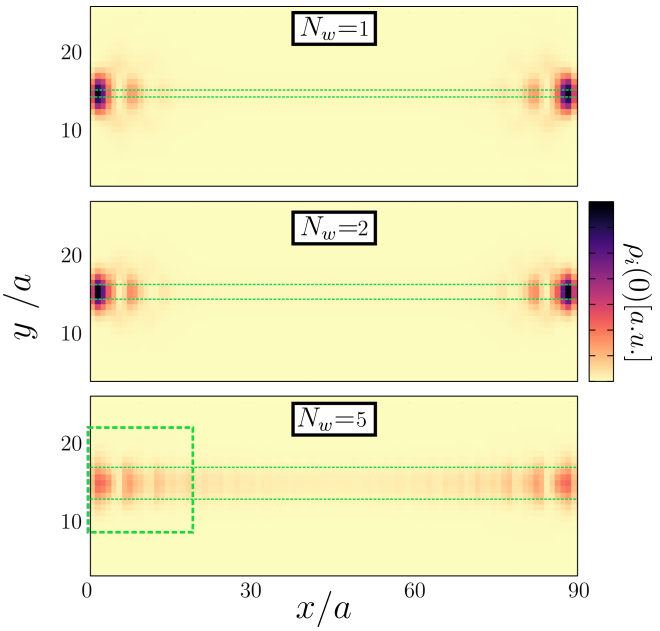

FIG. 2. The spatial profiles, $\rho_i(0)$, of the Majorana quasiparticles appearing in a metallic strip consisting of 1, 2 and 5 rows of atomic chains, as indicated. We have used the model parameters $\Delta = 0.25t$, $\phi = \pi$, $\lambda = 0.5t$, $B_0 = 0.1t$, $\mu = -3.75t$. The Majorana polarization (10) for the area in the green square is shown in Fig. 3.

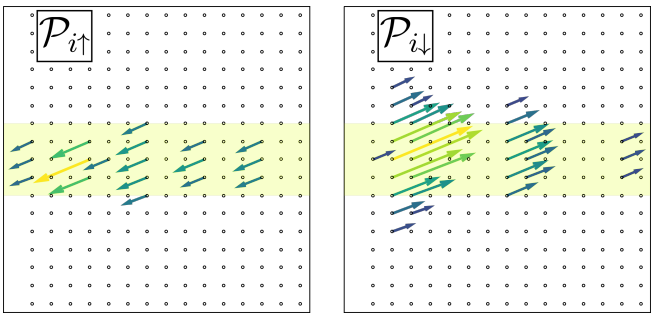

FIG. 3. Components of the Majorana polarization $\mathcal{P}_{i\sigma}$ obtained for the region highlighted by the dashed frame in Fig. 2. The magnitude of the arrows shows $|\mathcal{P}_{i\sigma}|$ and their direction shows $\mathrm{Arg}\,\mathcal{P}_{i\sigma}$. We note that the phase of the Majorana polarization is only well defined up to a global shift. The shaded region is the metallic strip.

B. Majorana polarization

Majorana modes are quasiparticles with energy $E_n = 0$ (we denote such doubly-degenerate eigenstate by $n \equiv n_0$) and which are eigenstates of the particle-hole transformation operator. We analyze here another valuable source of information about these modes encoded in the Majorana polarization.[37–39,45] This quantity is particularly useful for characterizing the Majorana modes of quasi two-dimensional topological superconductors[21,38,41] where its phase develops both longitudinal and transverse variation. As we shall see, its texture brings an important message about the delocalized Majorana quasiparticles.

Let us start by checking the contributions $\mathcal{P}_{i\sigma}$ from each spin σ to the Majorana polarization in the narrow metallic strips, when the zero-energy quasiparticles are well localized near its ends. To be specific, we focus on the region marked by the dashed lines in the bottom panel in Fig. 2. Both constituents $\mathcal{P}_{i\sigma}$ are depicted in Fig. 3 on the lattice sites of the marked metallic region. We clearly note that the directions of the arrows depicting $\mathcal{P}_{i\uparrow}$ are opposite to $\mathcal{P}_{i\downarrow}$, which is typical for both strictly one-dimensional topological superconductors (see Fig. 2 in Ref. 40) and for higher dimensions as well.[21,38,41] The magnitudes of the two components, shown by the length of the arrows, are however very different. It is important to emphasize, that for the realization of a true MBS the local phase of $\mathcal{P}_{i\uparrow} - \mathcal{P}_{i\downarrow}$ must be constant. Such a constraint $\mathcal{P}_{i\uparrow} = \mathrm{e}^{\mathrm{i}\varphi}|\mathcal{P}_{i\uparrow}| = -\mathrm{e}^{\mathrm{i}\varphi}|\mathcal{P}_{i\downarrow}|$ seems to be satisfied in our case only for narrow metallic strips.

There are in fact two conditions on $\mathcal{P}_i$ which are required for Majorana modes. The first, which we have seen here, is that its phase must be constant. The phase of $\mathcal{P}_i$ does not appear to be measurable in any simple way. What is measurable, as we will show in Sec. IV, is its magnitude $|\mathcal{P}_i|$. For a Majorana mode we require $|\mathcal{P}_i| = \rho_i^0$, and this gives a measurable determination of Majorana modes. Upon increasing the width of the metallic strip the Majorana polarization gradually develops varying orientations, both along and across the sample. Emergence of the transverse gradient is very sensitive to the width N_w, as illustrated in Fig. 4.

IV. POLARIZED ANDREEV SPECTROSCOPY

Here we briefly discuss an empirical method based on spin polarized Andreev reflection spectroscopy,[42] which could probe the absolute value of the Majorana polarization. Let us consider a scanning tunnelling microscope (STM) tip approaching site i of our heterostructure. The influence of this external reservoir of itinerant electrons can be incorporated by augmenting the model Hamiltonian Eq. (1) with the local term

$$H_i = \underbrace{\sum_{\mathbf{k},\sigma}(\varepsilon_{\mathbf{k}} - \mu_{tip})c^\dagger_{\mathbf{k}\sigma}c_{\mathbf{k}\sigma}}_{\text{STM tip}} + \underbrace{\sum_{\mathbf{k},\sigma}\left(\gamma_{\mathbf{k},\sigma}c^\dagger_{\mathbf{k}\sigma}d_{i\sigma} + H.c.\right)}_{\text{hybridization}}, \tag{11}$$

where the chemical potential of the tip, $\mu_{tip} = \mu + eV$, can be varied by an applied bias voltage V. $\varepsilon_{\mathbf{k}}$ is the dispersion of the tip electrons, and $\gamma_{\mathbf{k}}$ the tunneling amplitude from the tip to the heterostructure and vice-versa. The quasiparticle spectrum at site i can be indirectly deduced from measurements of the charge transport induced by the voltage V applied between the STM tip and the sample. In the subgap regime, i.e. for $e|V| \leq \Delta$, such a current would solely originate from Andreev scattering processes. This mechanism relies on the conversion of electrons arriving from the STM tip into the Cooper pairs of the superconducting heterostructure, with holes being reflected back into the STM tip.

We are interested here in probing the topological superconducting phase related to the p-wave pairing of equal spin electrons induced between neighboring sites, analogous to the situation in Kitaev's simple model.[46] For this purpose let us assume a complete polarization of the tip, where only one spin component σ can participate in the charge transport. On a microscopic level we thus imagine that an itinerant electron of spin σ arrives from the polarized STM tip at site i where it forms a triplet pair with an electron from the neighbouring site j, sending a hole of the same spin orientation into the tip. Within the Landauer formalism we can express the resulting spin-dependent charge current by[40]

$$I^\sigma_{ij}(V) = \frac{e}{h}\int \mathrm{d}\omega\; T^\sigma_{ij}(\omega)\;\left[f(\omega - eV) - f(\omega + eV)\right], \tag{12}$$

where $f(\omega) = \left[1 + \exp\left(\omega/k_BT\right)\right]^{-1}$ is the Fermi-Dirac distribution function. The main quantites of interest are the spatially-dependent transmission probabilities[40]

$$T^\sigma_{ij}(\omega) = \Gamma_N^2\;\left|\mathcal{F}^\sigma_{ij}(\omega)\right|^2, \tag{13}$$

where $\mathcal{F}^\sigma_{ij}(\omega) = \langle\langle \hat{d}_{i\sigma}; \hat{d}_{j\sigma}\rangle\rangle_\omega$ is the Fourier transform of the anomalous retarded Green's function in Nambu representation. For practical reasons, because we focus on a small charge transport window which is only a fraction of meV around the chemical potential μ of our sample, we have introduced a constant coupling strength, $\Gamma_N \equiv 2\pi\sum_{\mathbf{k}}|\gamma_{\mathbf{k}}|^2\delta(\omega - \varepsilon_{\mathbf{k}})$. Formally it is equivalent to the wide band limit approximation.

The anomalous Green's function $\mathcal{F}^\sigma_{ij}(\omega)$ has the explicit form, for $\sigma = \uparrow$,

$$\mathcal{F}^\uparrow_{ij}(\omega) = -\sum_n\left[\frac{u^n_{i\uparrow}(v^n_{j\uparrow})^*}{\omega + i\Gamma_N - E_n} + \frac{u^n_{j\uparrow}(v^n_{i\uparrow})^*}{\omega + i\Gamma_N + E_n}\right], \tag{14}$$

where $u^n_{j\uparrow}$ and $v^n_{j\uparrow}$ can be computed numerically.

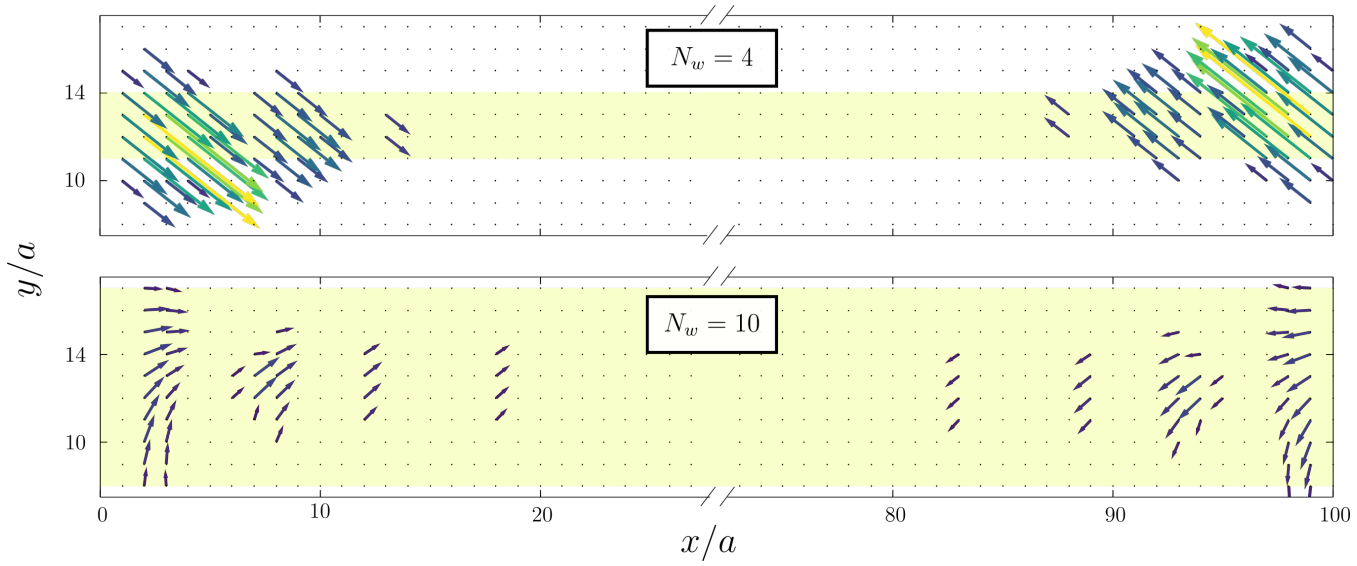

FIG. 4. The Majorana polarization $\mathcal{P}_i$ obtained for the heterostructure comprising $N_w = 4$ (top) and $N_w = 10$ (bottom) atomic rows in the metallic strip, marked by the shaded region. Numerical results are obtained for the same model parameters as in Fig. 2 but using $N_x = 100$, $Ny = 20$. The magnitude of the arrows shows $|\mathcal{P}_{i\sigma}|$ and their direction shows $\mathrm{Arg}\,\mathcal{P}_{i\sigma}$. We note that the phase is only well defined up to a global shift.

Focusing on the zero-energy limit $\omega \to 0$, dominated by the Andreev scatterings via the Majorana quasiparticle ($E_{n_0} = 0$), we can express the transmittance by

$$T^{\sigma}_{ij}(\omega \sim 0) \simeq \frac{\Gamma_N^2}{\omega^2 + \Gamma_N^2} \left| u^{n_0}_{i\sigma}(v^{n_0}_{j\sigma})^* + u^{n_0}_{j\sigma}(v^{n_0}_{i\sigma})^* \right|^2 . \quad (15)$$

Substituting Eq. (15) into the Andreev current formula (12) yields, at low temperatures, the following zero-bias differential conductance

$$\lim_{V\to 0} \frac{dI^{\sigma}_{ij}(V)}{dV} \simeq \frac{4e^2}{h} \left| u^{n_0}_{i\sigma} \left(v^{n_0}_{j\sigma}\right)^* + u^{n_0}_{j\sigma} \left(v^{n_0}_{i\sigma}\right)^* \right|^2 . \quad (16)$$

This result (16) demonstrates that selective Andreev transport might probe the spin-dependent contribution (10) to the Majorana polarization. Strictly speaking, however, such tunneling processes occur on the links (involving the neighbouring sites i and j) rather than on individual local sites. For this reason the differential conductance (16) would measure the *symmetrized Majorana polarization*

$$\mathcal{P}_{<ij>,\sigma} = u^{n_0}_{i\sigma} v^{n_0}_{j\sigma} + u^{n_0}_{j\sigma} v^{n_0}_{i\sigma} \quad (17)$$

over the neighboring sites i and j, instead of the strictly local definition (10). Since the diagonalization coefficients are slowly varying in space, $u^n_{j\sigma} \approx u^n_{i\sigma}$, $v^n_{j\sigma} \approx v^n_{i\sigma}$, the symmetrized $\mathcal{P}_{<ij>,\sigma}$ and local $\mathcal{P}_{i,\sigma}$ Majorana polarizations should in practice be nearly identical.

Let us finally recall that the complex vector $u^{n_0}_{i\uparrow} v^{n_0}_{i\uparrow}$ is typically perfectly opposite to $u^{n_0}_{i\downarrow} v^{n_0}_{i\downarrow}$, see Fig. 3. This implies, that the absolute value of the Majorana polarization (9) $|\mathcal{P}_i| = |\mathcal{P}_{i\uparrow}| + |\mathcal{P}_{i\downarrow}|$, and the same holds for the symmetrized Majorana polarization.

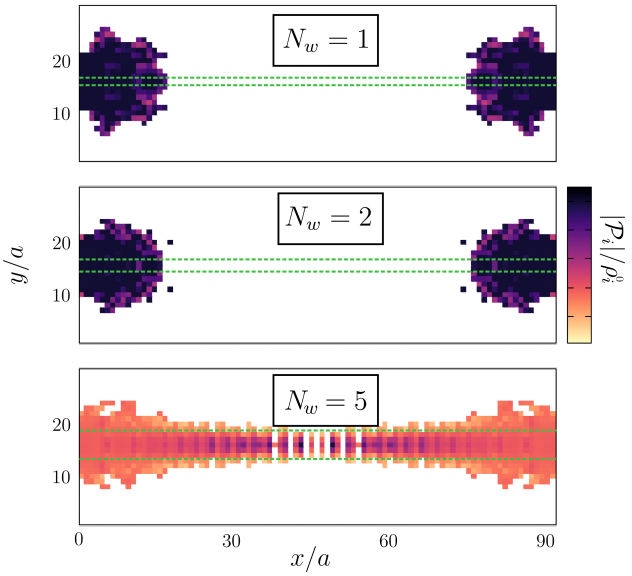

FIG. 5. The spatial profile of $|\mathcal{P}_i|/\rho^0_i$ for the potential zero-energy Majorana quasiparticles appearing in the metallic strip consisting of 1, 2 and 5 rows of atomic chains, as indicated. We have used the same model parameters as in Fig. 2: $\Delta = 0.25t$, $\phi = \pi$, $\lambda = 0.5t$, $B_0 = 0.1t$, $\mu = -3.75t$. The difference between the well isolated MBS and the delocalized states in the wider strip is evident.

In conclusion, by measuring the zero-bias differential conductance $\frac{dI^{\sigma}_{ij}(0)}{dV}$ of the spin-selective Andreev current flowing through the neighboring sites i and j one can evaluate the absolute value of the symmetrized Majorana

polarization

$$|\mathcal{P}_{<ij>}| = \sqrt{\frac{h}{4e^2}} \sqrt{\frac{d}{dV}\left[I_{ij}^{\uparrow}(0) + I_{ij}^{\downarrow}(0)\right]}. \qquad (18)$$

As far as the spatial variation of the phase is concerned, its determination is, if possible, evidently more cumbersome. This problem is beyond the scope of the present study.

Although the spatial variation of the phase is not currently measurable we can compare the absolute value of $|\mathcal{P}_i|$ with $\rho_i(0)$. For a MBS these must be the same, therefore if we plot the ratio of these measurable quantities, $|\mathcal{P}_i|/\rho_i(0)$, it should be flat for a MBS. In Fig. 5 we show results for $N_w \in \{1, 2, 5\}$, comparable to Fig. 2, which show that the MBS profile is indeed flat. For $N_w = 5$, when the two MBS at either end of the strip start to overlap, this quantity is no longer flat. Thus this can be used as an experimental determination of whether localized states are actually MBS. It is worth noting that increasing the length N_x of the system would result in $|\mathcal{P}_i|/\rho_i(0)$ being flat even for $N_w > 5$.

V. LOCALIZATION OF THE MAJORANA MODES

In Sec. III we have shown that upon increasing the width N_w of a metallic strip the topological superconducting state reveals (i) smearing of the Majorana quasiparticle, and (ii) development of the transverse gradient of the Majorana polarization. One may ask, however, whether there is any chance of localization of the Majorana modes. In this section we illustrate that such an effect could be observable due to local defects introduced in certain regions of the metallic strip.

Topological superconductivity in 1-dimensional wires and atomic chains has been shown to be robust against weak disorder,[47–54] noise,[55] inhomogeneous spin-orbit coupling,[56] reorientation of the magnetic field,[41,57] and thermal fluctuations.[58–61] Sufficiently strong scattering centers, however, could effectively break these 1-dimensional systems into separate segments, inducing additional pairs of the Majorana modes.[62] Such a mechanism can be expected to be inefficient in 2-dimensional systems. To verify this conjecture for the quasi 2-dimensional heterostructure discussed in this paper we take into consideration a point-like electrostatic defect $\mathcal{H}_{imp} = V_0 d_{i_0\sigma}^{\dagger} d_{i_0\sigma}$ positioned at site i_0 of the metallic region. We assume this scattering potential to be rather strong, $V_0 = 100t$, as otherwise its influence would be less visible.

Let us first assume the scattering potential to be placed in a central part of the metallic region (Fig. 6(a)). Neither the zero-energy spectral function nor the Majorana polarization reveal any influence of such an electrostatic impurity on the existing Majorana quasiparticles, in contrast to the properties of 1-dimensional topological superconductors.[62] This behaviour seems to be quite natural, because the Majorana modes are safely distant from the impurity.

Contrary to this situation, let us next consider the scattering potential near the left side of the metallic strip (Fig. 6(b,c)). We selected the specific sites $i_0 = 4$ and $i_0 = 8$, in order to guarantee a considerable overlap of the local defect with the left hand Majorana mode. Under such circumstances the scattering potential has a substantial influence both on the spectral function (left panels) and the Majorana polarization (right panels). This electrostatic impurity reduces the spatial extent of the Majorana quasiparticle on the left hand side, whereas the other Majorana quasiparticle is practically left intact. Such a tendency towards localization of the Majorana modes has been recently predicted by Haim and Stern,[36] when investigating the different role of weak extended disorder.

Our present study provides more detailed information concerning such disorder-induced-localization, indicating that: (i) disorder present in the internal segments of the metallic strip would naturally be rather ineffective for the Majorana quasiparticles, whereas (ii) disorder introduced to the regions of already existing Majorana quasiparticles substantially reduces their spatial extent. The considerations discussed in Sec. IV suggest that empirical detection of this subtle phenomenon could be feasible. A tendency towards the localization of the Majorana quasiparticles could be observed in the maps of differential conductance for the spin polarized Andreev current induced via the metallic region in the presence of the intentionally deposited local defects. Such an electrostatic scattering potential could be created by applying gate potentials, whereas a magnetic potential, leading to similar effects, can be obtained by locally perturbing the Zeeman field.

VI. SUMMARY

We have theoretically studied the properties of the Majorana quasiparticles emerging in a narrow metallic strip sandwiched between two s-wave superconductors in a Josephson-junction geometry. The topological superconducting phase has been recently reported for such metallic strips by the groups in Copenhagen[28] and Harvard[29] with a length-to-width ratio ranging from 20 to 100, respectively. Using the Bogoliubov de-Gennes treatment we have investigated the role of the finite metallic strip width, exploring its influence on: (a) spatial profiles of the zero-energy quasiparticles and (b) topography of the Majorana polarization that probes the particle-hole overlap of the zero-energy quasiparticles. Furthermore, we have proposed a feasible method for detecting the magnitude of such a Majorana polarization by measuring the differential conductance in spin-polarized Andreev reflection spectroscopy.

We have also analyzed the influence of strong (point-like) electrostatic defects on the Majorana modes. We

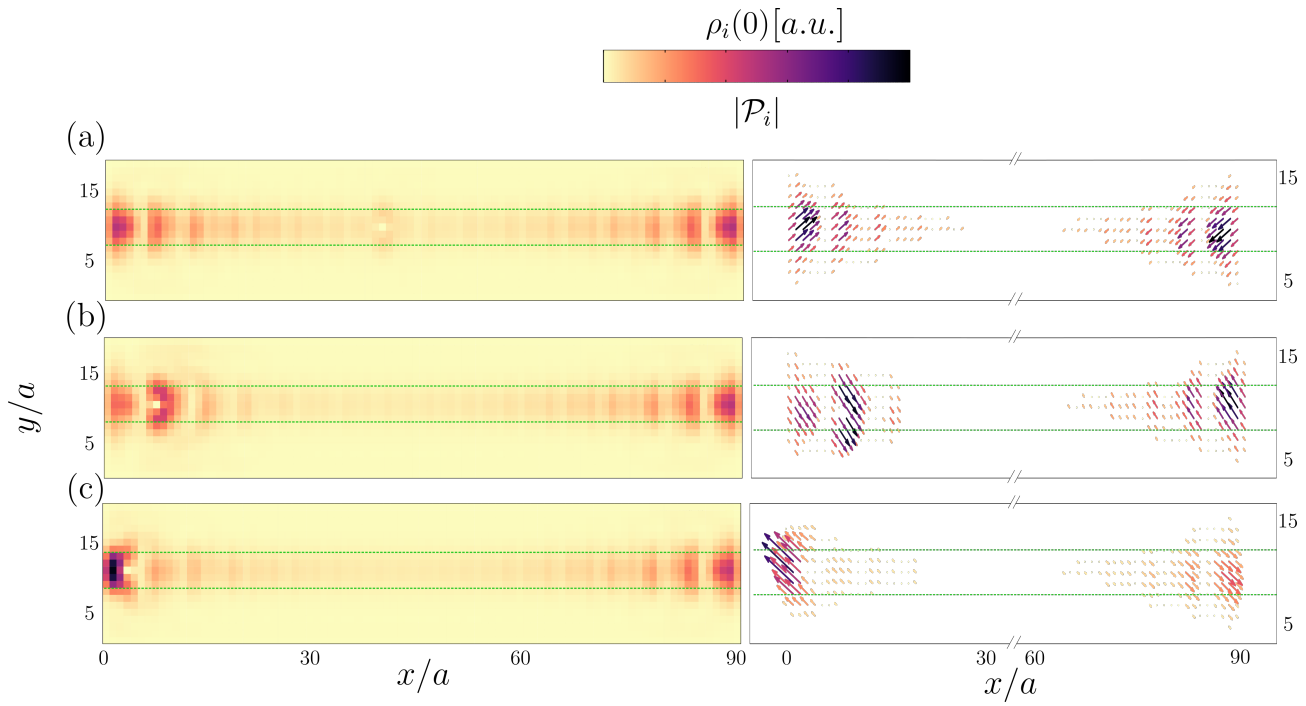

FIG. 6. The spatial density profile of the zero-energy Majorana quasiparticles (left panels) and their polarizations (right panels) obtained in the proximitized metallic strip, consisting of $N_w = 5$ rows of atoms, in presence of a point-like electrostatic defect with $V_0 = 100t$ at site: (a) $i_0 = 40a$, (b) $i_0 = 8a$, and (c) $i_0 = 4a$ and $N_y = 20$. The magnitude of the arrows in the right hand side plots show $|\mathcal{P}_{i\sigma}|$ and their direction show $\mathrm{Arg}\,\mathcal{P}_{i\sigma}$. We note that the phase is only well defined up to a global shift.

have revealed that such a local scattering potential can affect the localization length of the Majorana quasiparticles if deposited near the ends of the metallic strip. Under such circumstances the neighboring Majorana mode substantially reduces its spatial extent, which can be compared with what has been predicted in Ref.,[36] whereas the opposite-end Majorana mode remains practically intact. Similar coexistences of the localized and delocalized Majorana quasiparticles have been previously observed by scanning tunneling spectroscopy using a disordered monolayer of superconducting Pb coupled to underlying $Co-Si$ magnetic islands.[22] We hope that proximitized metallic strips would be a convenient platform not only for the realization of topological superconductivity, tunable by the magnetic field and Josephson phase, but could also allow for manipulating the Majorana quasiparticle length-scale.

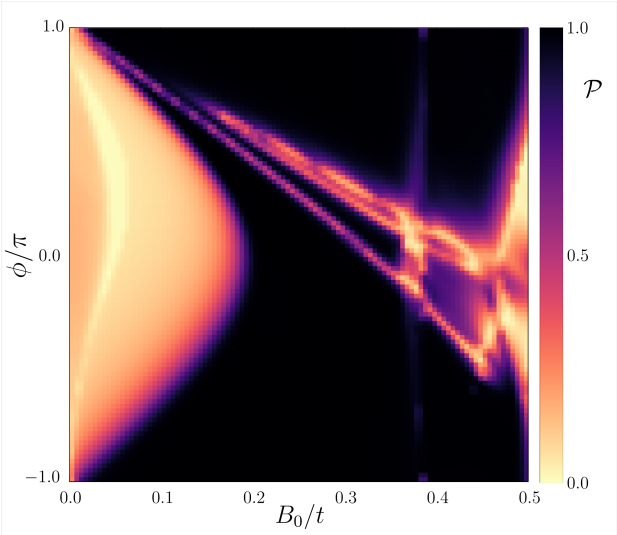

FIG. 7. The topological superconducting phase (dark area) with respect to the magnetic field B_0 and the Josephson phase ϕ obtained by the criterion concerning the global Majorana polarization.[21,38] Numerical computations were done for $N_w = 2$ and the same model parameters as in Fig. 2.

ACKNOWLEDGMENTS

We thank Benedikt Scharf for instructive discussions. This work is supported by National Science Centre (Poland) under the grants UMO-2017/27/N/ST3/01762 (SG), UMO-2018/29/B/ST3/01892 (NS), and UMO-2018/29/B/ST3/00937 (TD).

Appendix: Influence of the Josepshon phase

In the main part of this manuscript we have analyzed the spectroscopic properties of the Majorana quasiparticles, focusing on the particular case $\phi = \pi$, that is optimal for occurrence of the topological superconducting state. Similar qualitative features would be also observable for other values of the Josephson phase $\phi \neq \pi$, provided that model parameters (such as, e.g., the magnetic field) are appropriately tuned.[26,27] A possible criterion (proposed by one of us[21,38]) for determination of the topological diagram relies on the Majorana polarization for MBS to be non-vanishing when summed over a portion of the investigated system where the bound states should reside, in fact it should be equal to the total density of the state in the same region. Therefore

$$\mathcal{P} = \sum_{i \in \mathcal{R}} \frac{|\mathcal{P}_{in_0}|}{\rho_i(E_{n_0})} = 1 \tag{A.1}$$

for a MBS. This serves as a proxy for being in the topologically non-trivial phase. In the present scenario one can choose for this purpose either the leftmost or rightmost quarter of the metallic strip as the region $\mathcal{R}$. More details can be found in Ref. 21.

Fig. 7 displays the topological phase diagram, with the dark area being the nontrivial phase, obtained using this criterion for our heterostructure. We show the phase diagram with respect to the magnetic field B_0 and the Josephson phase ϕ. Let us remark, that such a criterion yields a smooth changeover between the topologically trivial and nontrivial superconducting states instead of a sharp transition. It can be hence useful for exploring the robustness of the topological state against perturbations such as inhomogeneity or thermal fluctuations.

* e-mail:szglodzik@kft.umcs.lublin.pl
† e-mail:sedlmayr@umcs.pl
‡ e-mail:doman@kft.umcs.lublin.pl

[1] M. T. Deng, C. L. Yu, G. Y. Huang, M. Larsson, P. Caroff, and H. Q. Xu, "Anomalous zero-bias conductance peak in a Nb–InSb nanowire–Nb hybrid device," Nano Lett. **12**, 6414 (2012).
[2] V. Mourik, K. Zuo, S. M. Frolov, S. R. Plissard, E. P. A. M. Bakkers, and L. P. Kouwenhoven, "Signatures of Majorana fermions in hybrid superconductor-semiconductor nanowire devices," Science **336**, 1003 (2012).
[3] A. Das, Y. Ronen, Y. Most, Y. Oreg, M. Heiblum, and H. Shtrikman, "Zero-bias peaks and splitting in an Al–InAs nanowire topological superconductor as a signature of Majorana fermions," Nat. Phys. **8**, 887 (2012).
[4] A. D. K. Finck, D. J. Van Harlingen, P. K. Mohseni, K. Jung, and X. Li, "Anomalous modulation of a zero-bias peak in a hybrid nanowire-superconductor device," Phys. Rev. Lett. **110**, 126406 (2013).
[5] R. M. Lutchyn, E. P. A. M. Bakkers, L. P. Kouwenhoven, P. Krogstrup, C. M. Marcus, and Y. Oreg, "Majorana zero modes in superconductor-semiconductor heterostructures," Nat. Rev. Mater. **3**, 52 (2018).
[6] S. Nadj-Perge, I. K. Drozdov, J. Li, H. Chen, S. Jeon, J. Seo, A. H. MacDonald, B. A. Bernevig, and A. Yazdani, "Observation of Majorana fermions in ferromagnetic atomic chains on a superconductor," Science **346**, 602 (2014).
[7] R. Pawlak, M. Kisiel, J. Klinovaja, T. Meier, S. Kawai, T. Glatzel, D. Loss, and E. Meyer, "Probing atomic structure and Majorana wavefunctions in mono-atomic Fe chains on superconducting Pb surface," Npj Quantum Information **2**, 16035 (2016).
[8] B. E. Feldman, M. T. Randeria, J. Li, S. Jeon, Y. Xie, Z. Wang, I. K. Drozdov, B. A. Bernevig, and A. Yazdani, "High-resolution studies of the Majorana atomic chain platform," Nat. Phys. **13**, 286 (2016).
[9] M. Ruby, B. W. Heinrich, Y. Peng, F. von Oppen, and K. J. Franke, "Exploring a proximity-coupled Co chain on Pb (110) as a possible Majorana platform," Nano Lett. **17**, 4473 (2017).
[10] S. Jeon, Y. Xie, J. Li, Z. Wang, B. A. Bernevig, and A. Yazdani, "Distinguishing a Majorana zero mode using spin-resolved measurements," Science **358**, 772 (2017).
[11] H. Kim, A. Palacio-Morales, T. Posske, L. Rózsa, K. Palotás, L. Szunyogh, M. Thorwart, and R. Wiesendanger, "Toward tailoring Majorana bound states in artificially constructed magnetic atom chains on elemental superconductors," Sci. Adv. **4** (2018), 10.1126/sciadv.1701476.
[12] F. Nichele, A. C. C. Drachmann, A. M. Whiticar, E. C. T. O'Farrell, H. J. Suominen, A. Fornieri, T. Wang, G. C. Gardner, C. Thomas, A. T. Hatke, P. Krogstrup, M. J. Manfra, K. Flensberg, and Ch. M. Marcus, "Scaling of Majorana zero-bias conductance peaks," Phys. Rev. Lett. **119**, 136803 (2017).
[13] J. Röntynen and T. Ojanen, "Topological superconductivity and high Chern numbers in 2D ferromagnetic Shiba lattices," Phys. Rev. Lett. **114**, 236803 (2015).
[14] K. Björnson, S. S. Pershoguba, A. V. Balatsky, and A. M. Black-Schaffer, "Spin-polarized edge currents and Majorana fermions in one- and two-dimensional topological superconductors," Phys. Rev. B **92**, 214501 (2015).
[15] J. Li, T. Neupert, Z. Wang, A. H. MacDonald, A. Yazdani, and B. A. Bernevig, "Two-dimensional chiral topological superconductivity in Shiba lattices," Nat. Commun. **7**, 12297 (2016).
[16] S. Rachel, E. Mascot, S. Cocklin, M. Vojta, and D. K. Morr, "Quantized charge transport in chiral Majorana edge modes," Phys. Rev. B **96**, 205131 (2017).
[17] Y. Volpez, D. Loss, and J. Klinovaja, "Rashba sandwiches with topological superconducting phases," Phys. Rev. B

97, 195421 (2018).
[18] G. C. Ménard, S. Guissart, Ch. Brun, R. T. Leriche, M. Trif, F. Debontridder, D. Demaille, D. Roditchev, P. Simon, and T. Cren, "Two-dimensional topological superconductivity in Pb/Co/Si(111)," Nat. Commun. **8**, 2040 (2017).
[19] Q. L. He, L. Pan, A. L. Stern, E. C. Burks, X. Che, G. Yin, J. Wang, B. Lian, Q. Zhou, E. S. Choi, K. Murata, X. Kou, Z. Chen, T. Nie, Q. Shao, Y. Fan, S.-C. Zhang, K. Liu, J. Xia, and K. L. Wang, "Chiral Majorana fermion modes in a quantum anomalous Hall insulator–superconductor structure," Science **357**, 294 (2017).
[20] A. Palacio-Morales, E. Mascot, S. Cocklin, H. Kim, S. Rachel, D.K. Morr, and R. Wiesendanger, "Atomic-scale interface engineering of Majorana edge modes in a 2D magnet-superconductor hybrid system," Sci. Adv. **5**, eaav6600 (2019).
[21] N. Sedlmayr, J. M. Aguiar-Hualde, and C. Bena, "Majorana bound states in open quasi-one-dimensional and two-dimensional systems with transverse Rashba coupling," Phys. Rev. B **93**, 155425 (2016).
[22] G. Ménard, A. Mesaros, C. Brun, F. Debontridder, D. Roditchev, P. Simon, and T. Cren, "Isolated pairs of Majorana zero modes in a disordered superconducting lead monolayer," Nat. Commun. **10**, 2587 (2019).
[23] F. Nichele, A. C. C. Drachmann, A. M. Whiticar, E. C. T. O'Farrell, H. J. Suominen, A. Fornieri, T. Wang, G. C. Gardner, C. Thomas, A. T. Hatke, P. Krogstrup, M. J. Manfra, K. Flensberg, and C. M. Marcus, "Scaling of Majorana zero-bias conductance peaks," Phys. Rev. Lett. **119**, 136803 (2017).
[24] A. Kobiałka, A. Ptok, and T. Domański, "Delocalisation of Majorana quasiparticles in plaquettenanowire hybrid system," Sci. Rep. **9**, 12933 (2019).
[25] E. Mascot, S. Cocklin, S. Rachel, and D.K. Morr, "Dimensional tuning of Majorana fermions and real space counting of the Chern number," Phys. Rev. B **100**, 184510 (2019).
[26] F. Pientka, A. Keselman, E. Berg, A. Yacoby, A. Stern, and B.I. Halperin, "Topological superconductivity in a planar Josephson junction," Phys. Rev. X **7**, 021032 (2017).
[27] Michael Hell, Martin Leijnse, and Karsten Flensberg, "Two-dimensional platform for networks of Majorana bound states," Phys. Rev. Lett. **118**, 107701 (2017).
[28] A. Fornieri, A.M. Whiticar, F. Setiawan, E. Portoles, A.C.C. Drachmann, A. Keselman, S. Gronin, C. Thomas, T. Wang, R. Kallaher, G.C. Gardner, E. Berg, M.J. Manfra, A. Stern, Ch.M. Marcus, and F. Nichele, "Evidence of topological superconductivity in planar Josephson junctions," Nature **569**, 89 (2019).
[29] H. Ren, F. Pientka, S. Hart, A.T. Pierce, M. Kosowsky, L. Lunczer, R. Schlereth, B. Scharf, E.M. Hankiewicz, L.W. Molenkamp, B.I. Halperin, and A. Yacoby, "Topological superconductivity in a phase-controlled Josephson junction," Nature **569**, 93 (2019).
[30] W. Mayer, M.C. Dartiailh, J. Yuan, A. Wickramasinghe, K.S. Matos-Abiague, I. Žutić, and J. Shabani, "Phase signature of topological transition in Josephson junctions," (2019), arXiv:1906.01179.
[31] F. Setiawan, Chien-Te Wu, and K. Levin, "Full proximity treatment of topological superconductors in Josephson-junction architectures," Phys. Rev. B **99**, 174511 (2019).
[32] F. Setiawan, A. Stern, and E. Berg, "Topological superconductivity in planar Josephson junctions: Narrowing down to the nanowire limit," Phys. Rev. B **99**, 220506 (2019).
[33] B. Scharf, F. Pientka, H. Ren, A. Yacoby, and E.M. Hankiewicz, "Tuning topological superconductivity in phase-controlled Josephson junctions with Rashba and Dresselhaus spin-orbit coupling," Phys. Rev. B **99**, 214503 (2019).
[34] T. Laeven, B. Nijholt, M. Wimmer, and A.R. Akhmerov, "Enhanced proximity effect in zigzag-shaped Majorana Josephson junctions," (2019), arXiv:1903.06168.
[35] A. Stern and E. Berg, "Fractional Josephson vortices and braiding of Majorana zero modes in planar superconductor-semiconductor heterostructures," Phys. Rev. Lett. **122**, 107701 (2019).
[36] A. Haim and A. Stern, "Benefits of weak disorder in one-dimensional topological superconductors," Phys. Rev. Lett. **122**, 126801 (2019).
[37] D. Sticlet, C. Bena, and P. Simon, "Spin and Majorana polarization in topological superconducting wires," Phys. Rev. Lett. **108**, 096802 (2012).
[38] N. Sedlmayr and C. Bena, "Visualizing Majorana bound states in one and two dimensions using the generalized Majorana polarization," Phys. Rev. B **92**, 115115 (2015).
[39] N. Sedlmayr, G. Guigou, P. Simon, and C. Bena, "Majoranas with and without a 'character': hybridization, braiding and chiral Majorana number," J. Phys.: Condens. Matter **27**, 455601 (2015).
[40] M. M. Maśka and T. Domanski, "Polarization of the Majorana quasiparticles in the Rashba chain," Sci. Rep. **7**, 16193 (2017).
[41] V. Kaladzhyan, J. Despres, I. Mandal, and C. Bena, "Majorana fermions in finite-size strips with in-plane magnetic fields," Eur. Phys. J. B **90** (2017), 10.1140/epjb/e2017-80103-y.
[42] J. J. He, T. K. Ng, P. A. Lee, and K. T. Law, "Selective equal-spin Andreev reflections induced by Majorana fermions," Phys. Rev. Lett. **112**, 037001 (2014).
[43] B. Scharf, F. Pientka, H. Ren, A. Yacoby, and E.M. Hankiewicz, "Tuning topological superconductivity in phase-controlled Josephson junctions with Rashba and Dresselhaus spin-orbit coupling," Phys. Rev. B **99**, 214503 (2019).
[44] D. Chevallier and J. Klinovaja, "Tomography of Majorana fermions with STM tips," Phys. Rev. B **94**, 035417 (2016).
[45] N. Sedlmayr, J. M. Aguiar-Hualde, and C. Bena, "Flat Majorana bands in two-dimensional lattices with inhomogeneous magnetic fields: Topology and stability," Phys. Rev. B **91**, 115415 (2015).
[46] A. Y. Kitaev, "Unpaired Majorana fermions in quantum wires," Phys.-Usp. **44**, 131 (2001).
[47] P.W. Brouwer, M. Duckheim, A. Romito, and F. von Oppen, "Topological superconducting phases in disordered quantum wires with strong spin-orbit coupling," Phys. Rev. B **84**, 144526 (2011).
[48] W. DeGottardi, D. Sen, and S. Vishveshwara, "Majorana fermions in superconducting 1d systems having periodic, quasiperiodic, and disordered potentials," Phys. Rev. Lett. **110**, 146404 (2013).
[49] H.-Y. Hui, J.D. Sau, and S. Das Sarma, "Bulk disorder in the superconductor affects proximity-induced topological superconductivity," Phys. Rev. B **92**, 174512 (2015).
[50] S. Hoffman, J. Klinovaja, and D. Loss, "Topological phases of inhomogeneous superconductivity," Phys. Rev. B **93**, 165418 (2016).
[51] P. Zhang and F. Nori, "Majorana bound states in a disordered quantum dot chain," New J. Phys. **18**, 043033 (2016).

[52] Suraj S. Hegde and Smitha Vishveshwara, "Majorana wave-function oscillations, fermion parity switches, and disorder in kitaev chains," Phys. Rev. B **94**, 115166 (2016).
[53] W.S. Cole, J.D. Sau, and S. Das Sarma, "Proximity effect and Majorana bound states in clean semiconductor nanowires coupled to disordered superconductors," Phys. Rev. B **94**, 140505 (2016).
[54] B. Pekerten, A. Teker, Ö. Bozat, M. Wimmer, and İ. Adagideli, "Disorder-induced topological transitions in multichannel majorana wires," Phys. Rev. B **95**, 064507 (2017).
[55] Y. Hu, Z. Cai, M.A. Baranov, and P. Zoller, "Majorana fermions in noisy kitaev wires," Phys. Rev. B **92**, 165118 (2015).
[56] J. Klinovaja and D. Loss, "Fermionic and Majorana bound states in hybrid nanowires with non-uniform spin-orbit interaction," Eur. Phys. J. B **88**, 62 (2015).
[57] B. Kiczek and A. Ptok, "Influence of the orbital effects on the Majorana quasi -particles in a nanowire," J. Phys.: Condens. Matter **29**, 495301 (2017).
[58] J. Klinovaja, P. Stano, A. Yazdani, and D. Loss, "Topological superconductivity and Majorana fermions in RKKY systems," Phys. Rev. Lett. **111**, 186805 (2013).
[59] B. Braunecker and P. Simon, "Self-stabilizing temperature-driven crossover between topological and nontopological ordered phases in one-dimensional conductors," Phys. Rev. B **92**, 241410 (2015).
[60] W. Hu, R.T. Scalettar, and R. R. P. Singh, "Interplay of magnetic order, pairing, and phase separation in a one-dimensional spin-fermion model," Phys. Rev. B **92**, 115133 (2015).
[61] A. Gorczyca-Goraj, T. Domański, and M.M. Maśka, "Topological superconductivity at finite temperatures in proximitized magnetic nanowires," Phys. Rev. B **99**, 235430 (2019).
[62] M. M. Maśka, A. Gorczyca-Goraj, J. Tworzydło, and T. Domański, "Majorana quasiparticles of an inhomogeneous Rashba chain," Phys. Rev. B **95**, 045429 (2017).

Chapter 5

Bibliography

[1] D. van Delft and P. Kes, "The discovery of of superconductivity," *Physics Today*, vol. 63, p. 38, 2010.

[2] J. Schmalian, "Failed theories of superconductivity," *Modern Physics Letters B*, vol. 24, pp. 2679–2691, 2010.

[3] J. Bardeen, L. N. Cooper, and J. R. Schrieffer, "Theory of superconductivity," *Phys. Rev.*, vol. 108, pp. 1175–1204, Dec 1957.

[4] K. v. Klitzing, G. Dorda, and M. Pepper, "New method for high-accuracy determination of the fine-structure constant based on quantized Hall resistance," *Phys. Rev. Lett.*, vol. 45, pp. 494–497, Aug 1980.

[5] N. R. Poniatowski, "Superconductivity, broken gauge symmetry, and the Higgs mechanism," *American Journal of Physics*, vol. 87, no. 6, pp. 436–443, 2019.

[6] J. E. Moore, "The birth of topological insulators," *Nature*, vol. 464, no. 7286, pp. 194–198, 2010.

[7] W. P. Su, J. R. Schrieffer, and A. J. Heeger, "Solitons in polyacetylene," *Phys. Rev. Lett.*, vol. 42, pp. 1698–1701, Jun 1979.

[8] B. A. Bernevig, T. L. Hughes, and S.-C. Zhang, "Quantum spin Hall effect and topological phase transition in HgTe quantum wells," *Science*, vol. 314, no. 5806, pp. 1757–1761, 2006.

[9] C. L. Kane and E. J. Mele, "Quantum spin Hall effect in graphene," *Phys. Rev. Lett.*, vol. 95, p. 226801, Nov 2005.

[10] J. D. Sau, R. M. Lutchyn, S. Tewari, and S. Das Sarma, "Generic new platform for topological quantum computation using semiconductor heterostructures," *Phys. Rev. Lett.*, vol. 104, p. 040502, Jan 2010.

[11] P. Anderson, "Theory of dirty superconductors," *Journal of Physics and Chemistry of Solids*, vol. 11, no. 1, pp. 26 – 30, 1959.

[12] K. I. Wysokiński, "Spectral and transport properties of strongly correlated disordered systems," *Phys. Rev. B*, vol. 60, pp. 16376–16381, Dec 1999.

[13] A. V. Balatsky, I. Vekhter, and J.-X. Zhu, "Impurity-induced states in conventional and unconventional superconductors," *Rev. Mod. Phys.*, vol. 78, pp. 373–433, May 2006.

[14] G. Binnig, H. Rohrer, C. Gerber, and E. Weibel, "Surface studies by scanning tunneling microscopy," *Phys. Rev. Lett.*, vol. 49, pp. 57–61, Jul 1982.

[15] G. Dresselhaus, "Spin-orbit coupling effects in zinc blende structures," *Phys. Rev.*, vol. 100, pp. 580–586, Oct 1955.

[16] Y. A. Bychkov and É. I. Rashba, "Properties of a 2D electron gas with lifted spectral degeneracy," *Soviet Journal of Experimental and Theoretical Physics Letters*, vol. 39, p. 78, Jan. 1984.

[17] A. Manchon, H. C. Koo, J. Nitta, S. M. Frolov, and R. A. Duine, "New perspectives for Rashba spin–orbit coupling," *Nature Materials*, vol. 14, pp. 871–882, Sep 2015.

[18] L. N. Cooper, "Bound electron pairs in a degenerate Fermi gas," *Phys. Rev.*, vol. 104, pp. 1189–1190, Nov 1956.

[19] H. Fröhlich, "Theory of the superconducting state. I. the ground state at the absolute zero of temperature," *Phys. Rev.*, vol. 79, pp. 845–856, Sep 1950.

[20] J. Kondo, "Resistance Minimum in Dilute Magnetic Alloys," *Progress of Theoretical Physics*, vol. 32, pp. 37–49, 07 1964.

[21] P. W. Anderson, "Localized magnetic states in metals," *Phys. Rev.*, vol. 124, pp. 41–53, Oct 1961.

[22] A. L. Fetter, "Spherical impurity in an infinite superconductor," *Phys. Rev.*, vol. 140, pp. A1921–A1936, Dec 1965.

[23] K. Machida and F. Shibata, "Bound States Due to Resonance Scattering in Superconductor," *Progress of Theoretical Physics*, vol. 47, pp. 1817–1823, 06 1972.

[24] J. Barański and T. Domański, "In-gap states of a quantum dot coupled between a normal and a superconducting lead," *Journal of Physics: Condensed Matter*, vol. 25, p. 435305, Oct 2013.

[25] G. Kiršanskas, M. Goldstein, K. Flensberg, L. I. Glazman, and J. Paaske, "Yu-Shiba-Rusinov states in phase-biased superconductor–quantum dot–superconductor junctions," *Phys. Rev. B*, vol. 92, p. 235422, Dec 2015.

[26] L. Yu, "Bound states in superconductors with paramegnetic impurities," *Acta Physica Sinica*, vol. 114, no. 1, pp. 75–91, 1965.

[27] H. Shiba, "Classical Spins in Superconductors," *Progress of Theoretical Physics*, vol. 40, pp. 435–451, 09 1968.

[28] A. Rusinov, "Superconductivity near a paramagnetic impurity," *Pis'ma v Zh. Eksp. Teor. Fiz.*, vol. 9, no. 146, p. 85, 1968.

[29] A. Yazdani, B. A. Jones, C. P. Lutz, M. F. Crommie, and D. M. Eigler, "Probing the local effects of magnetic impurities on superconductivity," *Science*, vol. 275, no. 5307, pp. 1767–1770, 1997.

[30] M. E. Flatté and J. M. Byers, "Local electronic structure of a single magnetic impurity in a superconductor," *Phys. Rev. Lett.*, vol. 78, pp. 3761–3764, May 1997.

[31] K. J. Franke, G. Schulze, and J. I. Pascual, "Competition of superconducting phenomena and Kondo screening at the nanoscale," *Science*, vol. 332, no. 6032, pp. 940–944, 2011.

[32] B. W. Heinrich, J. I. Pascual, and K. J. Franke, "Single magnetic adsorbates on s-wave superconductors," *Progress in Surface Science*, vol. 93, no. 1, pp. 1 – 19, 2018.

[33] R. Maurand, T. Meng, E. Bonet, S. Florens, L. Marty, and W. Wernsdorfer, "First-order $0-\pi$ quantum phase transition in the Kondo regime of a superconducting carbon-nanotube quantum dot," *Phys. Rev. X*, vol. 2, p. 011009, Feb 2012.

[34] L. Farinacci, G. Ahmadi, G. Reecht, M. Ruby, N. Bogdanoff, O. Peters, B. W. Heinrich, F. von Oppen, and K. J. Franke, "Tuning the coupling of an individual magnetic impurity to a superconductor: Quantum phase transition and transport," *Phys. Rev. Lett.*, vol. 121, p. 196803, Nov 2018.

[35] B. W. Hatter, Ninoand Heinrich, M. Ruby, J. I. Pascual, and K. J. Franke, "Magnetic anisotropy in Shiba bound states across a quantum phase transition," *Nature Communications*, vol. 6, p. 8988, Nov 2015.

[36] M. V. Berry, "Quantal phase factors accompaying adiabatic changes," *Proc. R. Soc. Lond. A*, vol. 392, pp. 45–57, 1984.

[37] B. Simon, "Holonomy, the quantum adiabatic theorem, and Berry's phase," *Phys. Rev. Lett.*, vol. 51, pp. 2167–2170, Dec 1983.

[38] D. J. Thouless, M. Kohmoto, M. P. Nightingale, and M. den Nijs, "Quantized Hall conductance in a two-dimensional periodic potential," *Phys. Rev. Lett.*, vol. 49, pp. 405–408, Aug 1982.

[39] S. Ryu, A. P. Schnyder, A. Furusaki, and A. W. W. Ludwig, "Topological insulators and superconductors: tenfold way and dimensional hierarchy," *New Journal of Physics*, vol. 12, p. 065010, Jun 2010.

[40] F. D. M. Haldane, "Model for a quantum Hall effect without Landau levels: Condensed-matter realization of the "parity anomaly"," *Phys. Rev. Lett.*, vol. 61, pp. 2015–2018, Oct 1988.

[41] C. L. Kane and E. J. Mele, "Z_2 Topological order and the quantum spin Hall effect," *Phys. Rev. Lett.*, vol. 95, p. 146802, Sep 2005.

[42] E. Majorana, "Teoria simmetrica dell'elettrone e del positrone," *Il Nuovo Cimento (1924-1942)*, vol. 14, p. 171, Sep 2008.

[43] F. Wilczek, "Majorana returns," *Nature Physics*, vol. 5, pp. 614–618, Sep 2009.

[44] M. Sato and Y. Ando, "Topological superconductors: a review," *Reports on Progress in Physics*, vol. 80, p. 076501, May 2017.

[45] M. Sato and S. Fujimoto, "Majorana fermions and topology in superconductors," *Journal of the Physical Society of Japan*, vol. 85, no. 7, p. 072001, 2016.

[46] X.-L. Qi and S.-C. Zhang, "Topological insulators and superconductors," *Rev. Mod. Phys.*, vol. 83, pp. 1057–1110, Oct 2011.

[47] C. Nayak, S. H. Simon, A. Stern, M. Freedman, and S. Das Sarma, "Non-Abelian anyons and topological quantum computation," *Rev. Mod. Phys.*, vol. 80, pp. 1083–1159, Sep 2008.

[48] J. Alicea, "New directions in the pursuit of Majorana fermions in solid state systems," *Reports on Progress in Physics*, vol. 75, p. 076501, Jun 2012.

[49] N. Read and D. Green, "Paired states of fermions in two dimensions with breaking of parity and time-reversal symmetries and the fractional quantum Hall effect," *Phys. Rev. B*, vol. 61, pp. 10267–10297, Apr 2000.

[50] M. Sato, "Non-abelian statistics of axion strings," *Physics Letters B*, vol. 575, no. 1, pp. 126 – 130, 2003.

[51] L. Fu and C. L. Kane, "Superconducting proximity effect and Majorana fermions at the surface of a topological insulator," *Phys. Rev. Lett.*, vol. 100, p. 096407, Mar 2008.

[52] S. Fujimoto, "Topological order and non-abelian statistics in noncentrosymmetric s-wave superconductors," *Phys. Rev. B*, vol. 77, p. 220501, Jun 2008.

[53] A. P. Schnyder and S. Ryu, "Topological phases and surface flat bands in superconductors without inversion symmetry," *Phys. Rev. B*, vol. 84, p. 060504, Aug 2011.

[54] M. H. Fischer, T. Neupert, C. Platt, A. P. Schnyder, W. Hanke, J. Goryo, R. Thomale, and M. Sigrist, "Chiral d-wave superconductivity in SrPtAs," *Phys. Rev. B*, vol. 89, p. 020509, Jan 2014.

[55] X. Xi, Z. Wang, W. Zhao, J.-H. Park, K. T. Law, H. Berger, L. Forró, J. Shan, and K. F. Mak, "Ising pairing in superconducting $NbSe_2$ atomic layers," *Nature Physics*, vol. 12, pp. 139–143, Feb 2016.

[56] W.-Y. He, B. T. Zhou, J. J. He, N. F. Q. Yuan, T. Zhang, and K. T. Law, "Magnetic field driven nodal topological superconductivity in monolayer transition metal dichalcogenides," *Communications Physics*, vol. 1, p. 40, Jul 2018.

[57] I. Reis, D. J. J. Marchand, and M. Franz, "Self-organized topological state in a magnetic chain on the surface of a superconductor," *Phys. Rev. B*, vol. 90, p. 085124, Aug 2014.

[58] T. Das, J.-X. Zhu, and M. J. Graf, "Local suppression of the superfluid density of $PuCoGa_5$ by strong onsite disorder," *Phys. Rev. B*, vol. 84, p. 134510, Oct 2011.

[59] J. Linder, Y. Tanaka, T. Yokoyama, A. Sudbø, and N. Nagaosa, "Unconventional superconductivity on a topological insulator," *Phys. Rev. Lett.*, vol. 104, p. 067001, Feb 2010.

[60] J.-X. Zhu, *Bogoliubov-de Gennes Method and Its Applications*. Springer, 2016.

[61] S. S. Pershoguba, K. Björnson, A. M. Black-Schaffer, and A. V. Balatsky, "Currents induced by magnetic impurities in superconductors with spin-orbit coupling," *Phys. Rev. Lett.*, vol. 115, p. 116602, Sep 2015.

[62] V. Mourik, K. Zuo, S. M. Frolov, S. R. Plissard, E. P. A. M. Bakkers, and L. P. Kouwenhoven, "Signatures of Majorana fermions in hybrid superconductor-semiconductor nanowire devices," *Science*, vol. 336, no. 6084, pp. 1003–1007, 2012.

[63] O. A. Awoga, J. Cayao, and A. M. Black-Schaffer, "Supercurrent detection of topologically trivial zero-energy states in nanowire junctions," *Phys. Rev. Lett.*, vol. 123, p. 117001, Sep 2019.

[64] D. Sticlet, C. Bena, and P. Simon, "Spin and Majorana polarization in topological superconducting wires," *Phys. Rev. Lett.*, vol. 108, p. 096802, Mar 2012.

[65] N. Sedlmayr and C. Bena, "Visualizing Majorana bound states in one and two dimensions using the generalized Majorana polarization," *Phys. Rev. B*, vol. 92, p. 115115, Sep 2015.

[66] C. Bena, "Testing the formation of Majorana states using Majorana polarization," *Comptes Rendus Physique*, vol. 18, no. 5, pp. 349 – 357, 2017. 2016 Prizes of the French Academy of Sciences /Prix 2016 de l'Académie des sciences.

[67] G. C. Ménard, S. Guissart, C. Brun, S. Pons, V. S. Stolyarov, F. Debontridder, M. V. Leclerc, E. Janod, L. Cario, D. Roditchev, P. Simon, and T. Cren, "Coherent long-range magnetic bound states in a superconductor," *Nature Physics*, vol. 11, no. 12, pp. 1013–1016, 2015.

[68] M. Bonilla, S. Kolekar, Y. Ma, H. C. Diaz, V. Kalappattil, R. Das, T. Eggers, H. R. Gutierrez, M.-H. Phan, and M. Batzill, "Strong room-temperature ferromagnetism in VSe_2 monolayers on van der Waals substrates," *Nature Nanotechnology*, vol. 13, pp. 289–293, Apr 2018.

[69] J. M. Lu, O. Zheliuk, I. Leermakers, N. F. Q. Yuan, U. Zeitler, K. T. Law, and J. T. Ye, "Evidence for two-dimensional Ising superconductivity in gated MoS_2," *Science*, vol. 350, no. 6266, pp. 1353–1357, 2015.

[70] J. Li, T. Neupert, Z. Wang, A. H. MacDonald, A. Yazdani, and B. A. Bernevig, "Two-dimensional chiral topological superconductivity in Shiba lattices," *Nature Communications*, vol. 7, p. 12297, Jul 2016.

[71] J. Röntynen and T. Ojanen, "Topological superconductivity and high Chern numbers in 2D ferromagnetic Shiba lattices," *Phys. Rev. Lett.*, vol. 114, p. 236803, Jun 2015.

[72] G. C. Ménard, S. Guissart, C. Brun, R. T. Leriche, M. Trif, F. Debontridder, D. Demaille, D. Roditchev, P. Simon, and T. Cren, "Two-dimensional topological superconductivity in Pb/Co/Si(111)," *Nature Communications*, vol. 8, p. 2040, Dec 2017.

[73] A. Palacio-Morales, E. Mascot, S. Cocklin, H. Kim, S. Rachel, D. K. Morr, and R. Wiesendanger, "Atomic-scale interface engineering of Majorana edge modes in a 2D magnet-superconductor hybrid system," *Science Advances*, vol. 5, no. 7, 2019.

[74] M. Hell, M. Leijnse, and K. Flensberg, "Two-dimensional platform for networks of Majorana bound states," *Phys. Rev. Lett.*, vol. 118, p. 107701, Mar 2017.

[75] F. Pientka, A. Keselman, E. Berg, A. Yacoby, A. Stern, and B. I. Halperin, "Topological superconductivity in a planar Josephson junction," *Phys. Rev. X*, vol. 7, p. 021032, May 2017.

[76] A. Fornieri, A. M. Whiticar, F. Setiawan, E. Portolés, A. C. C. Drachmann, A. Keselman, S. Gronin, C. Thomas, T. Wang, R. Kallaher, G. C. Gardner, E. Berg, M. J. Manfra, A. Stern, C. M. Marcus, and F. Nichele, "Evidence of topological superconductivity in planar Josephson junctions," *Nature*, vol. 569, pp. 89–92, May 2019.

[77] H. Ren, F. Pientka, S. Hart, A. T. Pierce, M. Kosowsky, L. Lunczer, R. Schlereth, B. Scharf, E. M. Hankiewicz, L. W. Molenkamp, B. I. Halperin, and A. Yacoby, "Topological superconductivity in a phase-controlled Josephson junction," *Nature*, vol. 569, pp. 93–98, May 2019.